UNIVERSITÉ DU
LUXEMBOURG

DISSERTATION

Defence held on 27/10/2021 in Luxembourg

to obtain the degree of

DOCTEUR DE L'UNIVERSITÉ DU LUXEMBOURG

EN SCIENCES DE L'INGÉNIEUR

by

Mahdi AMNE ELAHI
Born on 4 June 1987 in Tehran (Iran)

PROCESS INNOVATION FOR SENSORS IN MOBILE APPLICATIONS BASED ON LASER ASSISTED METAL-POLYMER JOINING

Dissertation defence committee
Dr. Peter PLAPPER, Dissertation Supervisor
Professor, Université du Luxembourg

Dr. Frank MÜCKLICH
Professor, Saarland University

Dr. Slavomir KEDZIORA, Chairman
Professor, Université du Luxembourg

Dr. Laurent HOUSSIAU
Professor, Université de Namur

Dr. Uwe REISGEN, Vice Chairman
Professor, RWTH Aachen

Contents

Preface

The present thesis is the result of my studies at the University of Luxembourg as a doctoral candidate; a challenging journey that brought me valuable experiences. I would like to appreciate the time and consideration of the jury members, Prof. Dr. Frank Mücklich, Prof. Dr. Slavomir Kedziora, Prof. Dr. Laurent Houssiau, Prof. Dr. Uwe Reisgen, and my supervisor, Prof. Dr. Peter Plapper for the evaluation of my thesis.

The journey started even before my physical presence in Luxembourg with writing the proposal for Luxembourg National Research Fund (FNR). I would like to acknowledge and appreciate the support of my supervisor, Mrs. Berta Rato (coordinator of the FSTM research facilitator team), and the management of Cebi Luxembourg S.A., Mr. Raymond Mohrbach, and Mr. Angelo Bove. The collaboration resulted in an AFR-PPP grant (reference 11633333). Therefore, I appreciate the opportunity FNR gave me to study at the University of Luxembourg.

I had the pleasure of meeting Dr. Patrick Soubiran from Cebi and sharing the results of my experiments with him regularly. His constructive comments and support are appreciated.

Before the lockdown of Covid-19, the most motivating and productive days of my studies were at INM (Leibniz Institute for New Materials) doing electron microscopy with Dr. Marcus Koch. His kind contribution brought my studies to another level. The collaboration resulted in several valuable publications in conferences and journals. I also appreciate the contribution of Dr. Frédéric Addiego, Mr. Julien Bardon, and Dr. Jérôme Guillot from the Luxembourg Institute of Science and Technology (LIST).

I would like to thank all my colleagues/friends at the University of Luxembourg as well who supported me with the inspiring discussions.

Last but not least, I would like to appreciate the dedication of my lovely wife, Sanaz, throughout my Ph.D. studies, my parents who are far away in Iran but I have been always blessed with their support and dedication.

Mahdi Amne Elahi

October 2021, Luxembourg

1. Abstract

The laser joining of metals to polymers is currently an interesting research area thanks to the capability of developing lightweight structures. Considering their miscellaneous applications in the automotive industry, aluminum and polyamide are chosen as the material combination for this study. There are three main challenges regarding the laser joining of metals to polymers in general: significant difference between the melting points of the materials, adhesion at the interface, and the mechanical properties of the assembly.

The first challenge is addressed by in-situ heating observation and temperature measurement during the joining process. Therefore, polyamide thermal pyrolysis is effectively avoided by optimizing the laser joining parameters and employing power modulation.

The second one is studied by applying different surface treatments on the materials (laser-based and abrasive-based). The surfaces were tested by several characterization techniques before and after each surface treatment. The modification of the surface structure through an appropriate surface treatment leads to the improvement of wetting and adhesion between the melted polyamide and aluminum surface. Therefore, the alteration of a mixed failure (adhesive/cohesive) to a fully cohesive failure is the major step to enhance the mechanical properties of the assemblies. However, in the absence of bubbles, the structural modification of polyamide during the joining process is responsible for the failure. Energy-dispersive X-ray[1] mapping and Time-of-Flight Secondary Ion Mass Spectrometry[2] shows the physicochemical bonding between aluminum oxide and the polyamide at the interface.

To further enhance the mechanical properties of the assemblies, the structure of the polyamide near the interface of metal/polymer is addressed. For this purpose, laser treatment of polyamide, post-heat treatment, and joining with different feed rates were implemented. Finally, the shear strength of approximately 45 MPa on average is achieved for the assembly of laser-polished aluminum laser-joined to the polyamide with 2 and 5 mm/s feed rates.

Keywords: Laser joining of aluminum-polyamide, Surface pre-treatment, Laser polishing, Tensile-shear test, Failure mechanism.
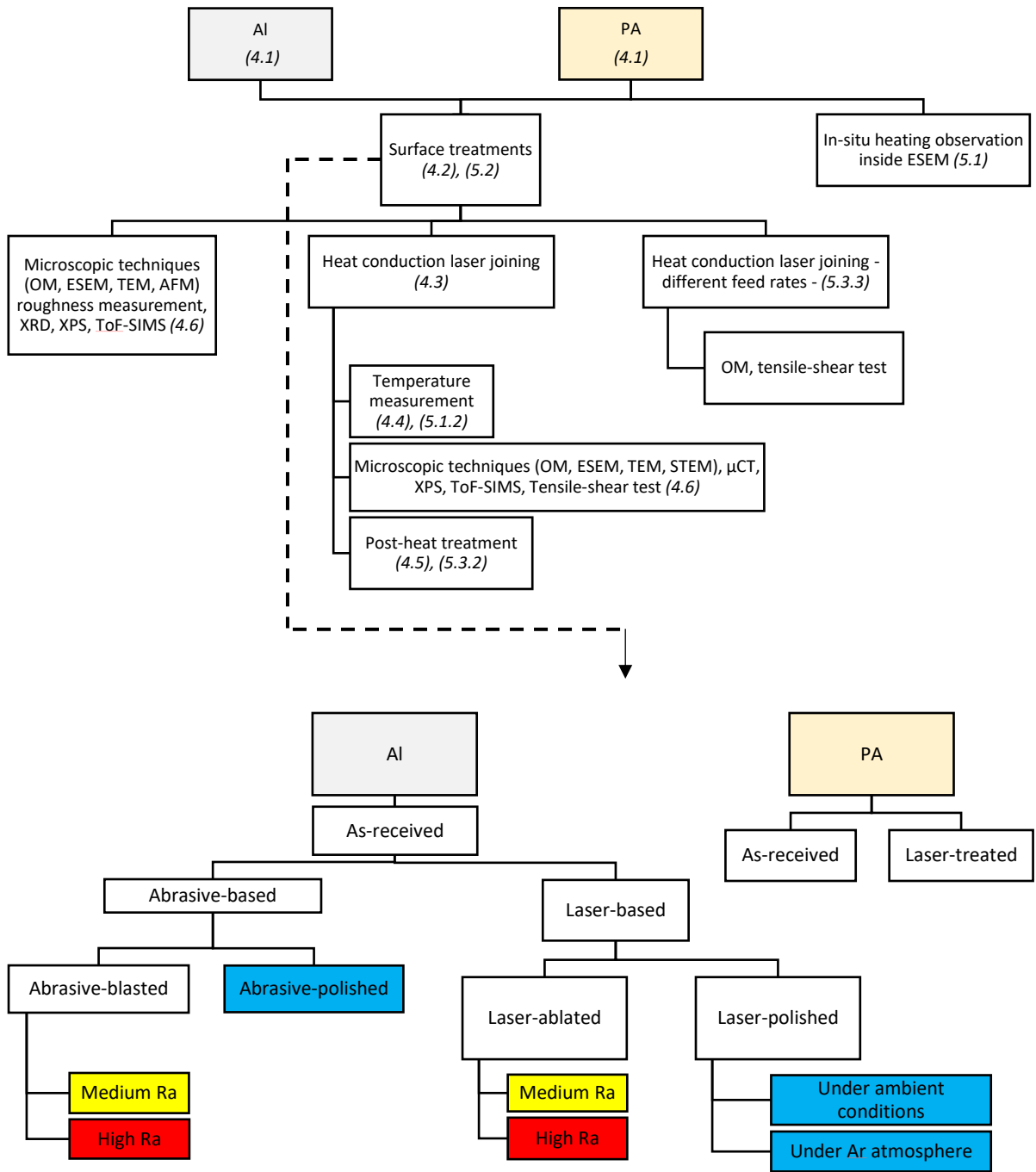
---

[1] EDX
[2] ToF-SIMS

1.1. Graphical abstract

2. Introduction

The application of lightweight structures will be increased from 30% to 70% by 2030 to reduce energy consumption and CO_2 emission in mobile industries [1]. Lightweight metal-polymer hybrid components have gained major applications in aerospace and automotive industries to take advantage of the unique physical and mechanical properties of metals and polymers in the assemblies. For instance, metals are commonly used where a high strength-toughness ratio and/or high thermal or electrical conductivity is required while polymers are well known for their light weight, high corrosion resistance, and excellent formability [2].

Consequently, advanced joining methods must be applied to realize the metal-polymer hybrid assemblies. There are three main joining methods for this purpose: mechanical fastening, adhesive bonding, and thermal bonding (welding). Mechanical fastening needs extra assembly elements which stand in contrast with the concept of lightweight design and demonstrates weak flexibility in joint design. Adhesive bonding is relatively simple; however, there are some limitations like requiring extensive surface preparation, not being environmentally friendly and deterioration by external influences like temperature and humidity [3].

Among thermal bonding, laser-assisted metal-plastic (LAMP) joining is gaining significant attention in the automotive industry. This new technology is flexible and fast, can be automated very well and the heat input is localized and low. Besides them, achieving superior strength by cohesive failure, made the process promising [4].

The LAMP joining is not well-industrialized for the hybrid structures of sensor application. The common production method for joining metal to polymer for this application is in-mold technology or crimp fastening with the assistance of sealant to seal polymers around electric sensors or electric circuits. There are, however, some innovations using LAMP joining:

- The time of laser joining process is shorter. In addition, the laser process has great potential for automation.
- The necessity of using sealing components like gaskets is eliminated because, unlike in-mold technology, a sound metal-polymer LAMP joined interface is gas and liquid sealed.
- The need for mechanical interlocking by applying flanges to the metallic component can be excluded. It means shorter production time plus saving materials.
- Flexibility during the development phase of new sensor solutions can be achieved.

As the industrial partner of the project, Cebi Luxembourg S.A. is looking forward to solving the problems in dissimilar materials joining. There are some industrial challenges in joining dissimilar materials using LAMP joining such as minimizing the volume of mating flanges,

reducing the time of assembly processes, and achieving superior joint characteristics against conventional processes, like in-mold technology or using adhesives. Therefore, the originality of the project dictates overcoming these challenges and covering industrial partners' requirements. Considering the limitation of conventional processes to join dissimilar materials, the project partner would like to develop new components tailored to successfully perform at a high-temperature range and higher-pressure application. To achieve the mentioned goals and application, it is reasonable to pursue recent joining technologies such as LAMP joining.

3. Literature review

3.1. Adhesion theories

To have a better understanding of the metal/polymer joining mechanism at the interface, different adhesion theories are presented in figure 3.1. The process of bonding cannot be explained merely by an individual theory and usually, a combination of them defines the whole mechanism of bonding. In this regard, applying surface treatments is necessary for the following reasons:

- To avoid the later formation of a weak layer on the substrate.
- To increase the molecular interaction between the adhesive and the substrate.
- To ensure sufficient joint strength by optimizing the adhesion forces at the interface.
- To develop a specific microstructure on the surface of the substrate [5].
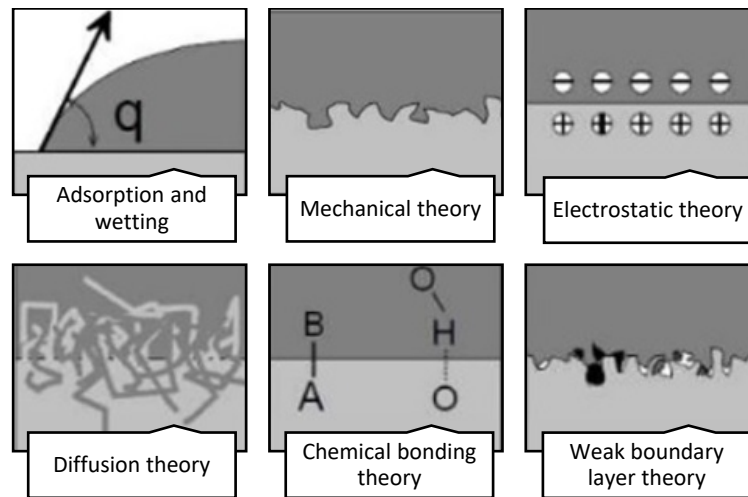
Figure 3.1. Different adhesion theories [5]–[7].

3.1.1. Adsorption and wetting

The adhesive material must behave as a liquid to spread on the adherents and make intimate contact with them (wetting). Wetting is determined by contact angle measurement which is governed by the young equation (equation 3.1) [7]:

$$\gamma_{LV} \cos \theta = \gamma_{SV} - \gamma_{SL} \tag{3.1}$$

θ: equilibrium contact angle
γ_{SV}: interfacial tension of the solid material in equilibrium with a fluid vapor
γ_{SL}: interfacial tension between the solid and liquid materials

If the material spreads uniformly over a substrate and creates a thin film, complete wetting happens, and $\theta = 0°$ or $\gamma_{SV} > \gamma_{SL} + \gamma_{LV}$

When γ_{SV} is high and γ_{LV} is low (like in the case of low-energy polymers over high-energy substrates such as metals) wetting is promoted. On the contrary, polymer substrates with low surface energies are not effectively wetted by other materials. This phenomenon is the route of applications requiring nonstick, passive surfaces. Adsorption and wetting theory is the foundation of developing adhesive materials with a lower surface tension compared to the adherend surfaces (such as epoxy resins as a proper adhesive for steel) [7].

3.1.2. Mechanical theory

Adhesion occurs by penetration of the adhesive into irregularities of the substrate surface like pores and cavities to form the mechanical interlocking. Normally adhesive bonds better to rough surfaces than to smooth ones however, it is not universally true as good adhesion also occurs between smooth surfaces. Improvement of adhesion based on mechanical theory is via one or more of the following: mechanical interlocking, formation of a clean or highly reactive surface, and increasing the contact surface area. Although increasing the surface roughness promotes mechanical interlocking, it is also argued that the increase of the adhesive contact surface enhances other mechanisms like wetting and chemical bonding. The increased surface roughness is reported to have a positive effect on joint strength and durability however, there are also some contrary observations [5], [7].

3.1.3. Electrostatic and diffusion theory

Compared to the previous theories, electrostatic and diffusion theories have gained less attention however, they are valid for some applications. Due to the formation of an electrical double layer at the interface of adhesive/adherend, electrostatic forces are developed, and it is assumed that these forces provide resistance to the separation of the materials. The electrostatic mechanism is a valid theory in the case of metal-polymer adhesion bonds.

Diffusion theory is plausible when both adhesive and adherend are polymeric materials and miscible with each other due to the presence of long-chain molecules capable of movement. Therefore, adhesion is achieved with the interdiffusion of molecules between adhesive and adherend [5], [7].

3.1.4. Chemical bonding theory

Considering this theory, adhesion is based on chemical bonding such as covalent, ionic, and hydrogen bonding formed across the adhesive/adherend interface. Generally, four types of interaction can take place during chemical bonding: covalent bonds, hydrogen bonds, Van der

Waals forces, and acid-base interactions. Covalent and ionic bonds provide significantly higher adhesion values compared to secondary forces such as hydrogen bonds [7].

Regarding the chemical bonding between metals and polymers, close contact and good wetting conditions are mandatory as molecular forces are relatively short-range. In general, the low surface tension of polymers and the pitfall topology of metallic oxide surfaces make the intimate contact of molecules more difficult. However, thermal stimulation of molecular mobilities during the laser joining process improves this condition.

For example, in the case of Al^3-PP^4 bonding at the interface, besides Van der Waals forces and hydrogen bonding, a covalent coordination bond between alumina (Al^{3+}) and the carboxylate groups (COO^-) is reported. As the chemical bonding developed at the metal/polymer interface is stronger than the Van der Waals forces of polymers, cohesive failure is commonly observed for the metal/polymer assemblies. Considering practice in the experimental condition, the adherence force is increased by the contribution of mechanical interlocking due to the presence of large and deep open porosities in the metallic oxide layer, high fluidity of the molten polymer, and the application of clamping pressure [8].

Studying the interface of different metals and PI^5 via the deposition of metal, the nature of the chemical bond depends significantly on the valence structure of the polymer and the work function of the metal [9]. For instance, the chemical reactivity between the metal and polymer depends on the number of the d valence electrons in the metal. Therefore, a strong chemical reactivity between Cr^6 or Ti^7 to PI is reported while Ni^8 and Cu^9 bonding to PI is weaker. It is also worth mentioning that for the latter case, the coverage of metal on the polymer is incomplete and in island form.

In this regard, the metal-Cr-O-plastic chemical bond is reported for 304 SST^{10} laser-joined to PET^{11} or $PA66^{12}$ [10], [11]. Zn-O-C bond for ABS^{13} laser-joined to Zn^{14}-coated steel [12].

---

[3] Aluminum
[4] Polypropylene
[5] Polyimide
[6] Chromium
[7] Titanium
[8] Nickel
[9] Copper
[10] Stainless steel
[11] Polyethylene terephthalate
[12] Polyamide 66
[13] Acrylonitrile butadiene styrene
[14] Zinc

Al which is a metal with p valence represents an intermediate bonding strength and chemical reactivity between that of Cr and Cu [9], [13]. In the case of chemical bonding between Al and PI, Al breaks the C=O bond by forming a C-O-Al complex [9]. It should be noted that these studies were based on the deposition of metals on the polymer under a controlled environment. To study the produced interfaces by joining techniques under ambient conditions, identifying the bonds is much harder due to surface oxidation and contaminations. For example, for laser joining of Ti to PET, no evidence of a Ti-C bond is found [14], while the formation of Ti-F and Ti-C is suggested for Ti laser-joined to PVDF[15] [15], Ti-F bond for Ti/Kapton FN interface [16], Ti-C and Ti-O for Ti/PI, and others reported on the Ti-C bond for Ti/PET [17].

3.1.5. Weak boundary layer theory

Based on this theory, the failure at the adhesive/adherend interface is due to a cohesive break or a weak boundary layer. Weak boundary layers are due to the weak attachment of impurities to the substrate, and they can be formed from the adhesive, the adherend, the environment, or a combination of them all resulting. Some examples of weak boundary layers are PE[16] or metal oxides. PE has a low molecular weight component which is uniformly distributed in the polymer. Therefore, it is also present at the interface and is responsible for the low-stress failing of the polymer when it is used as an adhesive. Some metal oxides are not strongly attached to the base metal and the failure can happen cohesively within the oxide. In the case of Al, the oxide is strong and does not reduce joint strength [5], [7].

3.2. Joining technologies for metal/polymer assemblies

To make the best use of metals and polymers' diverse properties in lightweight hybrid structures, advanced joining methods must be applied. The joining methods of metals to thermoplastic polymers can briefly be divided into In-Mold Assembly[17] and Post-Mold Assembly[18] technologies [18].

In IMA or injection molding, the metal part is placed in the cavity of the mold before the injection molding process of the polymer. To improve the performance of the injection-molded assemblies, researchers proposed several surface treatment processes. Some of them are as follows [19]:

---

[15] Polyvinylidene fluoride
[16] Polyethylene
[17] IMA
[18] PMA

- Surface treatments rely on roughness and improvement of mechanical interlocking which happens between the molten polymer infiltrated in the micron-size roughness features of the metal surface.

In this regard, the creation of a porous oxide layer coated by Plasma Electrolytic Oxidation[19] and improvement of the mechanical properties is discussed for Al/PBT GF30[20]. The shear strength of 3-8 MPa is achieved with 7-20% surface porosity. Micro-mechanical interlocking is reported as the decisive joining mechanism [20]. In another study, electrochemical surface treatment for injection-molded Al/PA6 GF30 assembly is studied and the micro-structures and roughness parameters on the metal surface are presented as the parameters to affect the bond strength [21]. The laser ablation process is also used for this purpose [22].

- Surface treatments employ primers as adhesion promoters which act as coupling agents.

Silane is a well-known coupling agent in the industry. The silane coupling reactions are: the production of hydrogen due to hydrolysis of the alkoxy group; formation of the hydrogen bonding at the interface of metal/polymer; condensation of the functional groups at the interface; and chemical reaction at the interface of metal/polymer and the formation of bonding [23].

- Surface treatments use a chemical modification of the thermoplastic material to promote adhesion to metal.

It can be done via the formation of polymer blends or a direct change in the monomer chemistry. Regarding the former, the chemical modification of polyamide by blending with self-ordering poly-(ester amide) block copolymer is an example of increasing the adhesion to the metal. For the latter, adding styryl silane to the monomer of styrene is reported to provide the ability of direct bonding to Al upon polymerization [19].

- Other treatments to modify the physical and chemical characteristics of the metal surface.

For instance, Openair® plasma is used to modify the metal surface via cleaning, removing a weakly bonded surface layer, and potential chemical modification to promote bonding [19].

---

[19] PEO
[20] Polybutylene terephthalate-30% Glass Fibers

Mechanical fastening, adhesive bonding, and thermal bonding (welding) are classified in PMA. Figure 3.2 shows the joining techniques available for metals/polymers joining.
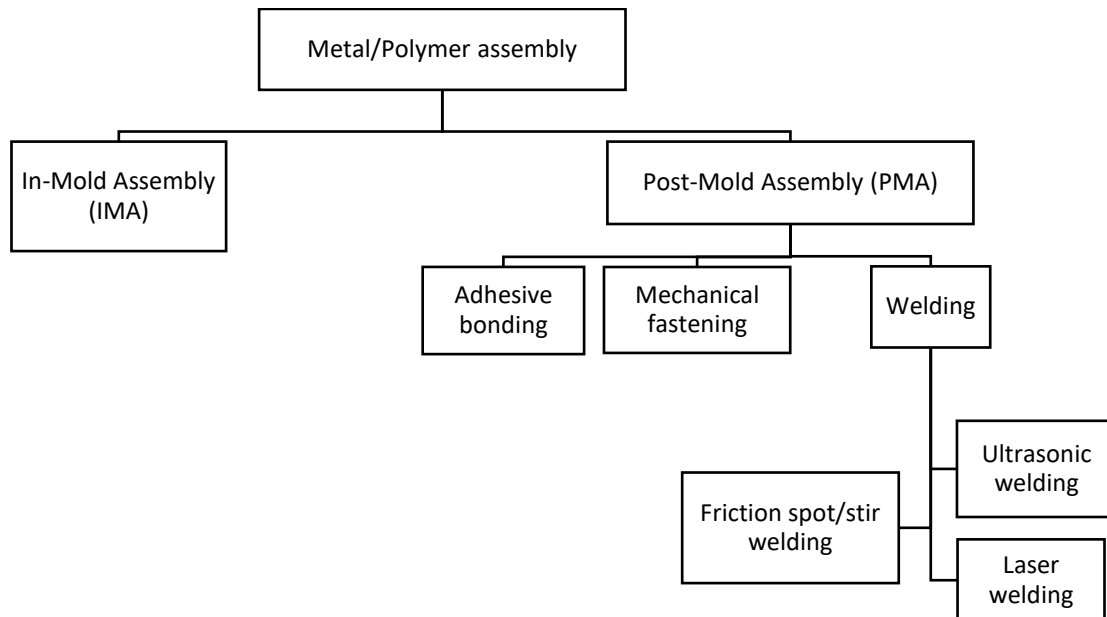
Figure 3.2. Joining methods for dissimilar materials [24].

3.2.1. Adhesive bonding

Adhesive bonding provides unique weight reduction with homogeneous stress distribution during loading. The fundamental of adhesive bonding (as a solid-state joining method) is the formation of intermolecular forces between the workpiece and the adhesive. The adhesive is generally a polymeric material with additives. The chemical reaction of the bonding process starts with the exposure of the adhesive to air followed by hydrogen or covalent bonding between the cured adhesive and the workpiece [7], [25].

However, it represents certain disadvantages such as the inability to disassemble without damaging the parts, and the susceptibility of the joints to environmental degradation such as moisture, humidity, and temperature. Therefore, the assessment of failure behavior for adhesive bonding is complex and this technique is not reliable in terms of long-term durability for engineering structures [24], [26]. To achieve successful adhesive bonding, surface cleaning is crucial. It can be implemented by several processes i.e., chemical etching, plasma etching, corona oxidation, acid etching, anodization, sandblasting, priming, solvent cleaning, and degreasing [3].

3.2.2. Mechanical fastening

Fasteners such as screws, bolts, washers, rivets, or the use of integrated design elements like snap-fit or press-fit joints are used in mechanical fastening [27]. No surface preparation is

needed, and the components can be disassembled in case of necessity, which are the main advantages of this technology. However, increasing component weight and the development of stresses around fastener holes that result in strength deterioration and corrosion susceptibility are the limitations of the technology [28].

3.2.3. Welding

As a fusion joining process, welding employs heat for the formation of the joint. It is suitable for both similar and dissimilar materials and can be implemented to achieve a solid-state joint with minimum or no microstructural changes. It is often challenging to weld metals to polymers directly due to the significant structural dissimilarities of these materials [29]. Macromolecules held together by Van der Waals forces are the structure of polymers while, metals are densely packed crystal structures with high cohesive energy [3], [29]. Therefore, the solubility of metals in plastic is noticeably low, as metals incline to form clusters instead of mixing uniformly when embedded with polymers. In addition, the melting temperature of metals is considerably higher than that of polymers therefore, far before metals are melted, polymers tend to degrade [29].

Polymers are classified as thermoplastics, elastomers, and thermosets and welding can be only implemented on thermoplastic polymers. Thermosets and chemically cross-linked elastomers cannot be reshaped by heating as they are characterized by an irreversible cross-linking reaction. Therefore, they tend to degrade by means of heat. Nevertheless, thermoplastics and thermoplastic elastomers can be softened and melted by heat because of the weakening of the Van der Waals and hydrogen bonding forces among interlocking polymer chains. This phenomenon explains the possibility of welding thermoplastic polymers [29].

Conventional welding processes like different types of arc welding are not applicable in the case of metal/polymer joining due to high energy input. There are several welding techniques for metal-polymer assemblies that have been addressed and studied by researchers. For instance, Friction Spot Joining[21] and the effective parameters on the bonding area and mechanical performance for Al/Carbon-Fiber-Reinforced Polymer[22] assemblies [30], and the effect of different surface treatments (mechanical, chemical, and electrochemical based) on the mechanical properties of FSpJ are discussed [31]. Ultrasonic welding for Al/CFRP was studied to increase the mechanical properties of the assemblies [32]. The effect of surface treatment and micro-mechanical interlocking is also reported for Al/ABS assemblies [33].

---

[21] FSpJ
[22] CFRP

Table 3.1 represents a brief comparison between different available joining techniques for metal/polymers assemblies emphasizing the advantages and disadvantages of each process.
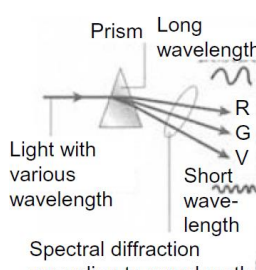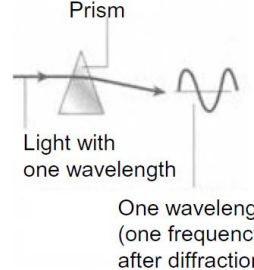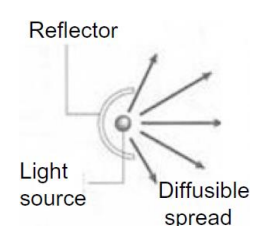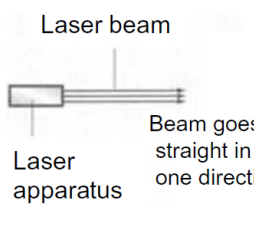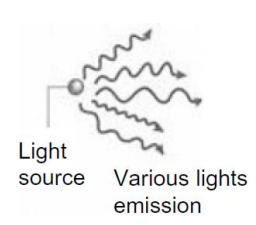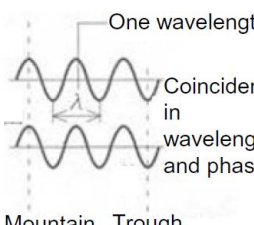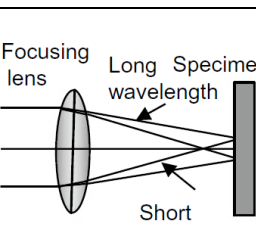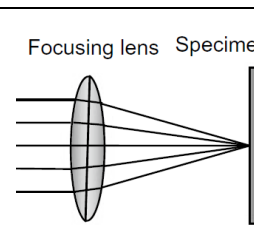
Table 3.1. The comparison between different joining techniques for metal/polymer assemblies [3], [24].

Joining techniques	Advantages	Disadvantages
Adhesive bonding	Uniform contact between the materials, therefore low-stress concentration and improved fatigue resistance, airtight joints, no extra weight to the assembly	Disassembling is not possible or difficult, surface pre-treatment is needed, long curing time, the joints undergo environmental and thermal degradation and the bond failure cannot be predicted
Mechanical fastening	The inspection, disassembly, repair, or replacement of the components are easy, no surface treatment is required	Extra weight to the assembly due to joining components, stress concentration around the holes, low corrosion resistance, both sides of the joint should be accessible, need extra components to provide sealing
Ultrasonic joining	Autogenous (no filler material is required), automation capacity, energy efficiency	Not environmentally friendly (very loud process), expensive machinery, the possibility to damage electrical components
Friction stir joining	Less heat input compared to the other welding techniques, therefore a solid-state joining	Low astatic due to the remaining visible hole in joint parts, high-cost machinery, and fixture
Laser joining	Fast process, therefore, small HAZ and low distortion, automation capacity, astatic joints	Expensive machinery

3.3.   LASER fundamentals

The word LASER is the acronym for "Light Amplification by Stimulated Emission of Radiation". Lasers present unique features compared to natural light. They are described in table 3.2 [34]. Lasers present miscellanies characteristics and hence applications in different fields. Still, it is tried to discuss mostly laser joining/welding for industrial applications in this report.

Table 3.2. The comparison between laser and natural light [34].

Item	Natural light	Laser	Applications
Monochromaticity			Spectroscopic analysis Isotope separation
Directivity			Optical communication Laser scanner Optical disk Laser radar
Coherency			Holography Precision measurement due to the interference fringe
Focusing/High intensity			Laser processing Laser scalpel Laser weapons

A laser consists of the following elements which are illustrated in figure 3.3:

- Laser medium:
- Pump source
- Laser resonator [35]
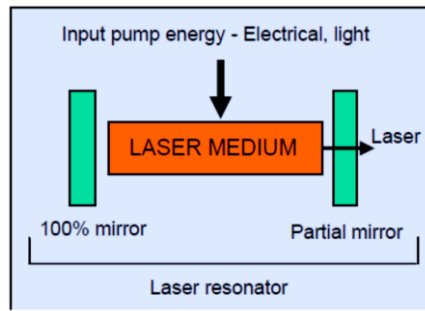
Figure 3.3. Illustration of laser elements [35].

Figure 3.4 shows the steps of laser beam generation which are described as follows:
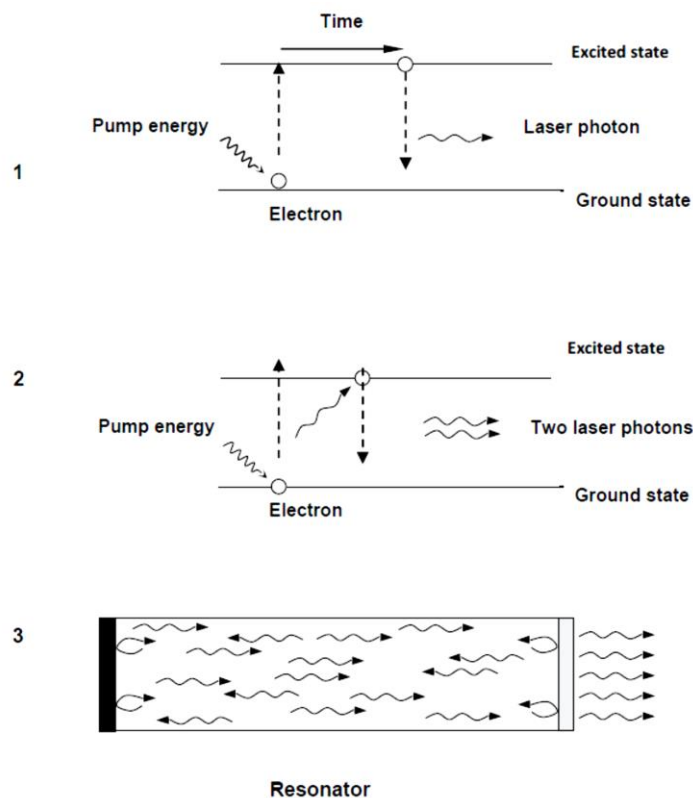
Figure 3.4. different states of laser beam generation [35].

1) Spontaneous emission: the energy input from the pump excites the laser medium atoms and the electrons are temporarily elevated to higher energy states. Nevertheless, the excited state is not stable, and the electron drops down to lower energy while losing the excess energy by emitting a photon.

2) Stimulated emission: in a very short time, the photons emitted by spontaneous emission collide with other electrons in the higher energy state and knock them to a lower energy level. This process creates another photon. The two photons are coherent meaning they are in traveling in the same direction and phase of the same wavelength.

3) Amplification: some of the emitted photons are moving along the laser medium thus the mirrors of the resonator reflect them back through the medium. Finally, amplification occurs when the percentage of atoms in the excited state is higher than those in the lower energy state [35].

3.3.1. Absorption, transmission, and reflection of laser energy

A unique characteristic of laser beams for materials processing is the ability to deliver high irradiance values on a small spot of a workpiece that provides rapid heating in a very small region. This is a route of many applications in materials processing [36]. During the incidence of the laser beam on a material, absorption, reflection, transmission, refraction, and scattering can take place. Equation 3.2 and figure 3.5 explain these different phenomena [34].

$$A = 1 - R - T \tag{3.2}$$

A: absorption coefficient
R: reflectivity
T: Transmittance
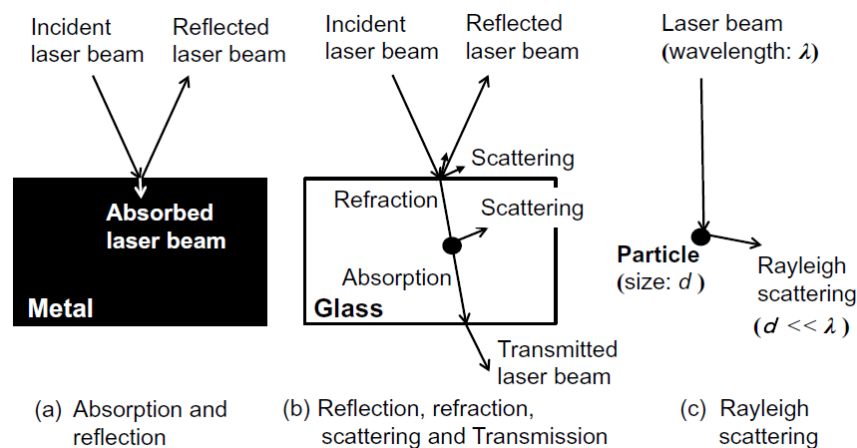
Figure 3.5. Absorption, transmission, reflection, and scattering of laser energy [34].

The reflectivity of the material's surface to the laser beam is an important parameter that affects laser processing. Reflectivity is a dimensionless value from zero to one and is defined as the ratio of the reflected power from the surface to the initial incident power. The reflectivity of metals is often high and it has a direct correlation with electrical conductivity [36].

Figure 3.6 represents the absorptivity of some metals versus the wavelength. In general, the absorption and wavelength show a reverse relationship. The absorptivity is also a function of temperature, and it increases with the rising in temperature until it reaches a maximum when the keyhole is created [34].
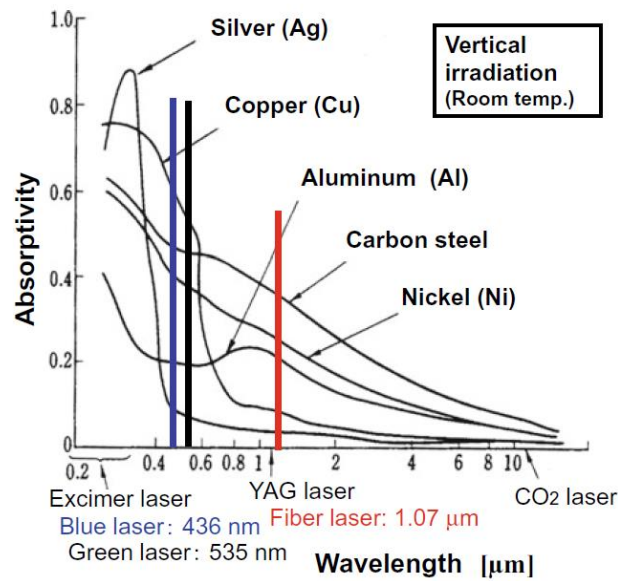
Figure 3.6. Absorptivity of some metals for laser sources with different wavelengths [34].

3.3.2. Pulsed and continuous operation

The laser beam can be applied in two operating modes regarding the duration of the emission.

- **Pulsed wave (PW):** it is a series of pulses with defined pulse width and frequency. The pulsed laser refers to a laser that emits a peak power much greater than its average power.

- **Continuous Wave (CW):** the laser beam is emitted with a stable average power over time. A CW laser can also produce pulses of laser. However, the peak power does not exceed the average power of the laser. This process is known as modulated output [35].

The difference between PW, CW, and modulated output is presented in figure 3.7.
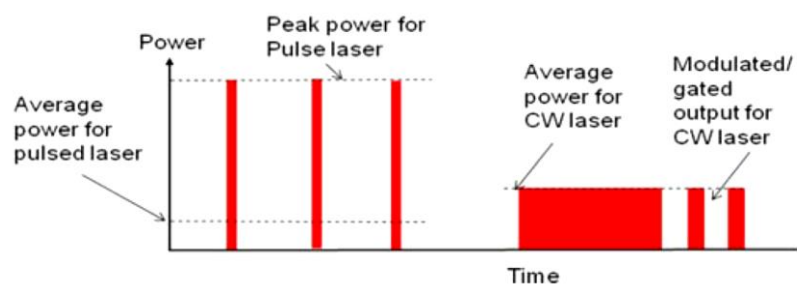
Figure 3.7. PW, CW, and modulated output of a laser beam [35].

3.3.2. Lasers in the industry

Based on the medium, industrial lasers are classified into gas, liquid, and solid-state lasers. In terms of easier operations, solid-state lasers are the best. For instance, the laser beam in YAG[23]

---

[23] Yttrium-Aluminum Garnet

laser with 1.06 μm wavelength, diode laser with 0.5 to 2.2 μm wavelength, disk laser with 1.03 μm, and fiber laser with 1.07 μm wavelength can be delivered with optical fibers up to 200 m distance [34].

Table 3.3. Industrial lasers for joining applications [34].

	Wavelength [μm]	Laser media	Average power [CW]	Efficiency [%]	Advantages
CO_2 laser	10.6	CO_2-N_2-He mixed gas	Max 45 kW, normal 0.5-12 kW	10-20	Achieving high power is easy
Lamp-pumped YAG laser	1.06	Nd^{3+}:$Y_3Al_5O_{12}$ garnet	Max 10 kW, normal 50 W-5 kW	1-4	Fiber-delivery and flexibility
Diode laser (LD)	0.8 – 1.0, blue laser 0.45	InGaAsP, Al(In)GaAs, etc	60 kW, blue laser 2 kW	20-50	Compact, fiber delivery, and high efficiency
LD-pumped solid-state laser	1.06	Nd^{3+}:$Y_3Al_5O_{12}$ garnet, etc	13.5 kW, PW 6 kW	10-20	Fiber delivery, high brightness, and high efficiency
Disk laser	1.03	Yb^{3+}:YAG or YVO_4, etc	16 kW	15-25	Fiber delivery, 4 branches, high brightness, and high efficiency
Fiber laser	1.07	Yb^{3+}:SiO_2, etc	Fiber-coupling 120 kW Max, single-mode fiber laser 10 kW Max	20-50	Compact, fiber delivery, high brightness, and high efficiency
Green laser	0.515, 0.532, 0.535	Nonlinear optical crystal from disk, YAG, or fiber laser	3 kW, PW 500 W	5-20	Short wavelength, high absorption for Cu
Ultrashort pulse laser	0.8-1.6	Titanium-sapphire, fiber, and disk laser	Max 1 kW, normal 1-100 W	-	Ultrashort pulse, extremely narrow HAZ

High-power lasers were initially developed in CO_2 laser and then YAG laser. Other lasers such as XeCl (308 nm), KrF (238 nm), and ArF lasers (193 nm) are mainly developed for other applications like drilling or cutting of polymers, glass, etc. In the twenty-first century, disk and fiber lasers with high power, high quality, and high efficiency were established for welding and cutting applications. These lasers are using high-quality high-power diode lasers as pumping sources. Recently, ultrashort pulse lasers (picosecond and femtosecond), second harmonic lasers (green laser from YAG, disc and fiber lasers), and blue diode lasers were

developed. The main applications for ultrashort pulse lasers are drilling and lap-joining of glasses while green and blue lasers are used for welding copper and other reflective materials. Table 3.3 summarizes the characteristics of lasers for welding and joining applications [34].

3.4.   Laser welding

Laser welding is a non-contact, fast and accurate process. Laser welding requires to be directed only on one side of the joint. It uses no consumables to be maintained or replaced. The only limitation is the reflectivity of metals. For instance, Cu will reflect more than 90% of laser energy at the wavelength of 1064 nanometers which belongs to industrialized Nd: YAG lasers.

Some advantages of the laser welding process are as follows [37]:

- Control over the delivery of energy into the weld area is exceptional; therefore, Heat Affected Zone (HAZ) and the distortion of the parts are minimized.
- The welding process is reliable and stable.
- The processing speed is relatively high, and the application of a scanner enables the process to achieve the maximum capacity of the laser.
- Welding reflective, conductive, and dissimilar materials are possible.
- The weld is clean which means that in addition to the aesthetic point of view sterilizing or fitting into other assemblies is easier to achieve.
- Unlike soldering or brazing, laser welding can provide sound hermetic welds.
- Laser welding provides a high-strength joint with a minimum number of welds.

Based on the power density, laser welding is classified into conduction mode and deep penetration or keyhole mode (see figure 3.8) [36], [37].
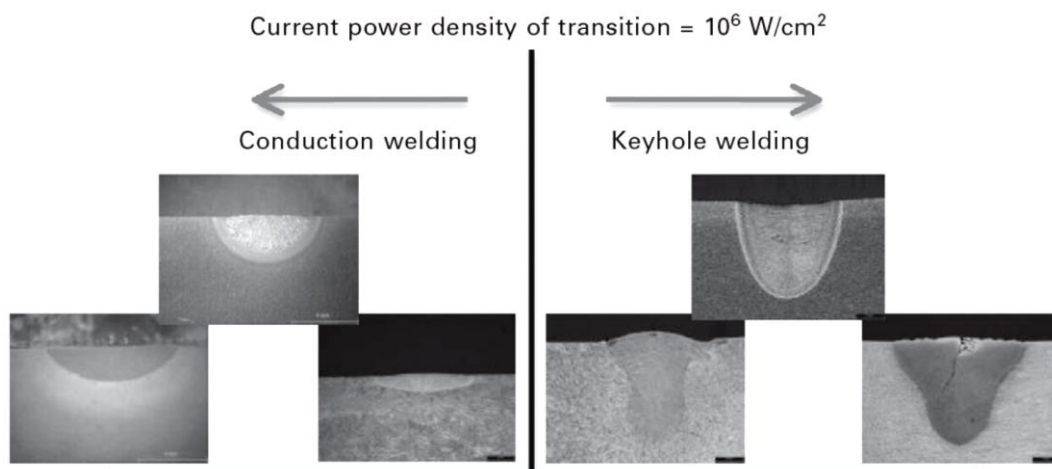
Figure 3.8. Conduction vs keyhole mode of laser welding [37].

3.4.1. Conduction welding

It is performed when the energy density is low (typically around 5×10^5 W/cm^2) with a shallow and wide weld bead. This mode of welding is common in applications that require an aesthetic surface or when particulates are a concern, for example, in certain battery sealing applications. For typical ferrous alloys, the penetration of conduction welding is not more than 0.3 mm [35], [36].

3.4.2. Keyhole welding

When irradiance (power density) is approximately 10^6 W/cm^2 or more, the interaction between the laser beam and the metal results in the vaporization of the metal producing a cavity or a keyhole inside the melt pool. The surface of the molten material will deform due to surface tension gradients and the recoil pressure of the metal vapor. Therefore, the laser energy is trapped, and the absorption increases thanks to the multi-reflection of the beam inside the keyhole. The weld is deep and narrow with an aspect ratio greater than 1.5 [34]–[36].

3.5. Laser welding of dissimilar metals

Laser welding of dissimilar metals is one of the key factors to promote flexibility in design and production in the industry. Welding in keyhole mode is very effective to reduce the HAZ and increase the efficiency of the welding process. One of the main challenges regarding the welding of dissimilar metals is the formation of intermetallic compounds in case the weldments present low solubility in a solid-state [38]. Several researchers addressed the effect of intermetallic compounds on the properties of the laser joint assemblies for different material combinations [39]–[41].

Following the demand of the industrial partner, Cebi, a study is done on the laser micro-welding of Ni wire to the CuSn$_6$ bronze terminal. As Ni and Cu represent complete solubility in a solid state [38], the formation of intermetallic compounds is not an issue to be addressed. Therefore, to achieve the maximum tensile load for the joint assembly, the effect of different laser beam oscillations (linear, zigzag, and circular) was studied. In the optimum condition, a weld stronger than the Ni-base metal was achieved [42].

3.6. Laser joining of metals to polymers

Among welding technologies, Laser-Assisted Metal-Plastic[24] joining is absorbing significant attention in the automotive industry. This new technology is flexible and fast, can be automated

---

[24] LAMP

very well and the heat input is localized and low. LAMP joining was developed for the first time at Osaka University for the joining of stainless steel type 304 with PET [10].

Almost all the researchers agree that metal surface pre-treatment is mandatory to achieve a high-strength bonding [1], [43]–[47]. However, it is worth noticing that the surface pre-treatment of the polymeric partner for laser joining of metal/polymer is rare and it was done in a paper to increase the oxygen-bearing functional groups [48]. There are two mechanisms, which are anticipated to provide metal-polymer joining possibilities: mechanical interlocking and physicochemical bonding. The first mechanism is promoted by creating patterns or grooves with undercuts on the metallic surface, generated by the laser beam [45], [46], [49]–[51], by milling or machining [52], [53], or by abrasive blasting process [1], [54]. The physicochemical bonding is via Van der Waals forces or hydrogen bonding [55], [56], or the enhancement of the chemical reactivity with pre-oxidation [12], and anodizing processes [57], [58].

Several researchers reported on the temperature measurement [59], [60] and simulation of the heat distribution inside the materials [46], [61]–[63] during the laser joining process in order to avoid degradation of the polymeric partner. However, the degree of polymer degradation and the size and distribution of the consequent bubbles is controversial.

Based on the laser transparency of the polymer, the LAMP joining can be categorized into two subdivisions. The irradiation of the laser source heats the metallic surface either directly or through the transparent plastic material, which in turn melts the polymer via heat conduction. In both cases, the metal remains solid.

3.6.1.   Laser Transmission joining[25]

The polymer should be highly transparent to the wavelength of the laser beam. A transparency of at least 60% is required for LTJ. The joint area can be directly heated by laser radiation through the polymer without any damage to the polymer [47], [59], [64]–[66].

3.6.2.   Direct laser joining or Laser Conduction Joining[26]

In this method, the laser targets the non-transparent partner which is the metal, and the heat is transmitted through the metal to the interface of the metal/polymer by heat conduction [4], [67]. The efficiency of the process is highly under the influence of metal thickness and heat

---

[25] LTJ
[26] LCJ

conduction properties [46], [53]. Figure 3.9 represents the LTJ and LCJ methods and the hypothesis of joining by bubble expansion.
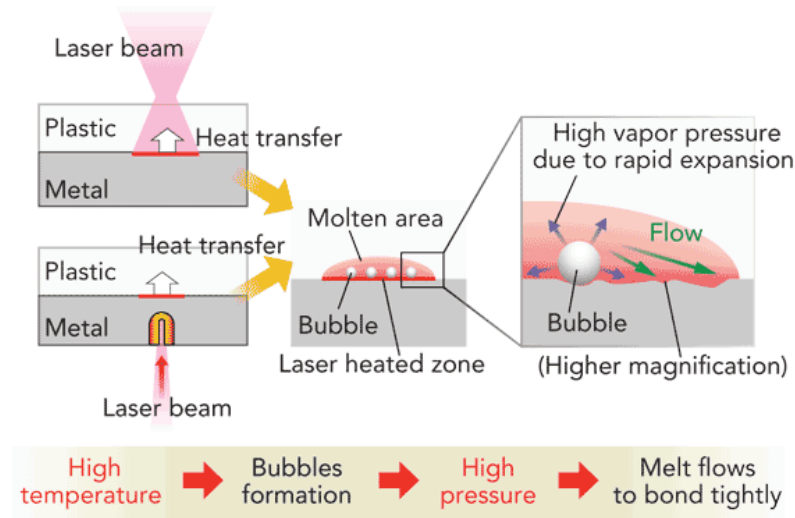
Figure 3.9. LTJ and LCJ and the formation of bubbles and their influence on the joining mechanism [66].

3.7. Technical and scientific gaps

3.7.1. Technical gaps

Due to several technical gaps, the application of LAMP joining is not well developed in the automotive industry although it can offer unique advantages over conventional joining techniques. The lack of specific standards regarding the sample preparation, laser joining process with miscellaneous parameters and mechanical testing make the results of mechanical properties optimization [68], [69] not usable for other applications. For instance, only a few researchers considered the effect of humidity on hygroscopic polymers like PA6.6 when laser-joined to metal [70]–[72] which alters the structure and consequently the mechanical properties.

Many researchers conducted their experiments with diode lasers in laser transmission joining configuration with a relatively large joining area between the materials [10], [73], [74]. On the one hand, engineering polymeric materials, and more specifically fiber-reinforced ones with dominant applications in the automotive industry, are not transparent to the available industrial lasers. Therefore, a systematic study on laser conduction joining is required. On the other hand, diode lasers do not provide high beam quality compared to fiber or disc lasers. Considering metallic surfaces are highly reflective to the near-infrared laser beams, using a high-quality beam helps to overcome the reflectivity issue and create a stable keyhole during the joining process which guarantees the repeatability of the process for industrial purposes. Moreover,

high beam quality enables the industry to design the parts with smaller overlaps and miniaturize the final assemblies.

3.7.2. Scientific gap 1

It is reported by Katayama et al. that the rapid expansion of numerous small bubbles due to the thermal degradation of polymer near the interface of metal/polymer is decisive to push the molten polymer inside the asperities of the metal's surface and created a reliable bonding [73]. In contrast, Schricker et al. discussed the expansion of the polymer during the melting process which increases the clamping force between the materials [75]. This effect would be enough to provide intimate contact between the materials without the presence of bubbles.

Other researchers reported on the minimization of the bubbles with the aid of ultrasonic vibration or modifying the clamping design and achieving joint strength three to four times higher than state-of-the-art [76], [77]. The presence of some micro-cracks is also reported around bubbles [78]. Therefore, the first scientific gap is to study the bubble formation near the interface of metal/polymer and the consequent effect on the performance of the assembly. The effect of bubbles near the interface of metal/polymer can only be identified when compared to a bubble-free state.

3.7.3. Scientific gap 2

Following other joining techniques like injection molding [54], [79] many researchers tried to increase the surface roughness of the metallic partner with the laser beam to promote only the mechanical interlocking between the materials [49], [51], [67]. In an extreme case of relying on the mechanical anchoring effect, the polymeric partner fails during the mechanical tests due to the notch effect [80] or the metal fails due to the loss of cross-section [67]. Compared to the other surface treatment processes, laser-based treatments are interesting for industrial applications as they are non-contact and considerably faster (compared to chemical treatments). However, the following should be considered for laser-based surface pre-treatments available in the literature:

On the one hand, the effect of surface melting and formation of the nanostructure oxide layer which contributes to the physicochemical bonding between the materials is absent. On the other hand, during the laser conduction joining process, the heat is transferred from the metal surface to the polymer; therefore, due to thermal contact resistance, the negative effect of surface roughness on the heat conduction needs to be considered especially for miniaturized joints.

On the contrary, others reported finding no correlation between the surface roughness and the shear strength of the joints [18], [56]. In addition, some studies reported on the significance of physicochemical bonding compared to mechanical interlocking [56], [58], [81]. In this regard, Heckert et al. [81] addressed Al oxide as the main requirement for joining Al to PA and found a correlation between the tensile-shear strength of the assemblies and the thickness of the oxide layer.

Therefore, for laser-based surface treatments, the creation of the nanostructure and increasing the surface roughness are combined effects that should be addressed separately.

3.7.4.   Scientific gap 3

And finally, several researchers reported on the effect of metal surface pre-treatment on the improvement of the mechanical properties and achievement of cohesive failure for metal/polymer laser joining. As the failure is cohesive, the failure zone due to the thermal effects needs to be studied. Only a few studies reported on the structural modification of the polymeric partner due to the joining process [82], [83]. Unfortunately, in some research, the polymeric partner fails due to the large joining area and low thickness of the polymer [2], [18]. The bending of the polymer is also another reason for failing during the tensile-shear test [73], [84].

Therefore, the mechanism of cohesive failure and the structural modification of PA to improve the mechanical performance of the assembly are not discussed in the literature.

3.8.   Scientific hypotheses

3.8.1.   Scientific hypothesis 1

The thermal degradation of the materials due to the excessive heat input is detrimental to their performance more specifically when miniaturization and reduction of metal thickness are the targets. Therefore, the presence of bubbles near the interface of metal/polymer reduces the mechanical properties of the assembly. Reducing the contact resistance between the materials provides uniform heat transfer from the metal to the polymer. Therefore, smooth surfaces and an optimum laser joining process will avoid the thermal degradation of the polymer.

3.8.2.   Scientific hypothesis 2

The surface of Al is covered with a dense, passive oxide layer that protects the bulk of the metal from corrosion. Exposing the Al (untreated surface condition) to the molten PA, the contact and consequently joining are limited to the extreme surfaces of the materials. Therefore, with

the absence of the anchoring effect, the joints do not perform robustly due to a mixed adhesive/cohesive failure.

3.8.3.   Scientific hypothesis 3

The mechanical properties of the polymers represent a strong relationship with their structure. PA is a semi-crystalline thermoplastic, and its degree of crystallinity depends on the manufacturing process. The modification of PA crystallinity due to the melting and solidification that occurs during the joining process affects the integrity of the material. If the adhesion and anchoring effect are robust between the materials, the susceptible failure zone is inside the PA where the structure is modified during the joining process.

3.9.   Research Methodology

The thermal degradation of polyamide should be studied with in-situ heating observation to explain the temperature measurements during the joining process. The exact values of melting point and degradation temperatures recorded by in-situ observation and temperature measurements are not the focus of the study. It is due to the fact that the heating rate is not similar for different processes and recording the temperature with thermocouples presents intrinsic errors compared to the real contact between the materials. The goal is to identify the melting and degradation behavior of polyamide.

To study the contribution of mechanical interlocking and physicochemical bonding, abrasive blasting and laser-based surface treatments are considered.

The anchoring effect between Al and PA would be achieved with surface roughening of the metal via abrasive blasting. It is a mechanical-based surface treatment and a proper cleaning process after the blasting is mandatory.

The nanostructure oxide layer provides physicochemical anchoring places rather than mechanical ones. Laser-based surface treatment processes under ambient conditions are interesting to modify the surface roughness of the metal with the promotion of the nanostructured layer. The laser ablation process provides higher roughness, while laser polishing created a nanostructured oxide layer on top of a smooth surface. To observe the effect of the nanostructured layer, laser polishing under Ar[27] atmosphere and an abrasive polishing process can be considered.

---

[27] Argon

Finally, it is important to study the near-surface structure of PA and compare it to the structure after the joining process. Structural modification due to the joining process presents a contribution to the mechanical properties of the assembly. Therefore, the modification of the near-surface structure of PA should be examined.

4. Experimental procedure

4.1.   Materials and Equipment

For the study, aluminum 1050 with H24 temper (by Assan Alüminyum) and industrial-grade extruded polyamide 6.6 (by Dutec) were used. They will be addressed as Al and PA for simplicity. The sample surfaces were carefully wiped with ethanol (≥ 99.8%) to avoid any undesirable contaminations and dried in a hot air stream before further processing. Table 4.1 depicts the nominal properties of the materials in the study.

Table 4.1. The nominal properties of Al and PA were used in the study.

Property	1050-H24 Aluminum	Polyamide 6.6
Dimensions	$60\times30\times0.5$ mm^3 $60\times30\times1$ mm^3	$75\times25\times4$ mm^3
Density	2.71 g/cm³	1.15 g/cm³
Melting point	650 °C	260 °C
Modulus of elasticity	71 GPa	3.3 GPa
Tensile strength	100 MPa	85 MPa

As the humidity state of PA samples is not well-known and it affects the material's properties and consequently joint quality [23], PA samples were conditioned according to ISO 1110 standard (Plastics-Polyamides-Accelerated conditioning of test specimens) at 70 ± 0.5 ℃ temperature and 5 mbar pressure for different durations. Table 4.2 shows the weight measurements of the PA samples with different cycles of conditioning. The presented values are the average of four different measurements for several samples. After seven days, the humidity content is less than 0.05%. Therefore, this conditioning process has been selected to apply to PA samples before further treatments.

Table 4.2. Different conditioning processes for PA samples.

Sample	weight [g]
As-received	8.7861
After 5 days of conditioning	8.7266
After 6 days of conditioning	8.7216
After 7 days of conditioning	8.7188

4.2. Surface treatments

4.2.1. Aluminum

The surface treatments of Al are categorized into two main groups of laser-based and abrasive-based surface treatments with three levels of the arithmetic average of roughness profile[28]. Table 4.3 summarizes the surface treatment processes applied on as-received Al.

The laser polishing process aims to melt a very thin layer of the material on the surface and consequently reduce the surface asperities by surface tension. In the literature, the process is done under a controlled atmosphere to avoid the oxidation process [85], [86]. Nevertheless, as the presence of oxide on the Al surface is the goal here, the process is implemented under ambient conditions. In addition, to have a homogeneous melted layer and reduce the surface roughness effectively with a single-step process, a CW laser beam was applied while defocused from the focal point to reduce the power density. The corresponding parameters such as scanning speed were optimized by the design of experiments to minimize the Ra and avoid damaging the materials during the processes. The laser polishing process has been implemented with a CW fiber laser (TruFiber 400 - max power of 400 W - with the wavelength of 1070 nm equipped with Scanlab HS20 2D f-Ө scanner head to achieve a beam quality of $M^2=1.03$)

Table 4.3. Summary of Al surface treatments.

	Laser-based surface treatments			Abrasive-based surface treatments		
	Laser polishing	Laser ablation medium Ra	Laser ablation high Ra	Abrasive polishing	Abrasive blasting medium Ra	Abrasive blasting high Ra
Treatment media	CW laser beam	PW laser beam	PW laser beam	Diamond suspension	PA powder	Silicon carbide powder
Post surface treatment	-	-	-	Ethanol ultrasonic bath (10 min)	Ethanol ultrasonic bath (10 min)	Ethanol ultrasonic bath (10 min)

Regarding the laser ablation process, the idea is to treat the Al surface with a PW laser to evaporate the material in addition to melting. Consequently, it increases the surface roughness compared to the untreated samples. The laser ablation processes have been carried out with a PW TruMark 6130 laser machine (laser medium: Nd: YVO_4, wavelength 1064 nm, and beam quality $M^2<1.2$) under ambient conditions.

---

28 Ra

4.2.2. Polyamide

PA surface treatment by laser beam was done with a CW CO_2 laser (laser station TM020+ with a wavelength of 10.6 µm and max power of 25 W equipped with SCANcube 10 scanner head). Figures 4.1 shows the schematics of the laser-based surface treatments on the materials with the corresponding laser beam parameters implemented for the study. The appearances of the surface treatments are shown in figure 4.2.

		V [mm/s]	ΔY [mm]	P [W]	PF [kHz]	BD [mm]	O [%]	d [mm]
Laser ablation	medium Ra	1000	0.05	20 (P₀)	120	0.028	70	0
	high Ra	145	0.05	20 (P₀)	60	0.028	91.4	0
Al Laser polishing		2000	0.05	400 (CW)	-	0.08	37.5	3
PA Laser treatment		20000	0.01	25 (CW)	-	0.1	90	1

V: Scanning speed [mm/s]
ΔY: Track offset [mm]
P: Laser power [W]
PF: Pulse frequency [Hz]
BD: Beam diameter [mm]
O: Overlap [%]
d: Defocused distance [mm]
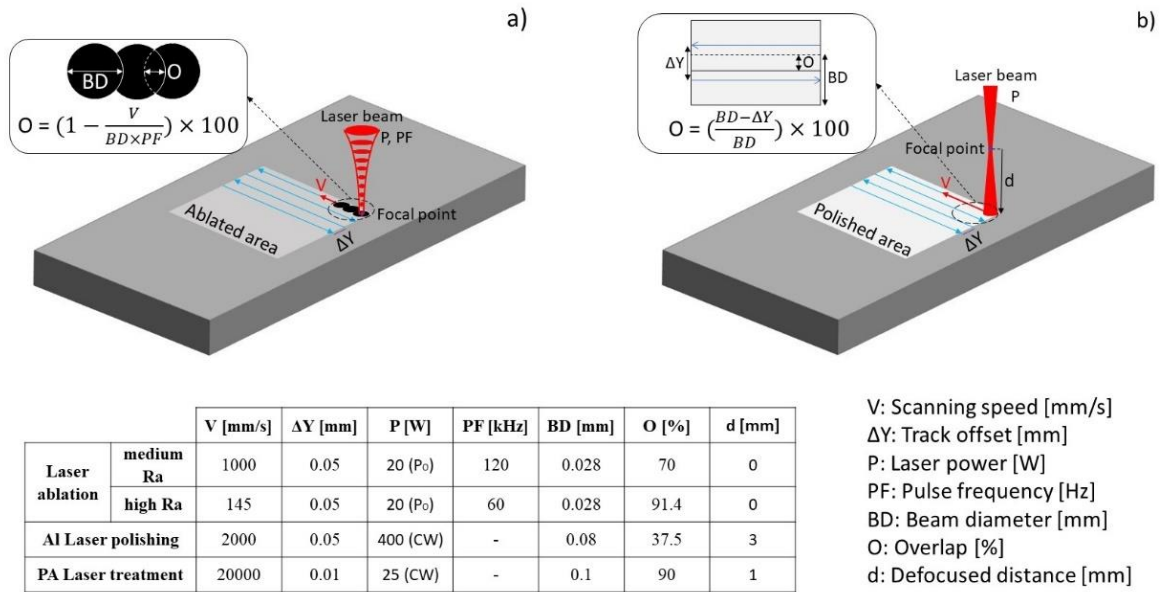
Figure 4.1. The schematics of a) laser ablation, b) laser polishing of Al, and laser treatment of PA, with the corresponding parameters,
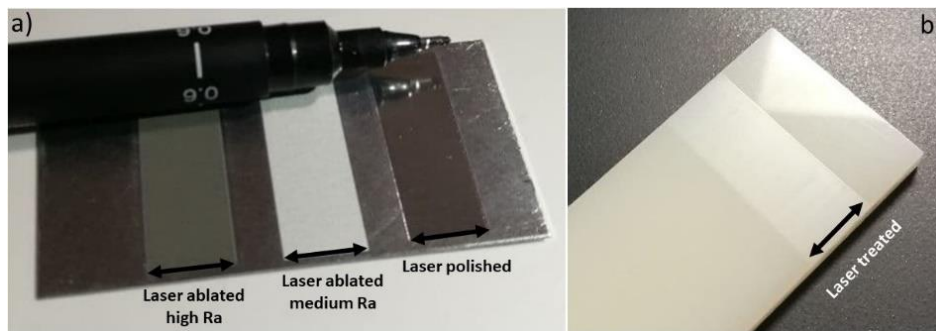
Figure 4.2. The appearance of surface treatments on a) Al, b) PA.

4.3. Laser joining process

4.3.1. Fixed process

For the laser conduction joining process which was also carried out with the fiber laser, the Al and PA samples are placed in an overlap configuration and the laser beam is applied from the Al side, while the pre-treated areas are aligned to face each other. As PA is not transparent to the laser beam, joining the assembly in a laser transmission joining configuration is not

feasible. The laser joining process is identical for all samples: the laser joining parameters and the clamping force (approximately 500 N) are kept constant and no shielding gas is applied. Figure 4.3 depicts the fixtures used for the laser joining process and the temperature measurements (which will be discussed in section 4.4) during the process.

Figure 4.3. The fixture for a) laser joining of the samples and b) temperature measurement during the joining process.
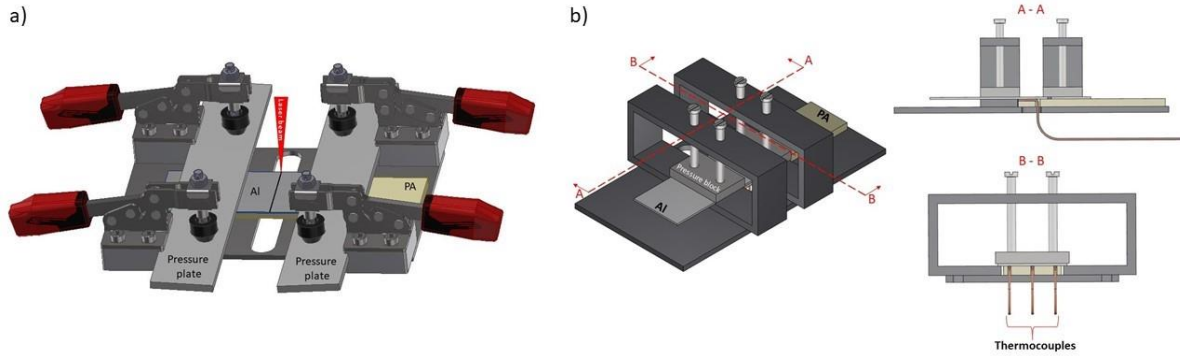
To better control the energy input to PA and widen the joining area, temporal and spatial modulations of the laser beam have been implemented. Figure 4.4 shows the joining configuration and the temporal and spatial modulations. Equations 4.1 and 4.2 explain the modulated power and spatial modulation of the laser beam, respectively.

$$\boldsymbol{P_{mod}} \; = \; \boldsymbol{t_{mod}} \times \boldsymbol{f_{mod}} \; \times \boldsymbol{P_p} \tag{4.1}$$

P_{mod}: Modulated power [W]
t_{mod}: Modulated time [s]
f_{mod}: Modulation frequency [Hz] $= \dfrac{1}{\text{Modulation Period [s]}}$
P_p: Peak power [W]

$$\begin{pmatrix} x \\ y \end{pmatrix} = \begin{pmatrix} a.\cos(2\pi f t + \varphi_x) + v_f t + a_0 \\ a.\sin(2\pi f t + \varphi_y) \end{pmatrix} \tag{4.2}$$

a: Amplitude [mm], a_0 t=0
$f_{x,y}$: Oscillation frequency [Hz]
v_f: Feed rate [mm/s]
$\varphi_{x,y}$: Phase angle in x and y direction (rad), $\varphi_x = -\pi$, $\varphi_y = 0$

The treated area covers the whole surface of the corresponding material with a width of 10 mm to avoid the contribution of the as-received area during the laser joining process of the treated samples.
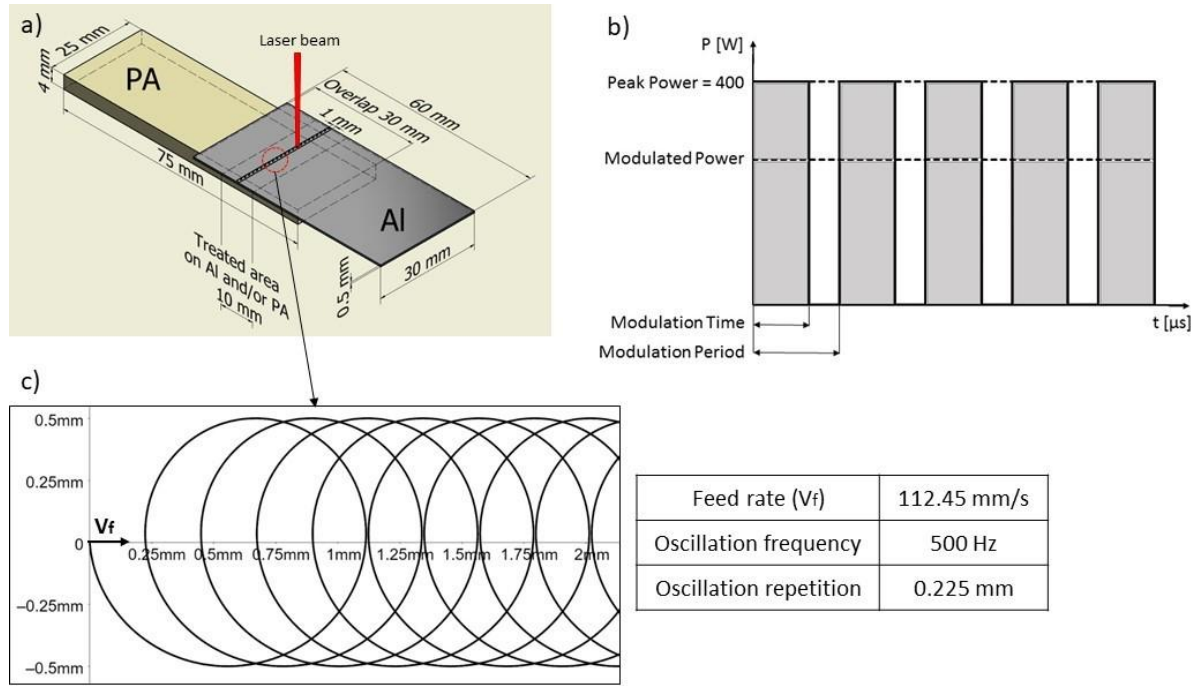
Figure 4.4. a) Joining configuration and the dimension of samples, b) temporal modulation, c) spatial modulation of the laser beam.

4.3.2. Laser joining with different feed rates

To study the effect of different joining speeds and consequently different cooling rates of the samples during and after the laser joining process, 1 mm thick Al samples (same standard of 0.5 mm samples) are laser-joined to PA with a linear trajectory of the laser beam. Table 4.4 shows the different feed rates with their corresponding laser power (CW) and the calculated energy input according to equation 4.3.

Table 4.4. Different feed rates (joining speed) and the corresponding power followed by the energy input for Al to PA joining.

Feed rate [mm/s]	CW laser power [W]	Energy input [J/mm]
2	148	74
5	176	35.2
30	260	8.6
60	328	5.4
90	352	3.9
120	388	3.2

$$Energy\ input\ [J/mm] \ = \ \frac{Power\ [W]}{Feed\ rate\ [mm/s]} \qquad\qquad (4.3)$$

4.4. Temperature measurement during the joining process

The temperature of the lower surface of Al (1 mm thickness) was recorded during the laser joining process to PA. for this purpose, the beam trajectory is zigzag oscillation with 1 mm

amplitude, wobble frequency of 50 Hz, and feed rate of 1 mm/s which is described in equation 4.4.

$$F(x) = \left| \frac{4af}{v_f}\left(x - \frac{v_f}{2f}\right) - 4a\left\lfloor \frac{f}{v_f}\left(x - \frac{v_f}{2f}\right)\right\rfloor - 2a\right| - a \qquad (4.4)$$

a: amplitude [mm]
f: oscillation frequency [Hz]
v_f: feed rate [mm/s]

To measure the temperature accurately during the process, a slow feed rate (v_f=1 mm/s) is required. Three cases of temperature measurement were considered. In the first case (case I), the joining process was tailored to keep the temperature below the melting point of PA for the whole process. For the second one (case II), the temperature should be between the melting and the degradation points of PA while, for the last case (case III), the temperature is always higher than the degradation temperature of PA.

Due to the employment of the laser beam in CW with a low feed rate, heat accumulation is inevitable. To moderate the heat accumulation for the temperature measurements, a power ramp for each case is defined as shown in Table 4.5. For all cases, the temperature is measured at three points (start, middle, and end of the joining area) between Al and PA with K-type thermocouples. The module NI 9219 used for the temperature measurements and recording of the temperature was carried out at a frequency of 50 Hz.

A parallel and a perpendicular cross-section (considering the laser path) of each case were prepared from the laser-joined samples. Figure 4.5 shows the schematics of parallel and perpendicular cross-sections.

Table 4.5. Power distribution for all cases of temperature measurements.

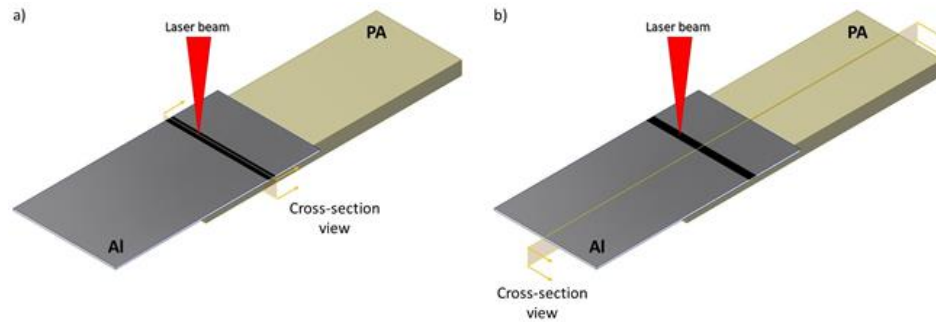|	Case I	Case II	Case III
Starting power	130 W	170 W	210 W
Power in the middle of the laser path	140 W	180 W	220 W
Power at the end	0 W	30 W	70 W

Figure 4.5. Schematics of a) a parallel and b) a perpendicular cross-section.

4.5.   Post-heat treatment

The post-heat treatment on the laser-joined specimen was implemented with a Memmert vacuum oven at 50, 100, 150, and 200℃ for 3 hours and a pressure of 5 mbar. The samples were cooled down in the ambient conditions for 30 minutes followed by the tensile-shear test. The post-treatment process was only implemented on laser-polished Al samples laser-joined to as-received PA.

4.6.   Characterization methods

4.6.1.   Microscopic techniques

Al and PA surfaces with different treatments were characterized by Environmental Scanning Electron Microscopy[29] with FEI ESEM Quanta 400 FEG and Optical Microscopy[30] and profilometry were done with Leica DM 4000 M and Keyence VHX-5000, respectively.

Transmission Electron Microscopy[31] imaging of Al was done by a JEOL JEM-2100 LaB_6 after lamella preparation using a FEI Versa 3D. Sample preparation includes the coating of Al with Pt[32] before using a Ga[33] ion beam for the lamella preparation. It should be noted that for laser-polished Al, an additional layer of amorphous carbon was deposited by evaporation before the Pt coating. Typically, the thickness of Focused Ion Beam[34] lamella is in the range of 60 nm.

Energy Dispersive X-Ray[35] mapping of Al/PA cross-section was performed on a TEM sample with Scanning Transmission Electron Microscopy[36] imaging at 200 kV accelerating voltage using a JEOL ARM200 CFEG equipped with a JEOL JED-2300 X-ray spectrometer.

---

[29] ESEM
[30] OM
[31] TEM
[32] Platinum
[33] Gallium
[34] FIB
[35] EDX
[36] STEM

4.6.2. X-Ray Diffraction

PA surface crystallinity was investigated by grazing X-Ray Diffraction[37] before and after the laser treatment using a Panalytical X'Pert PRO MPD system. The incident angle was set to 0.5° causing a penetration depth of 35 µm. The X-ray beam was generated at 40 kV and 45 mA through CuKα radiation (wavelength λ=1.54 Å). The diffractograms were recorded in the 2θ range of 5° to 50°, while the software Fityk was utilized to fit the experimental curves with the peak functions. To this end, the background signal was first subtracted, and then the amorphous scattering peak was positioned in the range of 21°-21.5°. The amorphous peaks were modeled with a Voigt function. Six crystalline diffraction peaks ((102)α at 13.1°, (200)α at around 20.4°, (001/20$\overline{1}$/200)γ at 22.4°, (002/$\overline{2}$00)α at around 23.6°, (202)α at around 38°, and an unknown weak diffraction or scattering peak at 41.2°) were modeled with Lorentzian functions [87]. From the area of each peak, the overall weight index of crystallinity (ratio between the sum of all crystalline peak areas and the sum of all crystalline peak areas and the amorphous peak area), and the weight fraction of each crystalline phase have been calculated.

4.6.3. X-ray Photoelectron Spectroscopy

X-ray Photoelectron Spectroscopy[38] (with Kratos Axis Ultra DLD) was performed on Al (as-received and laser-polished) and PA (as-received and laser-treated) to track a chemical modification of materials due to the laser treatment processes.

The X-ray beam is 150 W with an analysis area of 700×300 µm^2. The take-off angle is 0° and the calibration is performed through the C1s peak whose value is taken at 285.0 eV. Two tests were performed per sample to assess reproducibility. For each test, the energy resolution was 1.5 eV for the survey spectrum, and it was 0.6 V for the high-resolution spectrum, which was performed on Al, C, O for aluminum samples, and N, C, O for PA samples.

To identify the bonding between Al and PA for laser joining, XPS analysis was performed on fracture surfaces, and based on [88] it was tried to remove the extra PA by 2,2,2-trifluoroethanol from the fracture surface of laser-polished Al and reach the interface of metal/polymer (by floating the sample in the solution for approximately 15 hours).

4.6.4. Atomic Force Microscopy

The topography and nanomechanical properties were measured by Atomic Force Microscopy[39] with an MFP 3D infinity microscope from Asylum (Oxford instruments). Bimodal tapping

---

[37] gXRD
[38] XPS
[39] AFM

measurements were carried out in an amplitude modulation frequency modulation (AMFM) mode [89]. The probes were AC 160 R3 from Asylum Research, whose resonance frequency and force constant were approximately 300 kHz and 26 N/m, respectively. Three sizes of images were performed with a 128×128-pixel resolution: "low magnification" images with the size of either 40×40 μm^2 or 15×15 μm^2 and "high magnification" images with the size of 1×1 μm^2. Two samples were tested. The first sample is a PA that has been partly laser-treated, i.e., one part was laser-treated, and the other part was untreated. Since the surface nanostructure, probably assigned to crystallites, was not properly elucidated on the untreated area, a second sample was prepared by removing the first hundreds of nm of the surface (in thickness) by cryo-ultramicrotomy using a diamond knife. Imaging was done on the remaining flat block face of the material whose extremely low roughness enables to visualize of the intrinsic nanostructure. Thereby, the interface between the untreated and treated parts is better defined, and the topography amplitude is much reduced, which allows better nanomechanical analysis and, therefore better contrast between crystallites and amorphous volume. Microhardness tests were carried out by static indentation with a nano scratch tester (NST from Anton Paar). Indentation of 100 mN with a conosphere tip of 5 µm radius was performed. Residual imprints outside diameter were evaluated by optical microscopy and the corresponding hardness value was calculated as the ratio of the load divided by the imprint area.

4.6.5.   Micro-computed X-ray Tomography

Micro-computed X-ray Tomography[40] testing was performed to visualize the internal structure of the materials after the joining process. EasyTom 160 from RX Solutions has been utilized at 100 kV and 30 mA with a micro-focused tube (tungsten filament). The source-to-detector distance (SDD) and the source-to-object distance (SOD) were selected in such a way as to obtain a voxel size of around 3 µm. The reconstruction of the sample volume has been conducted with the software Xact64 after applying geometrical corrections and ring artifact attenuation. The imaging of the reconstructed volume of the assembly has been done with the software Avizo. The analysis is focused on the interfacial region between Al and PA.

4.6.6.   Time-of-Flight Secondary Ion Mass Spectrometry[41]

It was performed using an IonTOF TOF-SIMS 5 instrument, equipped with a bismuth cluster ion gun (Bi_3^+) for analyses and imaging. Moreover, the instrument is fitted with a dual-source sputter gun (Cs^+, C_{60}^+) for depth profiling and 3D imaging of materials.

---

[40] μCT
[41] ToF-SIMS

The technique uses a tightly focused primary ion gun (which provides a pulsed ion beam) to eject matter from the surface of the sample. Among the sputtered secondary particles, the sample emits electrons, neutral molecules/fragments, and elements; moreover, a minor proportion of positively or negatively charged molecules/fragments and elements (called secondary ions). These secondary ions are analyzed by a Time-of-Flight mass spectrometer. The average depth of analysis for a ToF-SIMS measurement is approximately 1 nm.

As the primary ion beam can be restored across the sample (typically over 500×500 μm^2), the individual spectra collected over this surface can be used for the retrospective image reconstruction of the lateral distribution of any secondary ion. In this study, the instrument was operated in analysis (static mode) and imaging mode, using both positive and negative detection modes.

4.6.7. Tensile-Shear test

Regarding different mechanical tests (tensile-shear, tensile, peel), metal/polymer assemblies present a better performance in tensile-shear followed by tensile tests. Therefore it is recommended to design the assemblies withstanding the tensile-shear loads [90].

The tensile-shear test on the joints was performed in a single-lap shear configuration using a Zwick/Roell machine with a maximum force of five kN. The test was done at a constant speed of 2.5 mm/min, free clamping length of 445 mm, and a fixture to limit the bending of the specimens. The fixture consists of CFRP material with a very smooth surface (Ra=0.02 µm) to avoid friction with the sample (see Figure 4.6). The reported values of tensile-shear load (maximum force during the test) are representative of at least ten individual measurements.
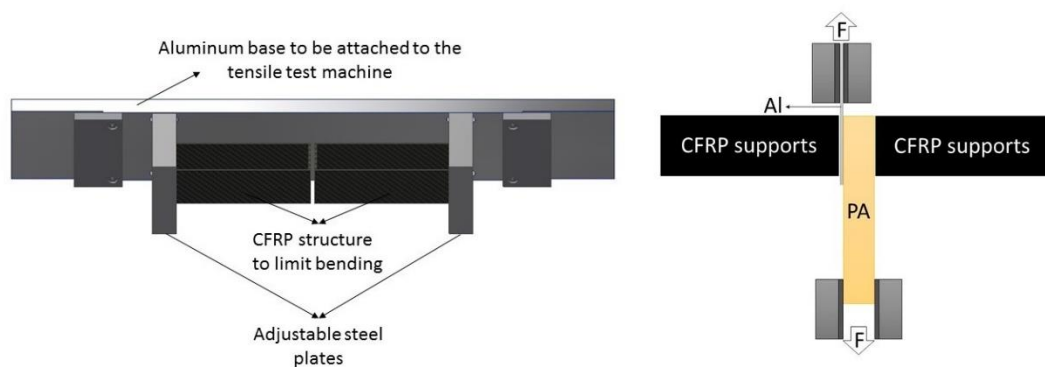

Figure 4.6. The schematics of the tensile-shear test with the designed fixture to limit the bending of the samples during the test.

4.6.8.   Roughness measurement

The Ra values of all the samples were measured using a Mitutoyo SJ-500P with a Stylus tip radius of 2 µm based on ISO 4288-1996. The reported values are representative of at least five individual measurements.

4.6.9.   Water contact angle test

To measure the contact angle of water to laser-polished Al and laser-treated PA surfaces for different aging times, the sessile drop test was employed. For each test, a water droplet with 2 µl volume was dropped on the surface of the materials.

5. Results and discussions

5.1.   In-situ observations

The first challenge of joining metal to a polymer with the laser beam is the significant difference between the melting points of the materials. PA is a heat-sensitive material, and it is important to observe its behavior while heating up. Therefore, based on in-situ heating observation, PA is characterized and consequently, the cross-sections of the Al samples laser-joined to PA are explained regarding different joining powers and thus, different temperatures at the interface of Al/PA.

However, there are several challenges to recording the exact temperature of the Al/PA interface during the joining process. Therefore, it is tried to design a process for recording the temperature and use the results to explain the cross-section of the joints followed by the mechanical properties and the main goal is not to report an exact temperature at the interface of metal/polymer.

To sum up, this chapter covers the in-situ heating observation of PA inside ESEM, temperature measurement of the Al/PA interface, and cross-section analyses of the corresponding samples.

5.1.1.   In-situ heating of PA observation inside ESEM

Figure 5.1 shows the images of ESEM in-situ heating. They represent the evolution of the PA melting process from room temperature to the melting range followed by the thermal degradation of PA due to excessive heat. The PA starts to melt at approximately 299 ℃ and at approximately 339 ℃ the thermal degradation is observed by bubble formation in the molten PA. According to [91], CO_2, NH_3, and H_2O are the gaseous products of PA thermal pyrolysis.
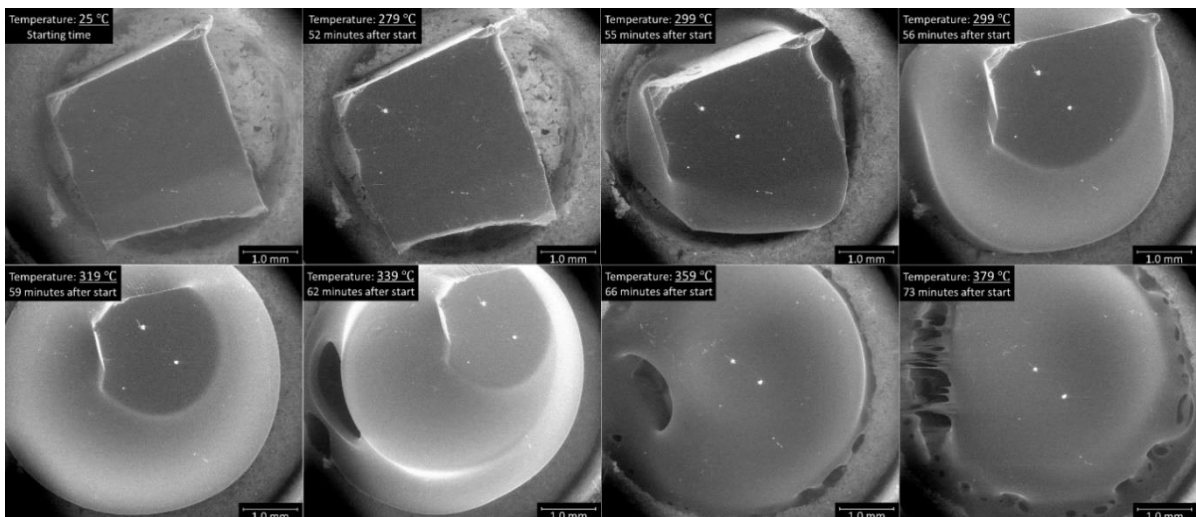

Figure 5.1. In situ ESEM heating observation for PA sample.

5.1.2. Temperature measurement

Based on in situ heating observation of PA, two critical temperatures are noted: the melting and the degradation temperatures of PA. With the designed process of temperature measurement (section 4.4 Temperature measurement during the joining process), the temperature was recorded. Figure 5.2 shows the temperature measurements for Al to PA laser joining for cases I, II, and III. In case I, the measured temperatures for all thermocouples are less than the melting point of PA while, in case II, they are between the melting point and the degradation temperature, and in case III, all the temperatures are higher than the degradation temperature.

The time of the laser joining process for all cases is 30 seconds, and the temperature is measured at the start, middle, and end of contact between Al and PA. The defined power ramp for each case was effective enough to keep a relatively constant temperature from one thermocouple to the next one. It is worth mentioning that without the power ramp, there is considerable damage to the PA at the end of the joining area for all cases and more specifically for case III.

For case I, as the measured temperatures are below the melting point of PA, no robust joint was observed on the cross-sections of the samples.
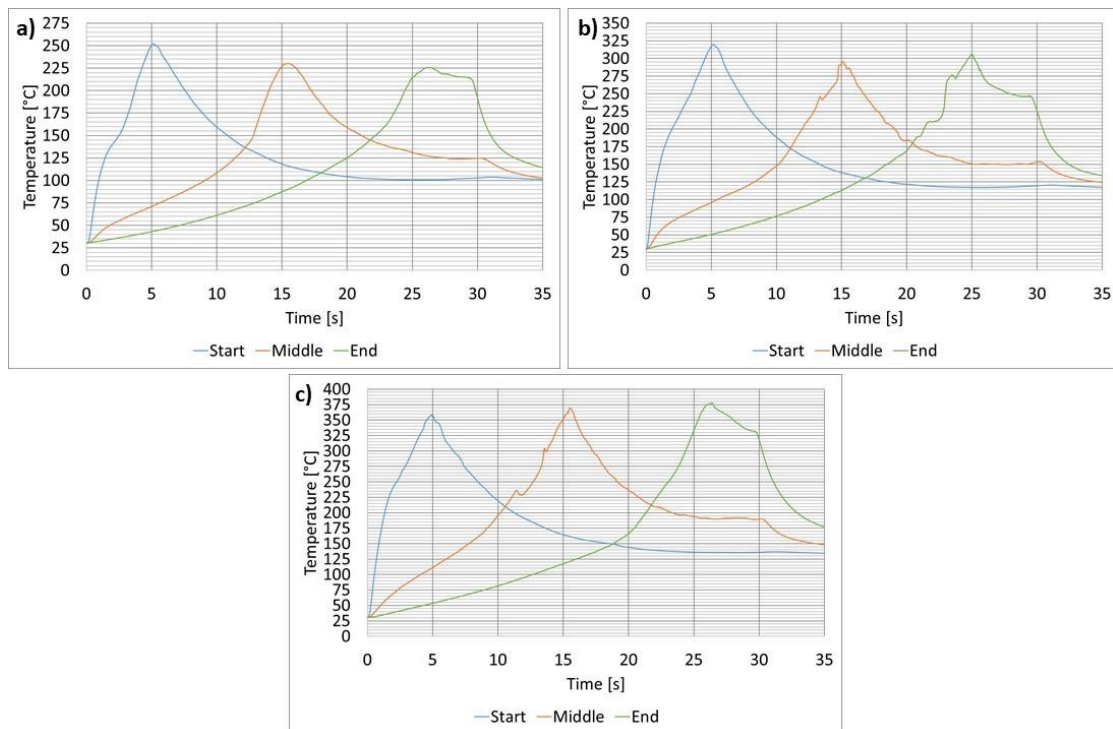

Figure 5.2. Temperature measurements for a) case I, b) case II, and c) case III.

Regarding cases II and III, figure 5.3 depicts the parallel and perpendicular cross-sections of the corresponding joined samples. For case III, the thermal degradation of PA all along the joining area is visible in the form of bubbles at the melted PA layer near the interface of Al/PA

(black areas). However, bubble formation is mainly avoided for case II. Yet, it is worth mentioning that in some samples small degradation areas of PA were observed. It most probably happened due to the heat accumulation caused by the slow feed rate of the process.
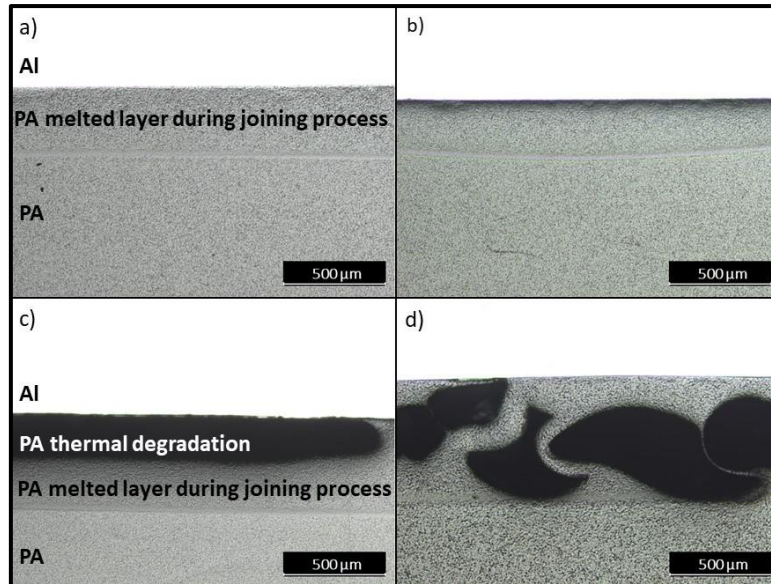

Figure 5.3. a) Case II parallel, b) case II perpendicular cross-sections, c) case III parallel, and d) case III perpendicular cross-sections.

Figure 5.4 shows the depth measurements of the PA melted layer (Y=0, the interface of Al/PA) from parallel cross-sections of samples laser-joined with the parameters of cases II and III. The measurements are done with optical microscopy on the cross-sections. The melted depth of case III is always higher than case II all along the contact area because of the higher temperature which leads to a higher volume of melted PA. Due to the high clamping force applied during the process, the depth of the melted layer is higher at the edges of PA, and it follows by the ejection of molten PA outside of the contact area which is more extreme in case III.
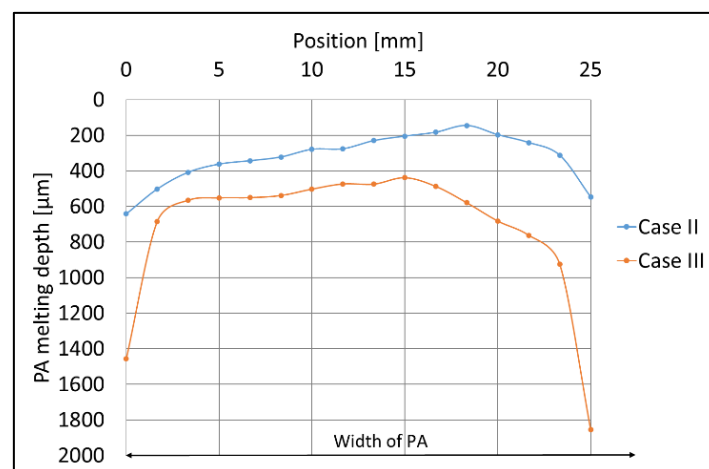

Figure 5.4. PA melting depth measurements from parallel cross-sections of cases II and III.

5.1.3.   Interim summary I

Considering the significant difference between the melting points of Al and PA and having in mind that PA is a heat-sensitive material, avoiding the thermal degradation of PA during the laser joining process is the first requirement to provide a robust joint with superior mechanical properties. Thanks to the exceptional control over the energy input of the laser beam, adjustments of process parameters are enough to reach an optimum condition and avoid PA thermal degradation. It is worth mentioning that all PA samples for this study are conditioned and possess a minimum level of moisture. Higher levels of moisture in the PA samples will enhance bubble formation during the joining process due to water vaporization.

5.2.   Adhesion between Al and PA

5.2.1.   Joining with different modulated powers

In the previous chapter, we observed the degradation of PA due to excessive heat input and followed this phenomenon in the cross-section observation of the joined specimens. As the joining process was specifically designed for accurate temperature measurement (low feed rate, complex fixture, 1 mm thick Al samples, etc.), to study the adhesion between Al and PA followed by the mechanical properties a new set-up of joining is designed (4.3.1 Laser joining-fixed process).

The thickness of Al samples is 0.5 mm in this chapter which is more challenging for the joining process due to the high reflectivity of Al to the near-infrared laser beam and the challenge to keep a stable keyhole on Al during the joining process without damaging the polymeric partner. The circular oscillation of the laser beam was selected to slightly enlarge the joining area and accomplish more robust joints for the mechanical tests. In the end, a high feed rate was defined which is more favorable to minimizing heat-affected zone[42] and providing a higher production rate. To provide a uniform heat input from Al to PA, power (temporal) modulation of the laser beam is employed.

Now it is interesting to observe and validate the degradation of PA in the cross-sections of different samples with the corresponding joining process. Figure 5.5 presents the shear load of the laser-joined samples with different modulated power. While the peak power is fixed at 400 W and the modulation period is 25 kHz, the modulation time varies from 20 μs to 34 μs in the steps of 20. Therefore, the modulated power varies between 200 to 340 W.
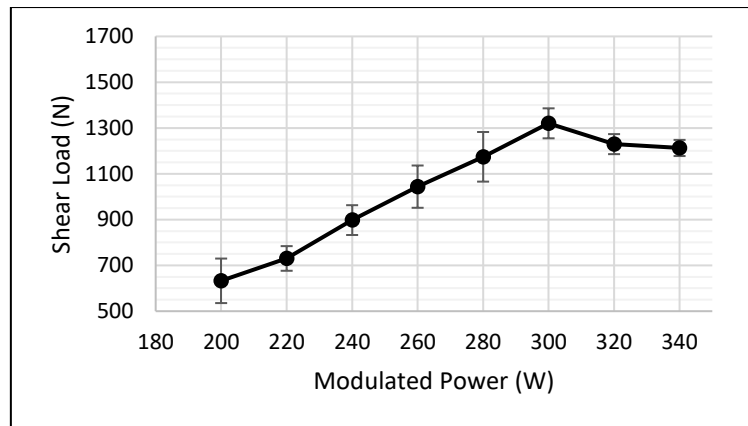
---

[42] HAZ

Figure 5.5. Shear load of the laser-joined samples with different modulated powers.

It is worth mentioning that laser joining with less than 200 W of modulated power does not provide a robust joint due to the lack of sufficient PA melting. Yet, Joining with higher than 300 W of modulated power damages the materials. Figure 5.6 depicts cross-sections of the joints with optimum and too much heat input. Figure 5.6a is the cross-section for a sample laser-joined with 280 W modulated power. As can be observed, the cross-section is free of bubbles. By increasing the modulated power, starting at 300 W, the thermal degradation of PA started which is observed in figure 5.6b as bubble formation. In contrast, to figure 5.3 (1 mm Al laser-joined to PA) and the presence of bubbles in the melted layer of PA, they are now in the Al. Severe degradation of PA remains an open cavity in the Al in the joining area and compromises the tightness of the joints. This fact makes the laser joining of thinner materials more challenging.
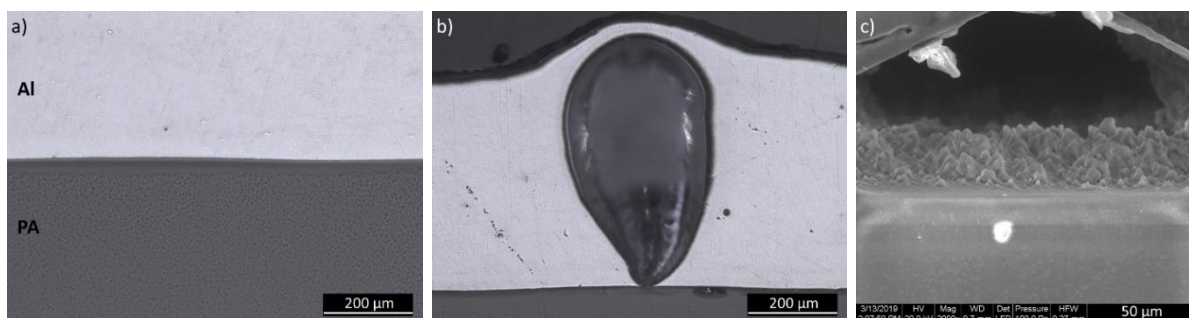

Figure 5.6. a) cross-section of the assembly laser-joined with 280 W, b) laser-joined with 300 W, c) ESEM image of PA surface at the degraded zone.

Therefore, the modulated power of 260 W was fixed to ensure that no degradation of PA happens during the laser joining process and investigation of the adhesion between Al and PA.

5.2.2. Ra measurements and microscopic observations for different surfaces

Figure 5.7 depicts Ra measurements for different Al surface treatments. As can be observed, Ra values can be categorized into four main groups: as-received condition with anisotropic

surface roughness values, medium and high Ra for laser-ablated and abrasive-blasted samples, and low Ra values for laser and abrasive-polished samples. Applying the surface treatment processes on as-receive Al results in more isotropic roughness.
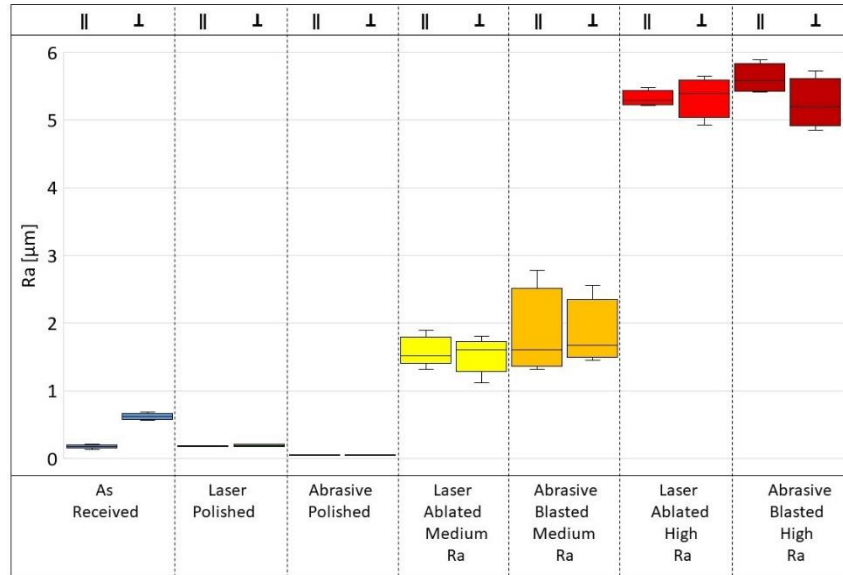

Figure 5.7. a) Ra measurements for different Al surface treatments (∥: rolling direction, ⊥: orthogonal to the rolling direction).

Figure 5.8 shows the microscopic image and the corresponding EDX analysis of the as-received surface. The rolling lines which provide surface roughness are visible and the presence of carbon on the as-received Al is due to inevitable surface contamination.
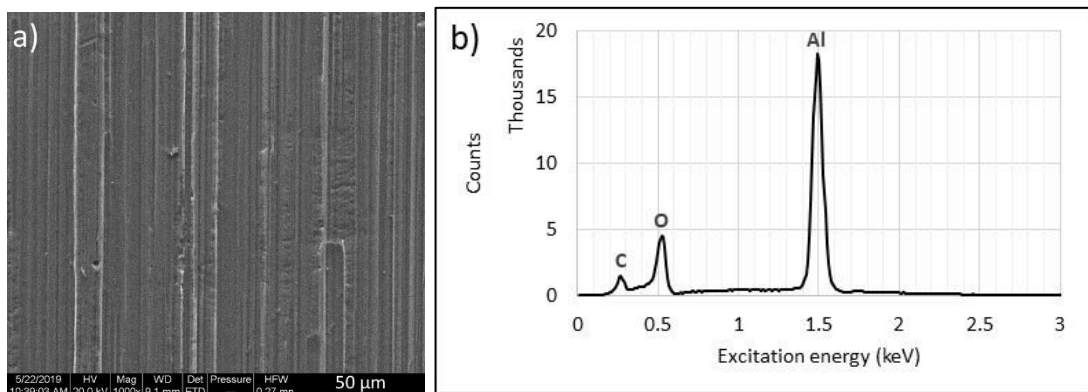

Figure 5.8. a) SEM image of the as-received surface and b) the corresponding EDX analysis.

Having a closer look at the surface of as-received Al is necessary to identify the structure of natural Al oxide which makes intimate contact with PA during the laser joining process. Figure 5.9 shows the TEM results of cross-sectional observation for as-received Al.
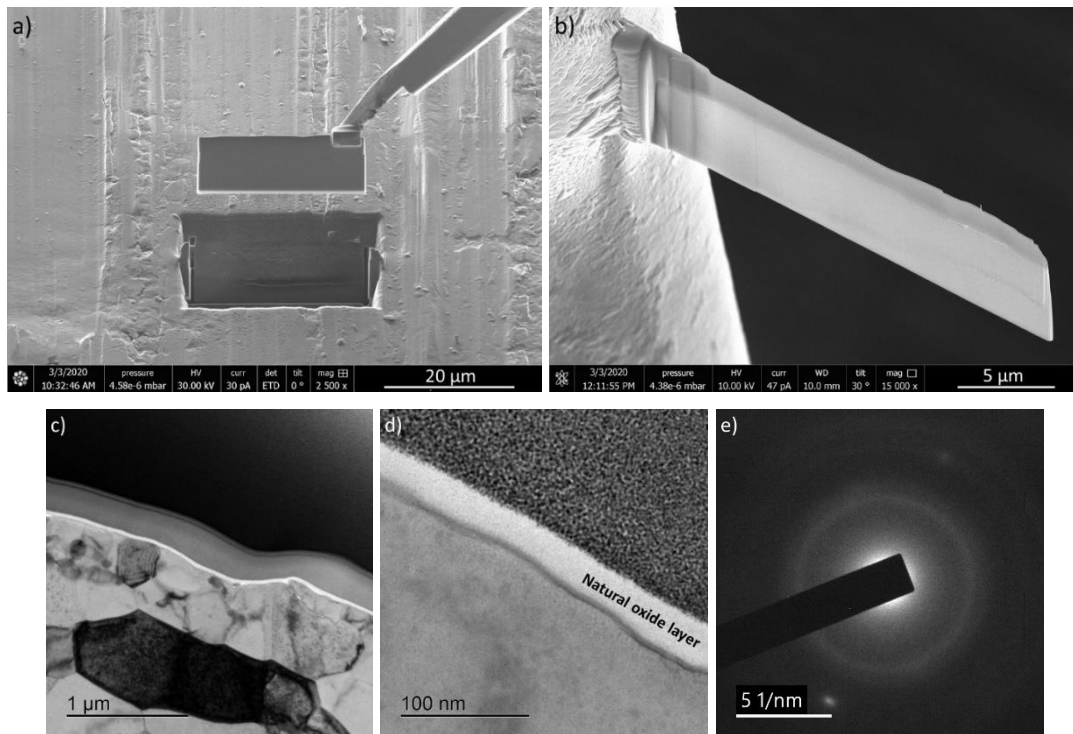
Figure 5.9. a, b) FIB cut for as-received Al sample, c, d) TEM images, and e) diffraction pattern for natural Al oxide.

Natural Al oxide with approximately 25 nm thickness covers the as-received Al surface. The oxide layer is relatively dense and uniform following the surface roughness of Al. This layer is amorphous in contrast to the Al.

Figure 5.10 depicts the SEM images of the laser-polished sample under ambient conditions with the EDX analysis. Compared to the as-received surface, the oxygen content of the EDX analysis is considerably higher, and a nanostructured layer is visible on the Al surface. Figure 5.11 shows the TEM results of cross-sectional observation for laser-polished Al. In combination with XPS results (see figure 5.12), an artificial Al oxide layer is created on the Al surface after laser polishing under ambient conditions. The nanostructured artificial oxide layer is considerably porous compared to the natural oxide layer and the thickness is approximately 1.5 µm. Having in mind the results of roughness measurement, the measurements were not sensitive enough to identify the nanostructured layer due to the relatively big size of the stylus tip radius.
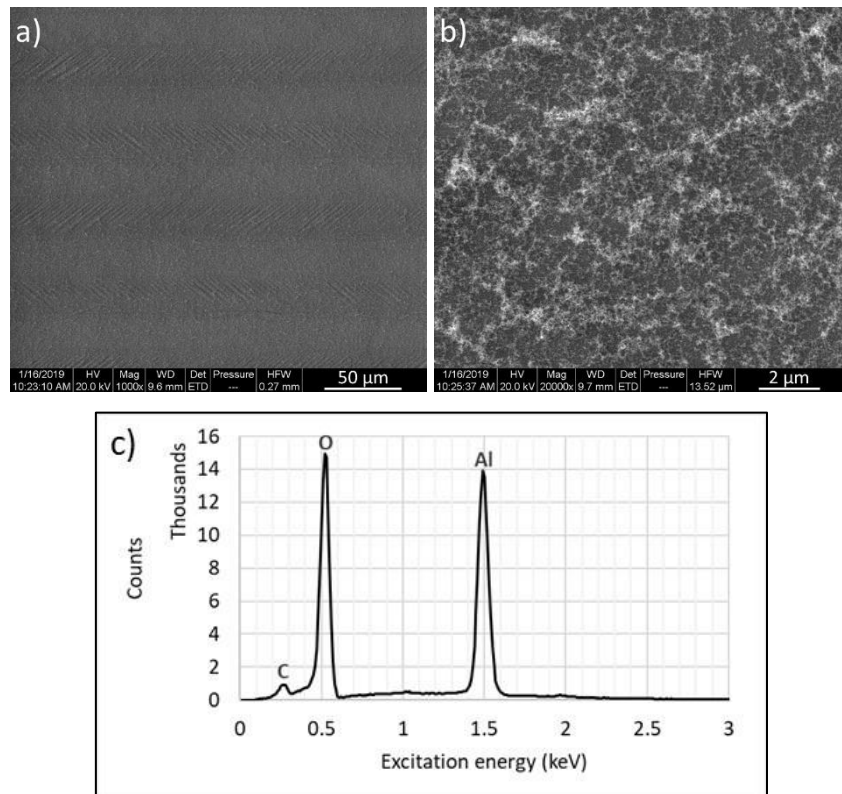
Figure 5.10. a, b) SEM images of the laser-polished surface under ambient conditions, and c) the corresponding EDX analysis.
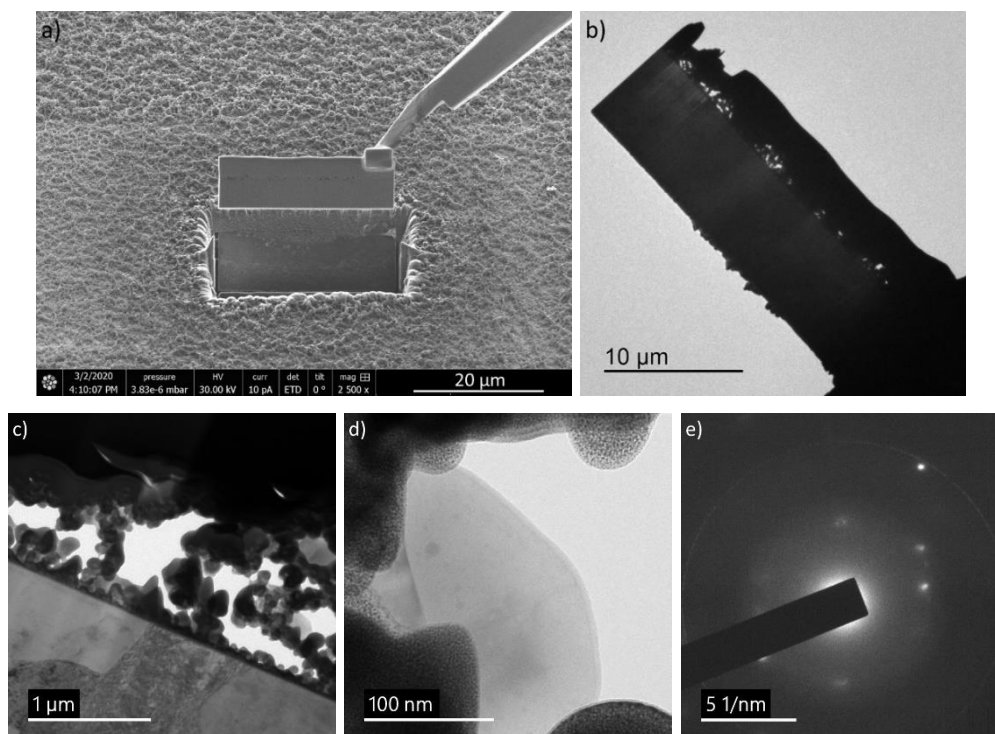

Figure 5.11. a, b) FIB cut for laser-polished Al sample, c, d) TEM images, and e) diffraction pattern for artificial Al oxide.

TEM diffraction of the artificial oxide layer shows distinct spots in the image; therefore, this layer is crystalline. It should be noted that due to the high porosity of the layer, it is well

decorated with Pt particles although a layer of amorphous carbon was already deposited before Pt coating. Both EDX and XPS results confirm the cleaning effect of the laser polishing process with the reduction of carbon content.
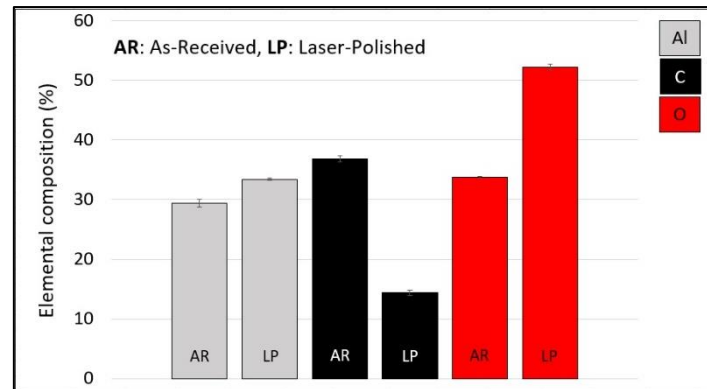
Figure 5.12. Elemental composition of Al samples surfaces from XPS.

Figure 5.13 depicts the SEM images of the laser-polished samples under the Ar atmosphere. In contrast to the laser-polished samples under ambient conditions, the development of artificial oxide is considerably suppressed here. The EDX analysis of the artificial oxide particles is comparable to that shown in figure 5.10, while the EDX analysis of the Al matrix is similar to figure 5.8 with less carbon content because of the cleaning effect of the laser polishing process.
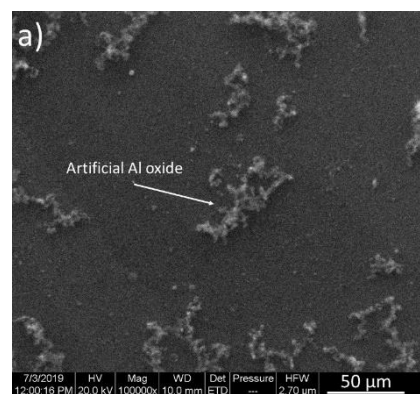
Figure 5.13. SEM image of the laser-polished surface under Ar atmosphere.

Figure 5.14 shows the SEM images of the laser-ablated samples to achieve medium and high levels of roughness. The EDX analysis of the laser-ablated samples (data not shown) shows a higher level of oxygen contents compared to the as-received condition, which is an indication of the presence of an artificial oxide layer. The surface chemistry of the laser-ablated high Ra samples is less uniform compared to the corresponding medium Ra samples. It is due to different process parameters especially lower pulse frequency and feed rate.
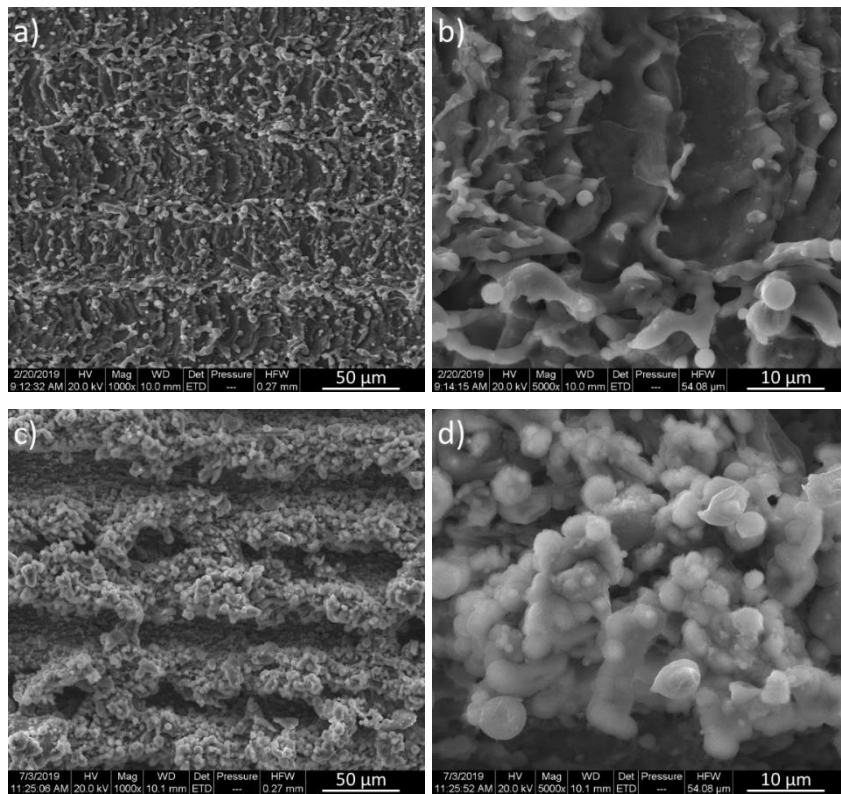
Figure 5.14. SEM images of laser-ablated surfaces, a, b) medium roughness, and c, d) high roughness.

Figure 5.15. SEM images of abrasive-blasted surfaces, a, b) medium roughness, and c, d) high roughness.

Figure 5.15 depicts the SEM images of abrasive-blasted samples with two levels of surface roughness. Each category is comparable to a corresponding laser-ablated one regarding surface roughness values; however, the EDX analysis (data not shown) is comparable to the as-received condition. The natural Al oxide is present on abrasive-blasted surfaces with higher surface roughness compared to the as-received condition.

5.2.3. Tensile-shear load of the joints

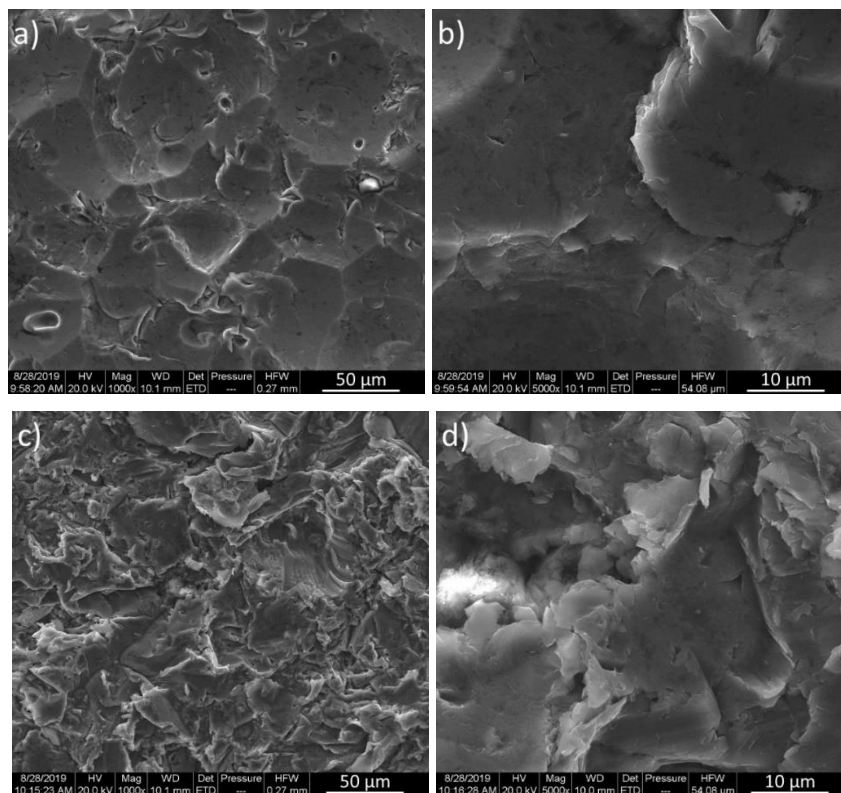Figure 5.16 shows shear load values for different pretreated Al samples laser-joined to PA. As the joining parameters are identical for the samples, it is tried to link the shear loads of the joint to the surface condition of Al samples. The as-received samples with the mean shear load of approximately 1018 N are the reference. In this case, the welding path is parallel to the rolling direction of Al samples. By changing the Al samples orientation, (the welding path is perpendicular to the rolling direction) the shear loads of the joints are comparable to the previous setup (approximately 1014 N on average). It is the first indication that mechanical interlocking is not the dominant bonding mechanism between Al and PA in the laser joining process.

By making the Al surface rough with the presence of the natural oxide layer, a huge drop in the shear loads of the joint can be observed. In the extreme case, which is abrasive-blasted high Ra, there is practically no durable joint. Laser joining these samples even with higher modulated power (up to 300 W) does not improve the shear load of the joints.

For laser-ablated samples, the shear loads were improved compared to the corresponding blasted category. Therefore, to increase the shear load of the joints, the development of an artificial oxide layer is significantly more effective rather than an increase in surface roughness. In fact, for the high Ra values of both categories, the shear load is lower than that of medium Ra due to higher thermal contact resistance. Higher Ra values bring higher thermal contact resistance; therefore, heat flow from Al to PA will be less uniform to create a reliable joint. However, for laser-ablated medium Ra samples, there is a significant improvement in shear load compared to the as-received condition.
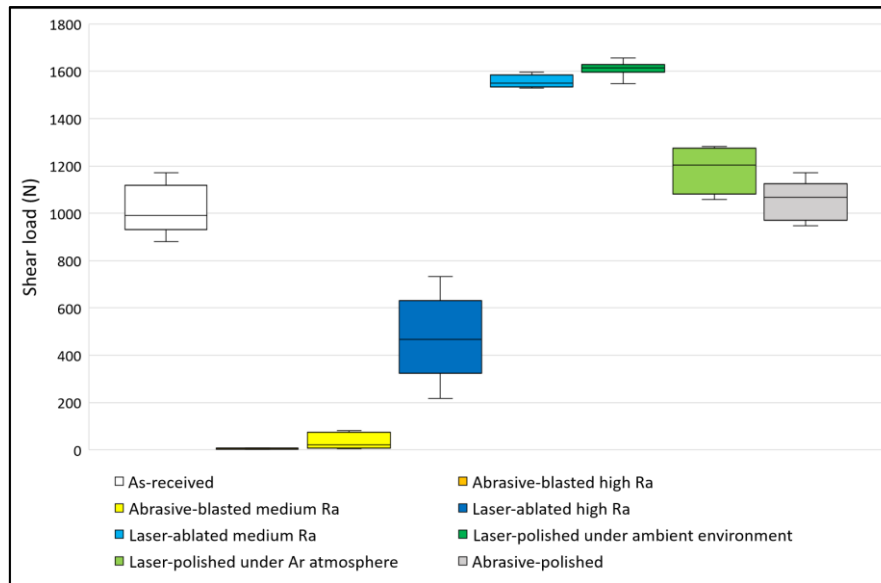
Figure 5.16. Tensile-shear load of the assemblies with different Al surface pre-treatments.

By making a comparison between the shear loads of the samples with low Ra values (laser-polished and abrasive-polished), the importance of the artificial oxide layer will be better clarified. The density of the artificial oxide layer is under the control of the laser-polishing environment. Under the Ar environment, the creation of nanostructured oxide is significantly suppressed, and the improvement of the shear load is not considerable. Moreover, the shear load of abrasive-polished samples is comparable to that of the as-received sample. It indicates that the slight reduction of surface roughness (consequently lower thermal contact resistance) with the presence of natural Al oxide is not effective to increase the shear loads of the joints. The natural Al oxide is dense and does not provide infiltration sites for molten PA during the joining process. However, for the sample laser-polished under the ambient conditions, the highest shear load is achieved thanks to the presence of a relatively thick artificial Al oxide layer, which can provide infiltration sited for the molten PA. this hypothesis will be discussed in detail in section 5.2.6. Overall, laser polishing of Al under ambient conditions provides 58% improvement in shear load compared to the as-received condition.

5.2.4. Fracture surface analysis for different Al surface treatments

Figure 5.17 shows the Al fracture surfaces for different pretreatment processes in a tilted view under ESEM. The PA residue on the Al surface (dark stripes/spots) represents the joint area between the materials. By making a comparison between figures 5.16 and 5.17, the morphology of PA residue on the Al surface after the mechanical failure can be explained by the corresponding mechanical properties. The PA residue on the as-received Al surface is not uniform as the natural Al oxide cannot prove good wettability and thus adhesion for molten

PA. Therefore, a mixed adhesive/cohesive failure is observed for as-received samples. Increasing the surface roughness with the presence of natural Al oxide makes the PA residue significantly narrow due to higher thermal contact resistance. By creating an artificial Al oxide layer, the PA residue is significantly wide and thicker even though the thermal contact resistance is supposed to be similar to the corresponding abrasive-blasted samples. It is an indication that the artificial Al oxide layer can promote adhesion to PA.
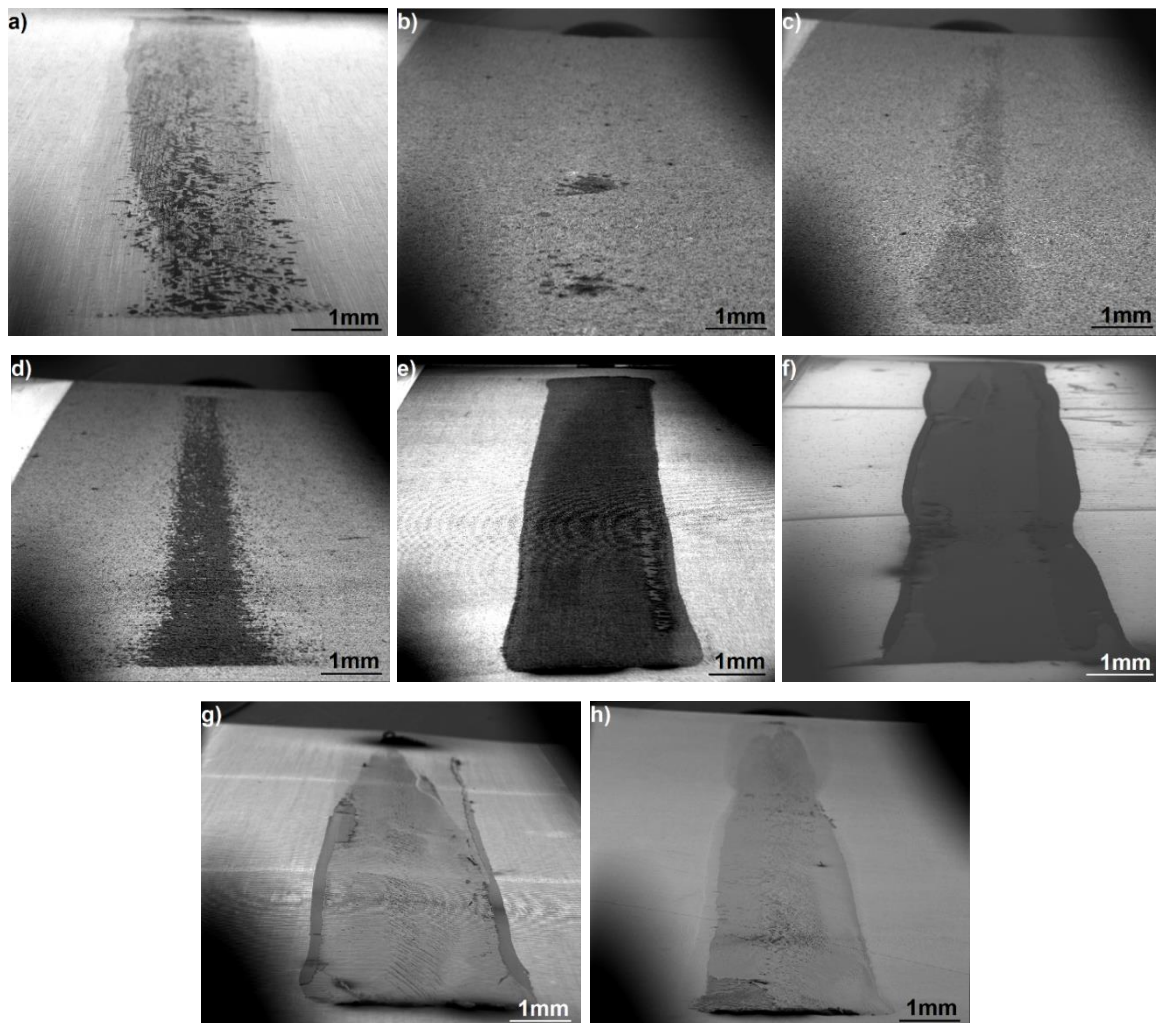
Figure 5.17. Al fracture surfaces, a) as-received, b) abrasive-blasted high Ra, c) abrasive-blasted medium Ra, d) laser-ablated high Ra, e) laser-ablated medium Ra, f) laser-polished under ambient conditions, g) laser-polished under Ar atmosphere, h) abrasive-polished.

In the case of the low roughness of abrasive-polished samples, low contact resistance provides a better heat flow from Al to PA, therefore resulting in wider PA residue. However, the intimate contact between molten PA and natural Al oxide is limited to the extreme surface of oxide therefore, the anchoring effect is weak and as seen before, the shear load is comparable to the as-received sample. This is also plausible for the laser-polished sample under Ar environment

except for the creation of rare and separate artificial oxide particles. Due to the lack of anchoring effect, the failure happens near the interface of Al/PA in the PA.

For laser-polished samples under ambient conditions, a wide and relatively thick PA residue on the Al has been observed thanks to the artificial Al oxide layer. Therefore, in contrast to the samples with natural Al oxide, high anchoring is present, which results in a superior shear load between the samples.

5.2.6. Failure mechanisms

Among the different samples discussed in the previous section, laser polishing and laser ablation processes were more promising to improve the mechanical performance of the assembly. Therefore, further investigations on the failure mechanisms of these samples are done.

Figure 5.18 shows a cross-section schematic and microscopic image of laser-polished Al joined to PA. As already discussed, PA melts during the laser joining process, and by infiltration into the nanostructure wets the Al surface effectively. For laser ablation medium Ra, a similar process happens; however, due to the higher surface roughness of Al, the mechanical interlocking is expected to be more pronounced.
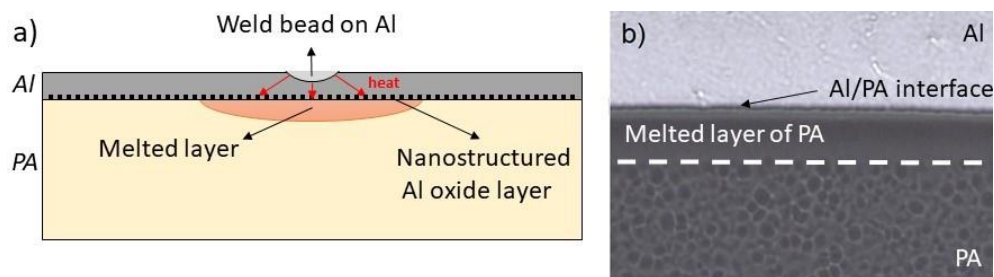
Figure 5.18. a) Schematic of a cross-section and b) microscopic observation of cross-section for laser joining of laser-polished Al to PA.

The size of the melted PA is measured for different cross-sections prepared from laser-joined assemblies while the modulated power changes from 200 to 340 W. The measurements are done for as-received, laser-ablated (medium Ra) and laser-polished (ambient conditions) Al samples laser-joined to PA. Figure 5.19 shows the measurements of width for the PA melted layer based on microscopic cross-sectional observations. The measured values represent very good accordance with the width of PA residue on top of the Al fracture surface for the corresponding sample. Figure 5.20 shows the visual appearance of the Al fracture surfaces with different surface treatments.

As already discussed, the thick, porous artificial oxide layer of laser-polished Al provides perfect wetting for molten PA. Therefore, generally for each modulated power, the laser-polished surface provides the highest width for the melted PA while the as-received surface represents the lowest one.

The maximum depth of PA melting occurs in the middle of the joining area, and it increases from approximately 12 to 45 μm for 200 to 340 W of modulated power which is almost comparable for all the mentioned Al surface conditions. Consequently, the thickness of melted PA is mostly under the effect of the laser joining power.
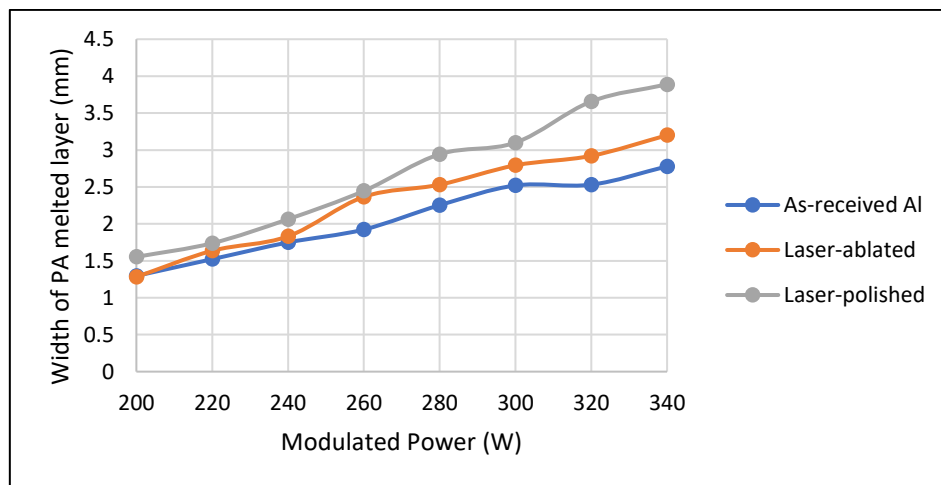
Figure 5.19. Width of PA melted layer based on microscopic observation of the cross-sections.
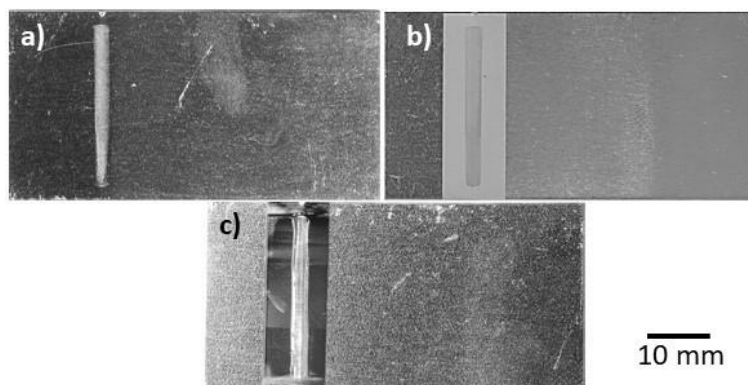
Figure 5.20. The visual appearance of Al fracture surfaces, a) as-received, b) laser-ablated, and c) laser-polished.

Figure 5.21 depicts the microscopic top view of the Al fracture surfaces for the mentioned surface conditions. As can be seen, the as-received Al surface provides a mixture of adhesive/cohesive failure while the laser polishing and ablation of Al result in completely cohesive failure with higher shear loads compared to the as-received state. Still, the mechanism of cohesive failure is not identical for them.
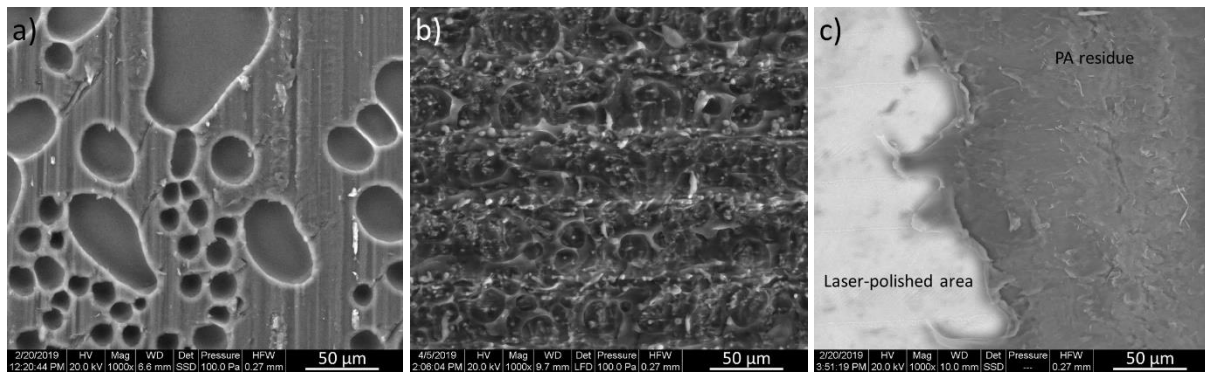
Figure 5.21. The microscopic view of PA residue over, a) as-received, b) laser-ablated, and c) laser-polished Al (260 W modulated power of laser joining).

Figure 5.22 shows the cross-section view followed by Al and PA fracture surfaces for laser-ablated Al joined to PA. The laser joining process is done with 260 W of modulated power. Although the PA effectively filled the surface roughness of Al, some bubbles are visible in the PA near the interface. It should be noted that with the current configuration of laser joining, the PA degradation happens at a minimum of 300 W modulated power (discussed in section 5.2.1); however, due to surface roughness of laser-ablated sample and uneven heat transfer from Al to PA, slight thermal pyrolysis of PA happens in the form of separated bubbles. The bubbles govern the failure of the assemblies and result in cohesive failure for laser-ablated Al samples joined to PA as they are visible in both Al and PA fracture surfaces (Figure 5.23c, d).
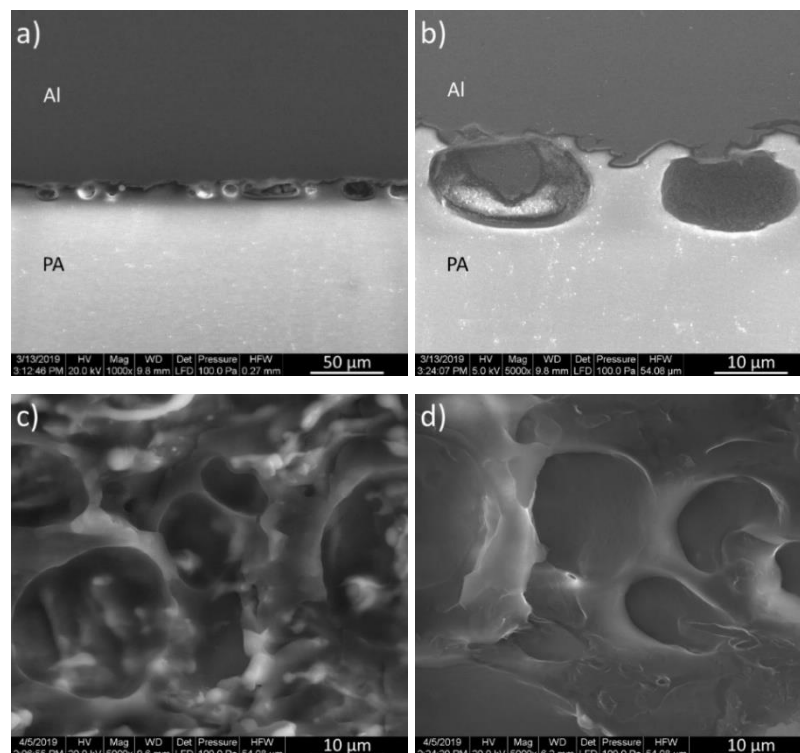
Figure 5.22. a, b) The cross-section of laser-ablated Al joined to PA, c) Al fracture surface, and d) PA fracture surface of the corresponding sample (260 W modulated power of laser joining).

For the laser-polished Al samples joined to PA with 260 W of modulated power, the discussed bubbles are absent due to low surface roughness and uniform heat transfer from Al to PA (see figure 5.23).
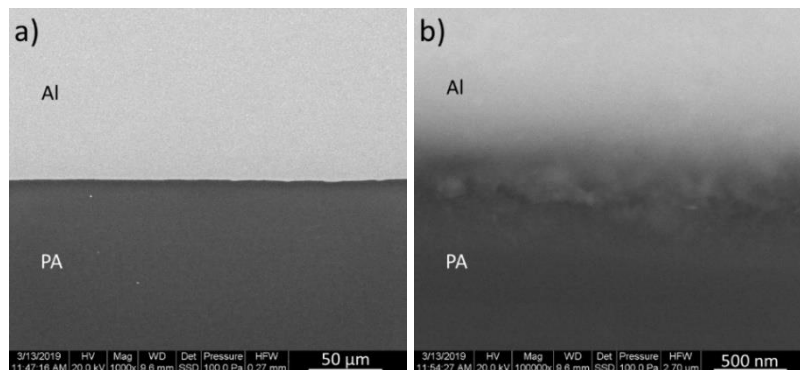
Figure 5.23. a, b) The cross-section of laser-polished Al joined to PA with 260 W modulated power.

Surface profilometry measurements on fracture surfaces show that the PA residue on top of the laser-polished Al surface has good accordance with the thickness of the PA melted layer which is measured from cross-section observation. Therefore, the failure happened between the melted PA layer and the bulk in the HAZ. Figure 5.24 depicts the comparison between cross-section observation and profilometry of a fracture surface for a laser-polished Al sample joined to PA with 260 W modulated power.
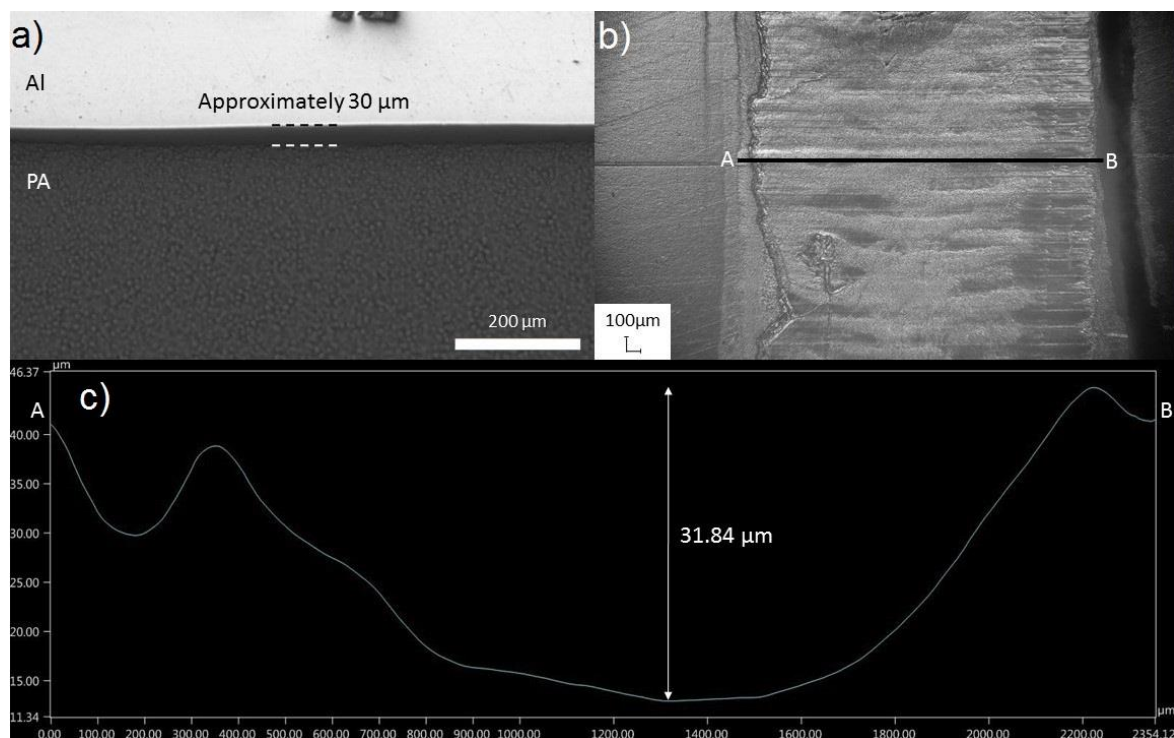
Figure 5.24. a) cross-section of laser-polished Al joined to PA with 260 W of modulated power, b) PA fracture surface of the corresponding sample and c) profilometry result of the selected area.

Schricker et al. [82] reported on the higher hardness of the HAZ due to the crystallization effect of amorphous areas for the PA66 laser-joined to Al compared to the bulk and melted zone. Therefore, HAZ is more susceptible to failure during the mechanical test.

Figure 5.25 shows the TEM observation for laser-polished Al under ambient conditions laser-joined to PA. The cross-section is prepared from an Al fracture surface.
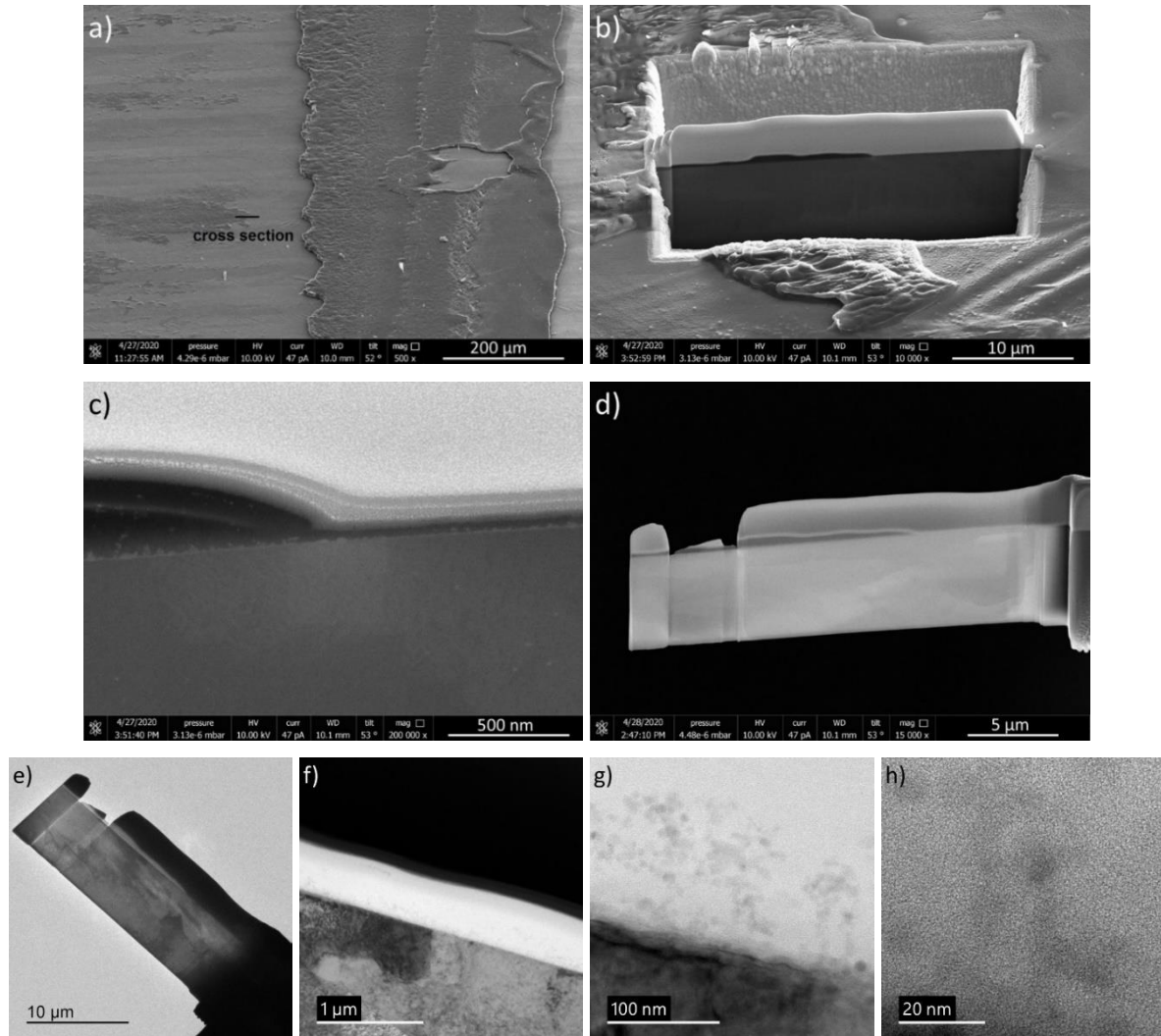
Figure 5.25. Al fracture surface a) the place where the cross-section is made, b) cross-section after Pt deposition and Ga ion beam milling, c) secondary electron image of cross-section, d) secondary electron image of TEM lamella after transfer to the copper grid, e) bright-field TEM image of the complete lamella, f) bright-field TEM image of dense bond between polished Al substrate and PA, g) bright-field image of individual Al_xO_y nanostructures embedded in PA, and h) high-resolution bright-field image of Al_xO_y nanostructures in amorphous PA.

An area where a thin layer of PA on top of the laser-polished Al was chosen for FIB preparation is depicted in figure 5.25a. Figure 5.25b shows the cross-section which was prepared using the Ga ion beam after Pt deposition. Secondary electron imaging using the FIB shows a dense bonding between the laser-polished Al substrate and the PA (see figures 5.25c and d). Bright-

field TEM imaging can visualize this bonding in higher resolution (see Figure 5.25e-h). Individual Al_xO_y nanostructures still bound on the Al substrate can be found in the PA matrix (see Figure 5.25f-h). High-resolution TEM bright field imaging cannot show any lattice fringes indicating that the PA matrix is amorphous. (see Figure 5.25h).

Therefore, the dense bonding of the PA matrix to the Al_xO_y nanostructures on top of the laser-polished Al substrate can be observed which is enabled by a perfect wetting of PA during the joining process. No bubbles or voids could be found at the cross-section both by secondary electron and by bright-field TEM imaging. This implies that for these samples, the physicochemical bonding is promoted rather than the mechanical interlocking. Due to the high surface area of the Al_xO_y nanostructures and the perfect wetting, the anchoring effect is promoted, and an extremely strong bond is formed, which results in a superior shear load during mechanical testing.

Figure 5.26 shows the µCT observations for as-received, laser-ablated, and laser-polished Al samples laser-joined to PA with 260 W modulated power.
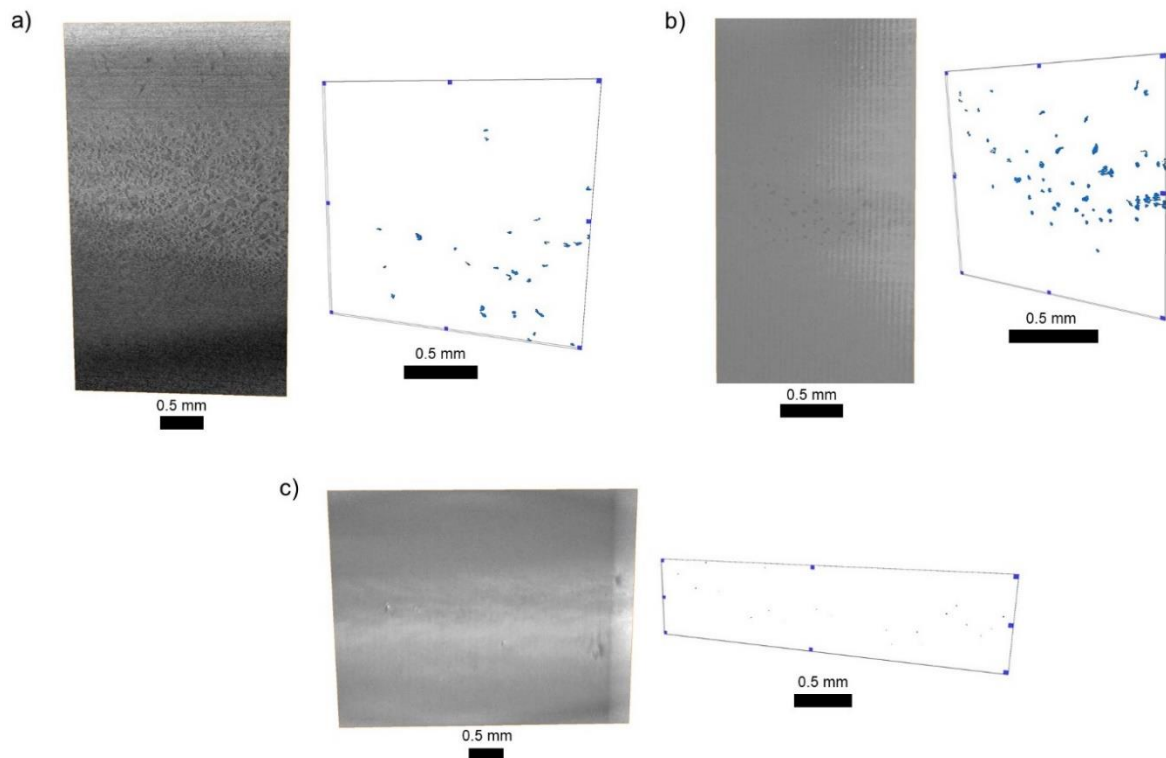

Figure 5.26. µCT analysis at the interface of Al/PA showing for each case a representative interfacial slice (left) and the volume rendering of the interfacial bubbles (right) in the case of, a) as-received Al, b) laser-ablated Al, and c) laser-polished Al.

Two pieces of information are provided: a representative 2D slice recorded in the interfacial region of Al/PA, and the 3D volume rendering of the bubbles extracted from the interfacial region after contrast thresholding. For the as-received Al, PA does not cover the Al at the interface of Al/PA uniformly as proved by the presence of discontinuities and bubbles (average equivalent diameter of 14.5 µm), which results in a mixed (adhesive/cohesive) failure. For laser-ablated Al, the presence of bubbles is confirmed (average equivalent diameter of 18.2 µm), while for laser-polished Al samples, the interface is quite continuous and contains smaller bubbles (average equivalent diameter of 4.8 µm) compared to the two other cases.

5.2.7. Interim summary II

As-received Al surface is covered with a natural oxide layer. The natural Al oxide is dense and 25 nm thick for the samples of this study. Therefore, the joining/bonding between Al and PA is limited to the extreme surfaces of the materials, and a mixture of adhesive/cohesive failure is observed. The promotion of the anchoring effect (mechanical or chemical) is necessary to increase the mechanical performance of the assembly. The results showed that the chemical anchoring effect of the nanostructured oxide layer is more promising. Nevertheless, different surface roughnesses of Al result in different mechanisms of failure. For laser-polished Al joined to PA, structural modification of PA during the joining process is responsible for failure.

5.3. PA structure

Following the failure mechanisms from the previous chapter, it is interesting to improve the mechanical properties of the joined specimens by modifying the PA structure near the Al/PA interface. To achieve this purpose, three different approaches are considered: laser treatment of PA samples, post-heat treatment of the laser-joined specimens, and laser joining with different feed rates.

5.3.1. Laser treatment of PA

The laser treatment of PA before the joining process was done with a CO_2 laser source as discussed in 4.2.2. The CO_2 laser was selected because of the good absorbance of the PA for the far-infrared wavelength of the laser. Figure 5.27 shows the surface roughness measurements and EDX analysis for as-received and laser-treated PA.
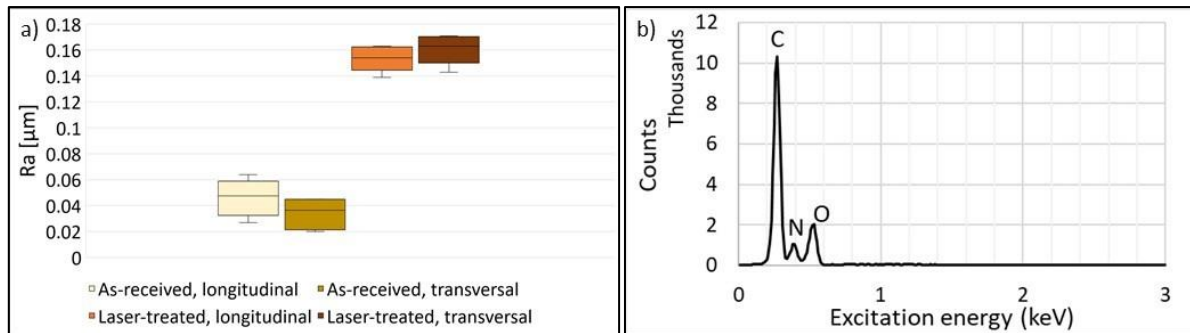
Figure 5.27. a) Ra measurements for PA samples and b) EDX analysis of as-received and laser-treated PA.

A slight increase in surface roughness can be observed due to the laser treatment process of PA while no significant chemical modification is observed (see figure 5.27b).

Figure 5.28 shows the XPS analysis of PA samples in as-received and laser-treated conditions. A slight oxidation effect of PA after the laser treatment process is detected. More precisely, a very slight increase in the oxygen concentration is observed, together with a slight decrease in the nitrogen concentration. High-resolution spectra of oxygen show that more C-O bonds are observed compared to C=O for laser-treated samples (not shown here). It is assumed that these new C-O bonds are coming from the degradation of pristine PA molecules after laser treatment. Therefore, laser treatment has a limited effect on the surface chemistry of PA; yet a stronger effect on the PA structure in the first microns in depth is expected.
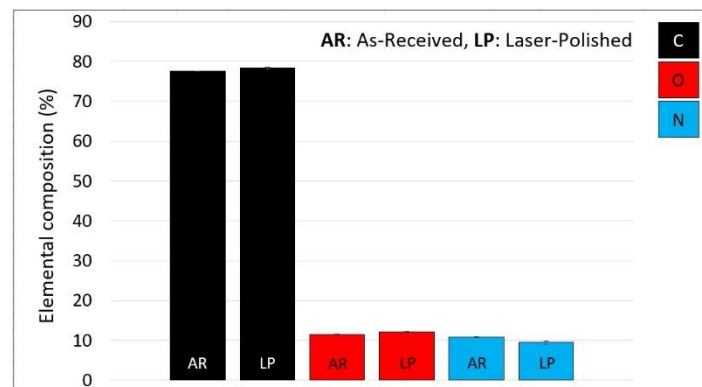
Figure 5.28. Elemental composition of PA samples' surfaces from XPS.

Figure 5.29 shows the gXRD diffractograms of PA samples in grazing mode. PA is well-known as a semi-crystalline polymer. gXRD measurements conducted with a penetration depth of 35 µm before and after laser treatment on the PA surface show that the total crystallinity of PA slightly increases from 58.5 wt. % to 63.9 wt. %. The crystalline phase consists of the α phase (monoclinic) and the γ crystalline phase (monoclinic or pseudohexagonal). Although the total crystallinity has been increased by the laser treatment, the increase is associated with the γ

phase (from 8.3 wt. % to 23.4 wt. %) and the ratio of α to γ phase reduced (from 85.8 wt. % to 63.4 wt. %).

α phase crystallinity (wt. %)	50.2		α phase crystallinity (wt. %)	40.5
γ phase crystallinity (wt. %)	8.3		γ phase crystallinity (wt. %)	23.4
Total crystallinity (wt. %)	58.5		Total crystallinity (wt. %)	63.9
α/γ ratio (%)	85.8		α/γ ratio (%)	63.4
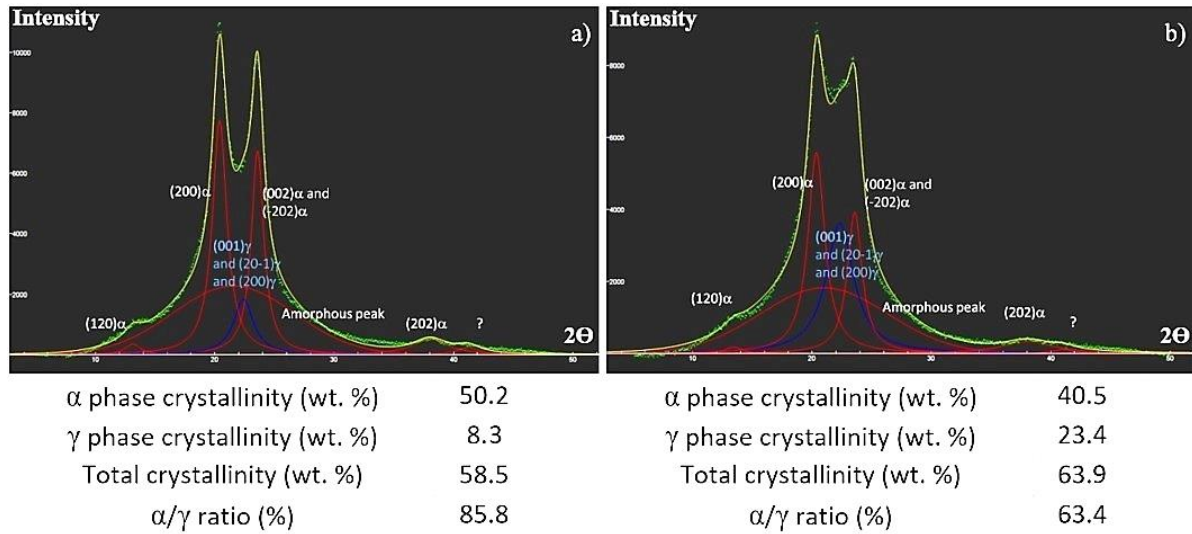
Figure 5.29. XRD of the PA samples a) as-received condition, b) laser-treated condition.

Moreover, nano scratch indentations show the laser-treated area is softer than the as-received area (hardness of 175 MPa and 213 MPa, respectively). Both the slight increase in PA surface roughness and the decrease in hardness after the laser treatment process is certainly related to the evolution of the crystalline properties of PA to some extent. Indeed, as shown by gXRD, the laser treatment induced an increase in the γ phase fraction compared to the α phase. Since α phase is more stable and perfect (more packed) than γ phase [92], the laser treatment may slightly decrease the local packing of the crystalline phase explaining a local increase in roughness (local dilatation) and a local decrease of hardness (gamma phase expected to be less hard than alpha phase). This assumption is possible considering that this phase transition has more impact on roughness and hardness than the slight increase of the overall crystallinity (having the opposite influence). Other mechanisms are probably contributing to this increase in roughness and decrease in hardness.

Figure 5.30 depicts the AFM imaging of the PA surface. For the as-received surface condition, no clear evidence of the crystalline structure is observed whereas a spherulitic structure is noted in the laser-treated area, as observed in figure 5.30a. For the latter image, in addition to applying a thermal treatment of the PA inducing crystalline changes in the volume of interaction, the laser can also finely etch the extreme surface of the polymer revealing its intrinsic morphology. In principle, to reveal semi-crystalline morphology, the amorphous phase must be removed, creating a local topography since crystalline lamellae are still present. This mechanism may

explain the increase of roughness, not only due to crystalline phase changes but also to this potential elimination of the amorphous phase at the extreme surface. Cryo-ultramicrotomy preparation is a convenient method to both get rid of the PA "skin", thereby removing the first tens of nanometers of the surface and obtaining a very flat surface which is convenient for AFM nanomechanical analysis.
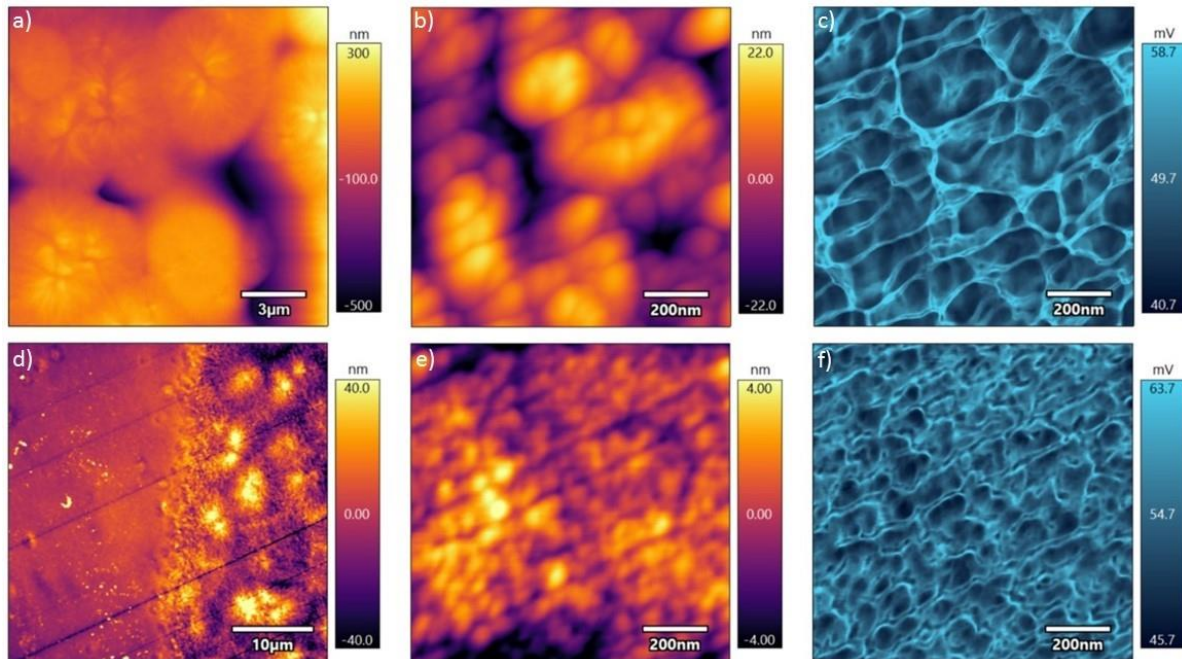
Figure 5.30. AFM results of PA surfaces, a) laser-treated area on the bulk sample, no cryo-microtomy, topography, b) laser-treated area after cryo-microtomy, topography, c) laser-treated area after microtomy, dissipation, d) general view of both areas after microtomy: left untreated, right laser-treated, e) untreated area after microtomy, topography, and f) untreated area after microtomy, dissipation.

An overview of both areas (laser-treated and as-received) after cryo-microtomy is observed in figure 5.30d. At low magnification, no evidence of the crystalline structure is visible in the untreated area, whereas the particular spherulitic structure is observed in the laser-treated area. Higher magnification is performed on the two areas, to investigate their nanostructure. A very fine structure with a typical dimension in the range of 50-100 nm, is observed for the untreated area (figures 5.30e and 5.30f), whereas another structure of greater dimensions (100-200 nm) is observed for the laser-treated area (figures 5.30b and 5.30c). Both are assigned to the crystalline structure of the PA. Note that hardness measurement being a volume analysis, cannot depict this elimination of the amorphous phase at the extreme surface.

Figure 5.31 depicts cross-section images for the laser-polished Al samples joined to as-received and laser-treated PA. The depth of the laser-treated PA is approximately 50 μm while the thickness of the melted layer is approximately 30 μm.

Figure 5.31. Cross-section schematics and OM images, a) laser-polished Al joined to as-received PA, b) laser-polished Al joined to laser-treated PA.

Figure 5.32 shows the force-displacement curves for the joined specimens with different surface treatments and the appearance of laser-polished Al joined to laser-treated PA after the shear test. Compared to this sample, others represent relatively br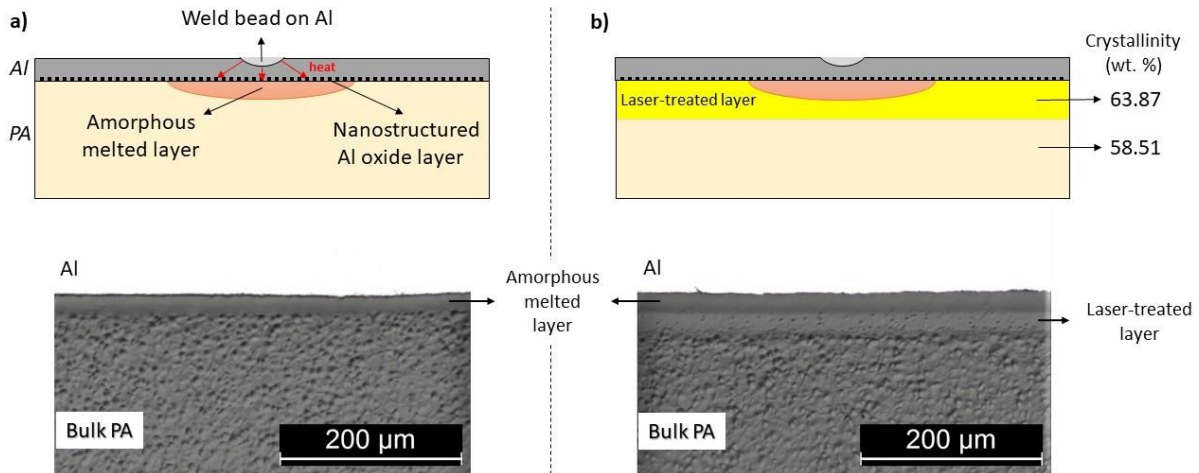ittle failures. The mechanisms of failure are already discussed in section 5.2.6. In addition, it is interesting to observe that the laser treatment of PA does not significantly improve the shear load of the laser-ablated Al joined to PA as the failure is still under the control of bubbles.

The laser treatment process improves the crystallinity of PA on the near-surface area. Therefore, HAZ is located in a more packed structure with higher mechanical properties in the case of laser-polished Al and laser-treated PA assembly, and it will improve the mechanical properties of the joints. Consequently, this modification of crystallinity probably prevents or delays the failure within PA and triggers the failure of Al in a ductile shear manner (the angle between the direction of failure and applying load is 45°). From another perspective, HAZ possesses higher hardness compared to bulk PA due to the crystallization effect [82]. The Laser-treated area of PA is more crystalline and thus harder compared to the bulk. Therefore, the hardness of HAZ and laser-treated areas are more similar compared to the bulk PA. A smooth transition of hardness between the HAZ and laser-treated area compared to HAZ and the bulk PA reduce stress concentration in the HAZ and hence shifts the failure to the Al.

It should also be noted that the surface melting of PA during the laser treatment process would refine the low molecular weight component and avoid the formation of weak boundary layers which might have a negligible effect in this case.
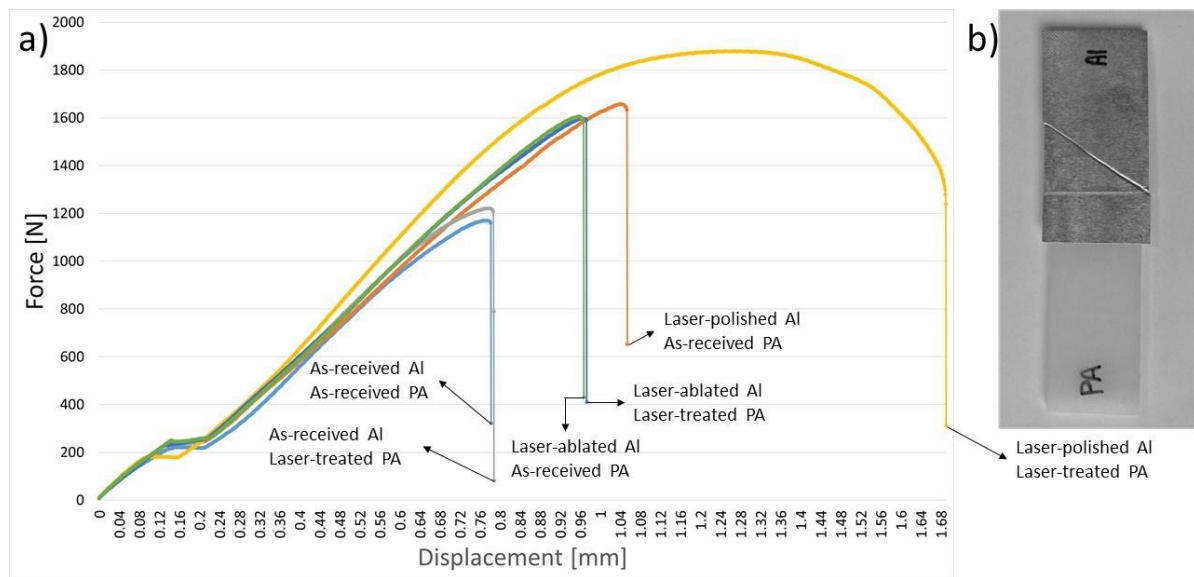
Figure 5.32. Force-displacement graphs for different samples and b) the failure appearance of laser-polished Al joined to laser-treated PA.

In the end, it is important to know if the laser treatment of PA applies a permanent effect on the material or is similar to some processes like plasma treatment, it suffers from hydrophobic recovery and an increase of Water Contact Angle[43] over time [93]. Figure 5.33 shows the water contact angle measurements for as-received PA and laser-treated PA naturally aged at different times. Due to the structural modification of the PA surface, there is an increase in the WCA which is preserved over time therefore, in contrast to plasma treatment, the laser-treatment process of PA does not suffer from hydrophobic recovery due to aging.
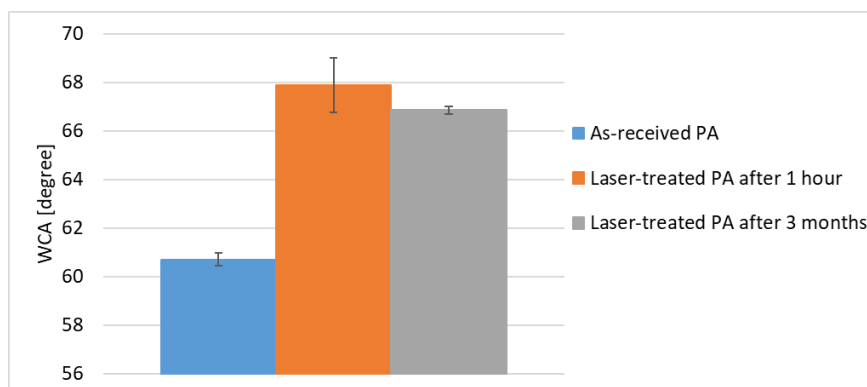
Figure 5.33. WCA of as-received PA, laser-treated PA after 1 hour, and laser-treated PA after 3 months.

Figure 5.34 depicts the sessile drop test images of the laser-polished Al sample. The presence of the nanostructure layer brings the ultrahydrophobicity and lotus effect[44] to the surface of

---

[43] WCA

[44] The lotus effect is the self-cleaning characteristic resulted by the ultrahydrophobicity of materials such as the leaves of Nelumbo or the lotus flower. Due to the micro and nanostructures of the surface, the droplets' adhesion to the surface of the substrate is minimized [97].

laser-polished Al (WCA is approximately 138°). Nevertheless, after some seconds and forcing the droplet to deposit on the surface, it eventually meets an imperfection and hence is adsorbed by Al via the nanostructure (WCA is approximately 70°). A similar case is assumed to happen in the case of laser joining due to clamping force.
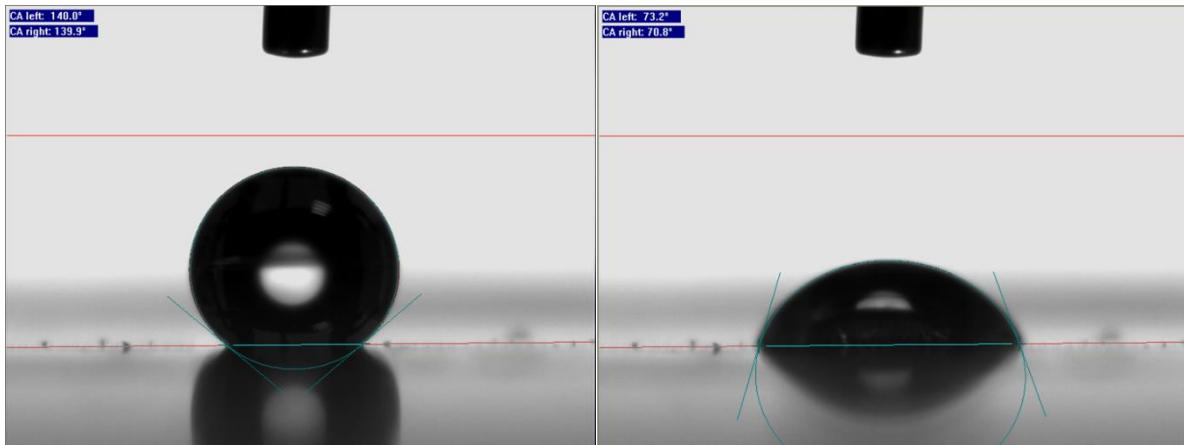
Figure 5.34. Sessile drop test of laser-polished Al left) drop test after 0.5 s, right) after 20 s and forcing deposition.

5.3.2. Post-heat treatment of the laser-joined specimens

The second approach is the heat treatment of the laser-joined assemblies to modify the amorphous structure of the melted PA layer. Figure 5.35 shows the shear loads of the laser-polished Al samples joined to as-received PA with different modulated powers. The positive effect of post-heat treatment is observed thanks to the continuous and uniform joint with the high anchoring effect provided by the artificial oxide layer. However, getting near to the melting point of PA, at 200°C there is a significant drop in the mechanical properties of the joint due to the high thermal stress of PA. The deformation of PA samples in the oven is noticeable. The reduction of the shear load also happens for the samples joined with 200 W-modulated energy at 150℃ as the joint between Al and PA has the minimum width. For other samples, there is a significant improvement in the shear load of the joints. For 240 and 280 W samples heat-treated at 50, 100, and 150℃ the joint is stronger than the base materials near the joint area. Therefore, the shear loads of the mentioned samples are comparable as the location of the failure is not the joint anymore. In conclusion, the implementation of heat treatment on the joined samples is only effective for laser-polished samples, which are joined with appropriate modulated power.
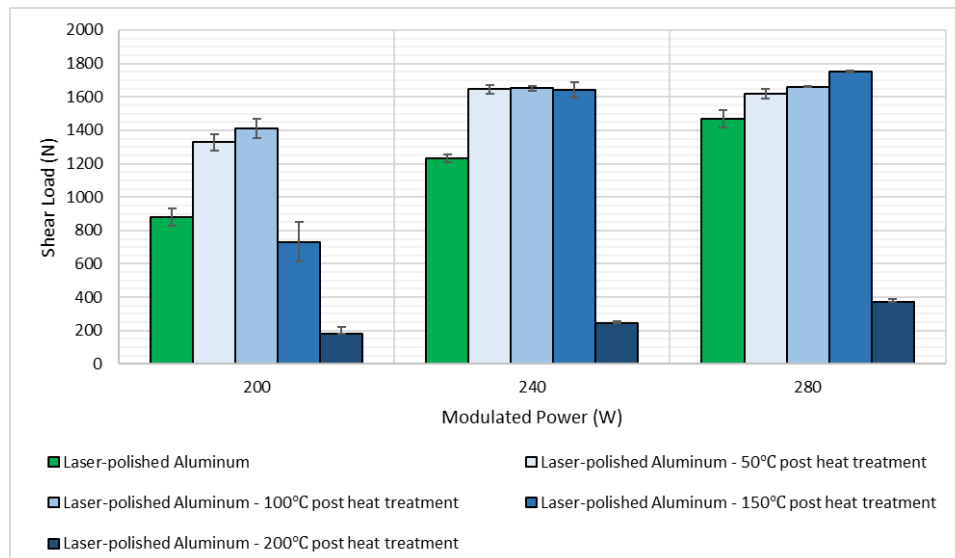
Figure 5.35. shear load of the post-heat-treated samples in case of laser-polished Al joined to as-received PA.

Nevertheless, all heat treatment cycles are detrimental to the mechanical properties of the joints in the untreated condition (see figure 5.36). In some cases, the joint already broke during the heat treatment process. There is a significant difference in thermal expansion between Al and PA (21-24 and 80 [10-6/K] respectively) [94], [95]. As the connection between Al and PA is merely limited to the extreme surfaces and is not also uniform, thermal stress eliminates the weakly bonded areas then the separated droplets will break due to stress concentration. This makes the connection even weaker and at higher temperatures, the joint breaks eventually during the heat treatment process. Figure 5.37 shows a tilted view of an as-received Al fracture surface.
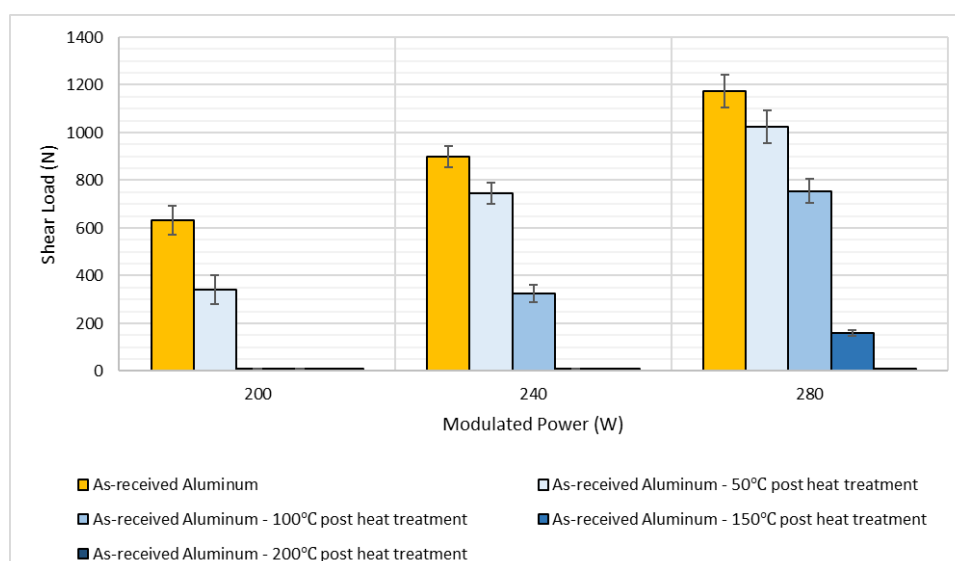
Figure 5.36. shear load of the post-heat-treated samples in case of as-received Al joined to as-received PA.
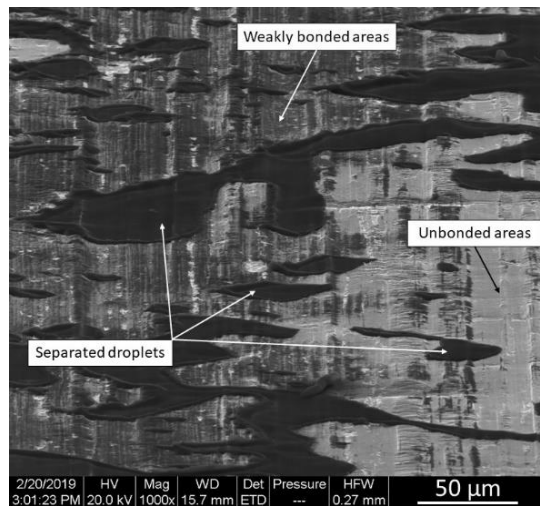
Figure 5.37. Tilted view of an as-received Al fracture surface without the heat treatment process.

5.3.3. Laser joining with different feed rates

The last approach to improve the mechanical performance of the laser-joined Al/PA assembly is to examine different feed rates for the joining process. The previous processes of PA surface treatment and post-heat treatment of the assembly are interesting in the case of the joining speed, minimizing the heat input, and thus HAZ are decisive. However, by sacrificing the joining speed and therefore, providing a lower cooling rate for the molten PA during the laser joining process, the creation of an amorphous structure is limited. With the development of a semicrystalline structure, the mechanical properties of the melted layer are improved which enhances the mechanical performance of the whole assembly. Figure 5.38 shows the microscopic images of cross-sections prepared with different feed rates.
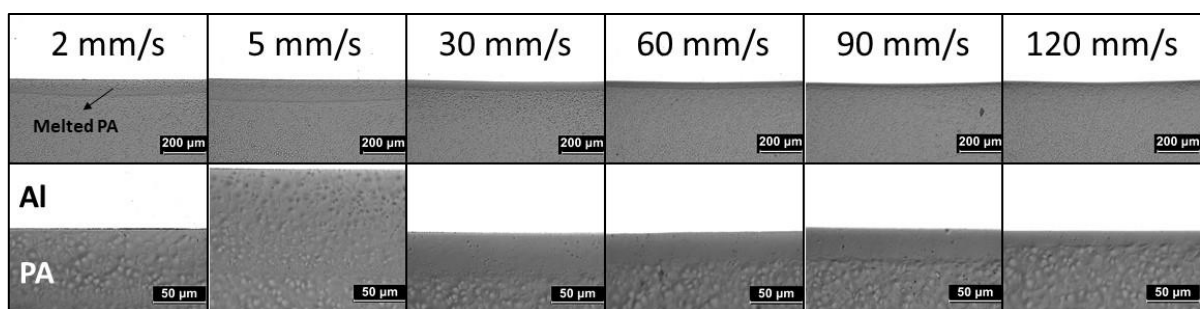
Figure 5.38. Cross-section of the assemblies for different feed rates.

Table 5.1 shows the thickness of the PA melted layer for different feed rates of joining. Generally, by increasing the feed rate the volume of the melted PA layer is decreased, and therefore, the combination of a higher feed rate and lower volume of molten material results in a higher cooling rate of the PA melted layer. As discussed before, for a high feed rate of 112.45 mm/s the melted PA layer is amorphous. On the contrary, laser joining with lower feed rates

provide a PA melted layer that is larger in volume and more similar to the structure of the bulk PA that is semicrystalline.

For laser joining with 2 mm/s, the thickness of the melted layer is lower than that of 5 mm/s and it does not follow the trend of other samples. To avoid PA degradation due to a very low feed rate and hence intense heat accumulation, the laser power should be kept very low. The high reflectivity of the Al surface in addition to the low power of laser joining results in the suppression of keyhole formation in a stable manner; therefore, the mode of welding is more on conduction welding rather than keyhole welding. Consequently, the thickness of the melted layer is reduced.

Table 5.1. The thickness of the PA melted layer for different feed rates

Feed rate [mm/s]	The thickness of the PA melted layer [µm]
2	76.8
5	103.7
30	38.9
60	29.7
90	17.8
120	11.4

Figure 5.39 depicts the shear strength of the samples prepared with different feed rates.
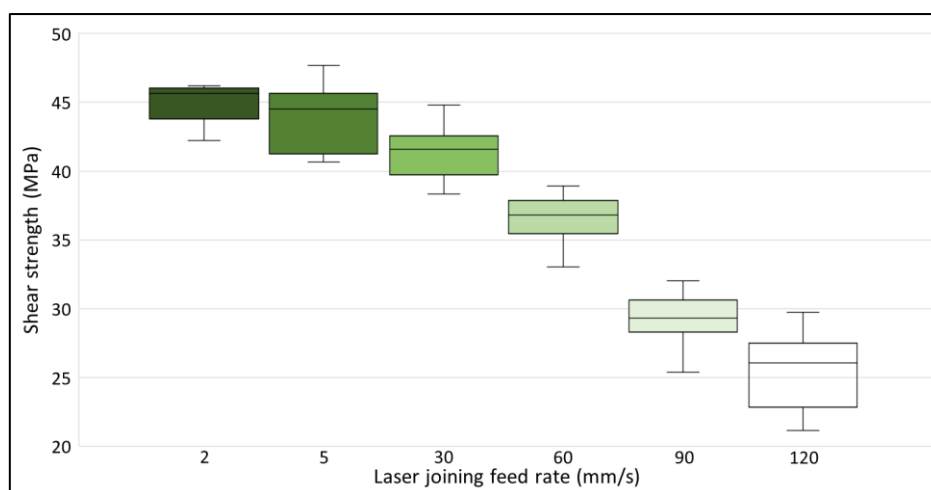
Figure 5.39. Shear strength of the samples laser-joined with different feed rates (Al samples are laser-polished).

As joining with lower feed rates results in significantly bigger joining areas, the shear load of the joint exceeds the capacity of the machine which is used in the study. Therefore, to make a

comparison between the samples laser-joined with different feed rates, it was tried to define a very short overlap between the materials and then implement the joining process.

As can be observed, by decreasing the feed rate and hence achieving a similar structure between the bulk and the melted PA, the shear strength of the assembly increases significantly. The shear strength of approximately 45 MPa achieved in this study is superior to the values reported by other researchers for similar material combinations. For example, 26 MPa for 6082 Al alloy laser-joined to PA6-GF66 [81], 12.5 MPa for friction press joining of 6082 Al alloy to PA6-GF30 [80], 41.8 MPa for 6061 Al alloy laser-joined to PA6-CF22 [58], 16.3 MPa for Al laser-joined to PA6 [50], and 39 MPa for Al-PA laser joining [96].

5.3.4. Interim summary III

The artificial Al oxide layer provides perfect wetting and adhesion for the molten PA. Consequently, cohesive failure happens and the structural modification of PA during the laser joining process is responsible for that in the absence of bubbles near the interface of metal/polymer. To reduce the effect of PA structural inhomogeneity, three processes of laser pre-treatment of PA, post-heat treatment of the assembly, and laser joining with different feed rates are proposed. In all cases, a superior assembly regarding the shear load is achieved thanks to the modification of the PA structure near the interface of metal/polymer.

5.4. Bonding mechanism

The materials which are used in the study are industrial grade Al and PA and the bonding is also created with a laser joining process under ambient conditions. Therefore, the effect of surface oxidation was considered, and the presence of contaminations and other elements related to the manufacturing processes are expected on the surfaces of materials. In the following, the results of different characterization techniques are discussed to identify the bonding mechanism between Al and PA.

5.4.1. STEM results

The cross-section of laser-polished Al joined to as-received PA was prepared by FIB and investigated by STEM dark-field imaging/EDX mapping that is presented in figure 5.40. The nanostructured Al_xO_y (white dots) on top of the Al substrate is completely wetted by PA, also indicated by the homogeneously distributed elements C and N surrounding Al and O visible in the elemental maps. Although there is no hint of a chemical change regarding the bondage of Al_xO_y to PA after joining, complete wetting of PA on top of the substrate indicates a strong physicochemical interaction between the nanostructured Al_xO_y and the PA. Together with the high surface area of nanostructured Al_xO_y, this leads to an exceptionally strong interconnection.
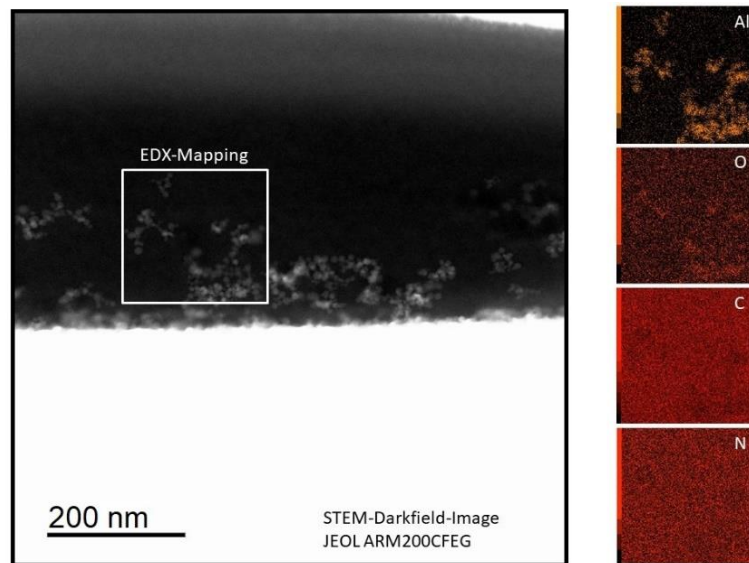
Figure 5.40. STEM dark-field image of the Al/PA cross-section and elemental maps of Al, O, C, and N of the selected area.

5.4.2.   XPS results

Table 5.2 depicts the elemental composition of different samples processed with XPS. For the analysis of samples, the followings are worth noticing:

- In the case of surface analysis of PA, silicon is detected which disappears after dissolution in trifluoroethanol. For PA ($C_{12}H_{22}N_2O_2$) C is 75%, N is 12.5%, and O is 12.5% however, due to the presence of Si on the surface of PA during the analysis, a higher O amount is detected (as SiO_x).

- Also, low amounts of Na, N, and Si are detected on the as-received Al surface, and they disappear after the laser polishing process (cleaning effect). However, after the laser polishing treatment, Zn and F are detected on the surface.

- The trifluoroethanol dissolution process is effective to remove extra PA from the fracture surface of Al and reach the near interface region. On the XPS analysis of the sample treated with trifluoroethanol, PA is still detected.

- After dissolution with trifluoroethanol, N is detected and is reduced by 1/3 only (compared to PA-ref) whereas the aluminum amount is 1/2 compared to the laser-polished sample.

Table 5.2. Elemental composition of different samples

Sample identifier	Al 2p%	C 1s%	N 1s%	O 1s%	Si 2p%
PA on laser-polished Al fracture surface (1)	0.8	72.8	8.9	14.6	2.9
PA on laser-polished Al fracture surface (2)	0.9	72.5	8.7	14.7	3.1
PA on as-received Al fracture surface (1)	1.7	71.4	8.6	15.5	2.9
PA on as-received Al fracture surface (2)	0.6	73.4	9	14.1	3
As-received Al (1)	24.6	32.8	0.4	40.2	2
As-received Al (2)	24.6	33.5	0.5	39.3	2.1
Laser-polished Al (1)	27.9	24.3	0.2	47.6	0
Laser-polished Al (2)	27.6	24.5	0.1	47.8	0
Laser-polished Al fracture surface + trifluoroethanol (1)	14.2	49.8	6.3	29.6	0
Laser-polished Al fracture surface + trifluoroethanol (2)	14.8	48.6	6.3	30.2	0

The high energy resolution spectrum of Al 2p for as-received, laser-polished, and trifluoroethanol-treated Al samples are presented in figure 5.41. The peaks of the laser-polished Al sample have a larger Full-Width Half Maximum[45] for all the elements (O, N, C, Al) due to the roughness of the surface (heterogeneous charge distribution at the surface).

Unfortunately, the presence of an Al-O-C cannot be evidenced by comparing the peak shape of the trifluoroethanol-treated Al samples with the as-received or the laser-polished Al samples. However, the energy gap between Al and Al_2O_3 depends on the Al_2O_3-Al system (thin oxide on Al or bulk/thicker oxide) (see figure 5.42 regarding different positions of Al-O peak for different samples).
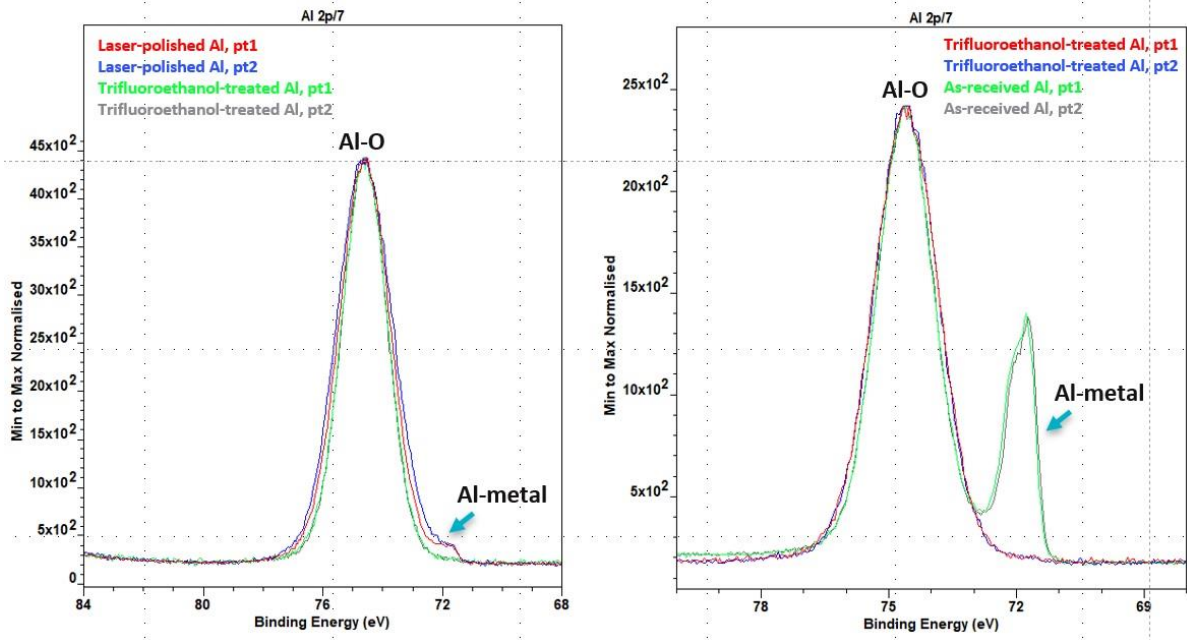
---

[45] FWHM

Figure 5.41. High energy resolution spectra of Al 2p, left: laser-polished and trifluoroethanol-treated Al samples, right: as-received, and trifluoroethanol-treated Al samples.
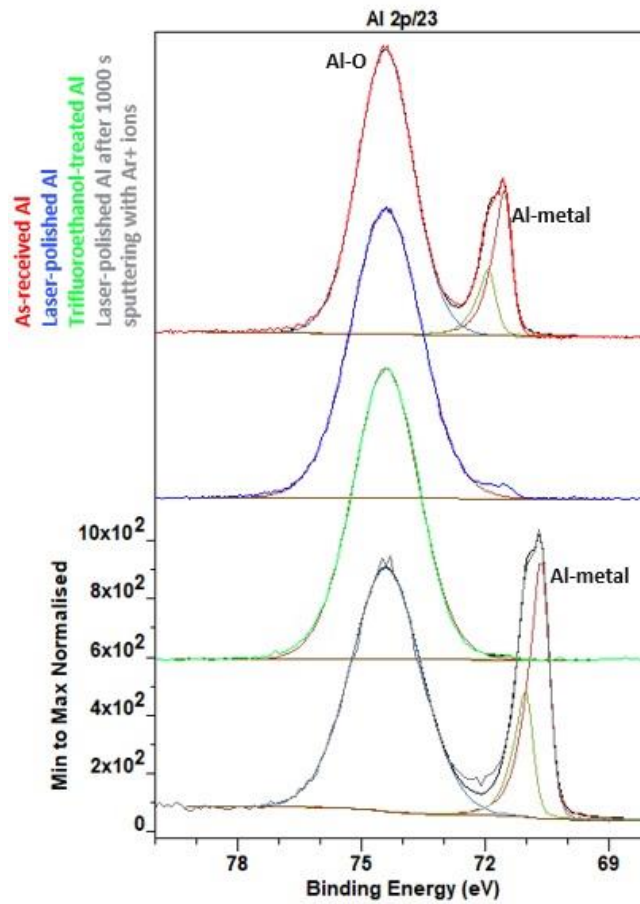

Figure 5.42. Al 2p spectrum for different Al samples and the effect of Al oxide morphology on the positions of Al-O peak.

5.4.3. ToF-SIMS results

As-received Al is mainly characterized as follows:

- In positive ion mode, the detection of element ions Na^+, K^+, Al^+ and many ions of type $Al_xO_yH_z^+$ such as $AlOH^+$, $AlO_2H_2^+$, $Al_2O_4H_3^+$, $Al_3O_5H2^+$, $Al_4O_6H^+$, $Al_5O_7^+$.

- In negative ion mode, the detection of several ions of type $Al_xO_yH_z^-$ such as AlO_2^-, $AlO_3H_2^-$, and $Al_2O_4H^-$.

- In addition, in negative ion mode Cl^-, $NaOH^-$, F^-, CF_3^-, and $C_3F_7^-$ are also detected and probably come from surface contaminations.

Laser-polished Al is mainly characterized by:

- All same ions were detected for the as-received sample. In addition, Zn^+ is detected in positive ion mode. In addition, $C_6H_{16}N^+$, $C_8H_{20}N^+$, and $C_{12}H_{24}N^+$ ions are also detected.

PA residue on as-received and laser-polished Al samples are similar and mainly characterized:

- By ions characteristic of a polyamide material such as CH_4N^+, $C_3H_3O^+$, $C_2H_5NO^+$, CH_2NO^+, $C_2H_6N^+$, $C_3H_6NO^+$, $C_5H_7N_2O^+$, $C_6H_{12}NO^+$, and CN^-, CNO^-, $C_2H_2N^-$ respectively in positive and negative ion modes.

- By ions characteristic of Si such as $SiC_3H_9^+$, $Si_2C_5H_{15}O$, $Si_3C_5H_{15}O_3^+$, $Si_3C_7H_{21}O_2^+$, $Si_4C_7H_{21}O_4^+$, and $SiCH_3O_2^-$, $SiC_3H_9O^-$, $Si_2C_3H_9O_3^-$, $Si_2C_5H_{15}O_2^-$, $Si_3C_7H_{21}O_3^-$, $Si_3C_5H_{15}O_4$ respectively in positive and negative ion modes, they could probably come from contamination present in the polyamide.

PA residue on laser-polished Al removed by trifluoroethanol sample is mainly characterized by:

- The combination of ions detected on the spectra of both laser-polished Al and polyamide residue on as-received Al samples excepted those relative to the Si contamination.

- In addition, ions characteristic of phosphates groups (PO_2^-, PO_3^-, PO_3H^-, and $PO_4H_2^-$) are detected in negative ion mode.

Figures 5.43 and 5.44 depict the images of ToF-SIMS for the laser-polished Al fracture surfaces in positive and negative modes, respectively. The image is taken from the border of PA residue on top of laser-polished Al. Therefore, on one side, the ion characteristics of Al, and on the other side, the ion characteristics of PA are observed.
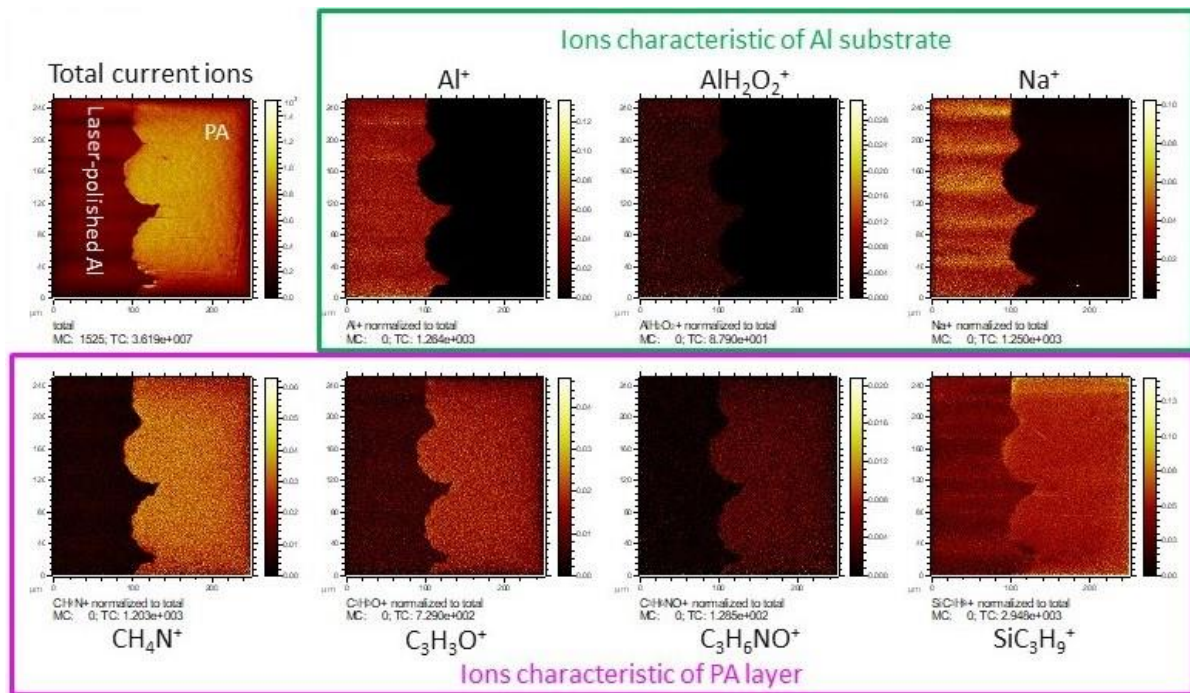
Figure 5.43. ToF-SIMS imaging in positive mode and normalized for the fracture surface of laser-polished Al (PA residue is on top of the artificial Al oxide).
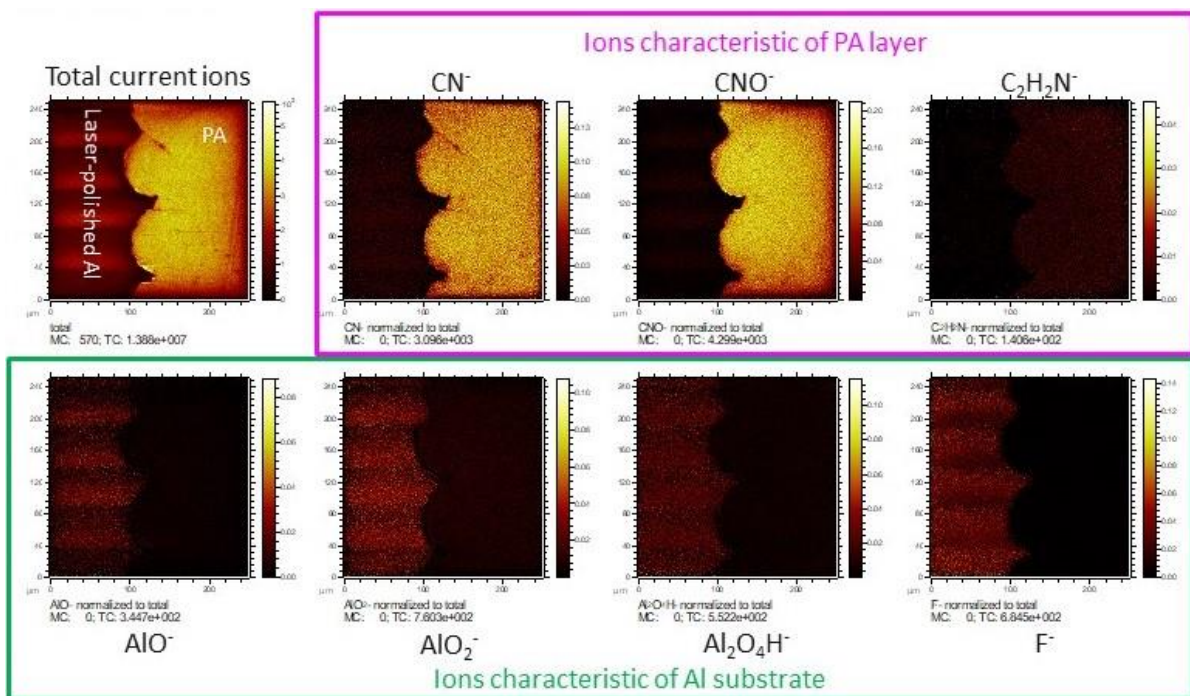
Figure 5.44. ToF-SIMS imaging in negative mode and normalized for the fracture surface of laser-polished Al (PA residue is on top of the artificial Al oxide).

Figures 5.45 and 5.46 depict the images of ToF-SIMS for the laser-polished Al fracture surfaces after trifluoroethanol treatment in positive and negative modes, respectively.
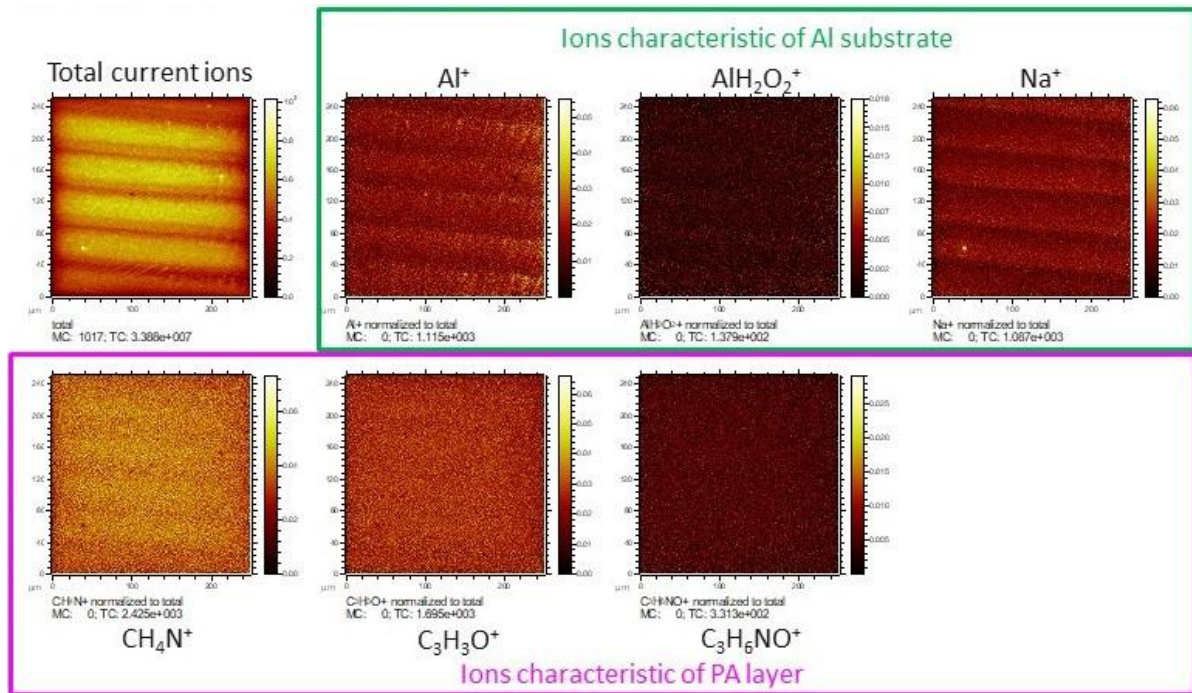
Figure 5.45. ToF-SIMS imaging in positive mode and normalized for the fracture surface of laser-polished Al after trifluoroethanol treatment.
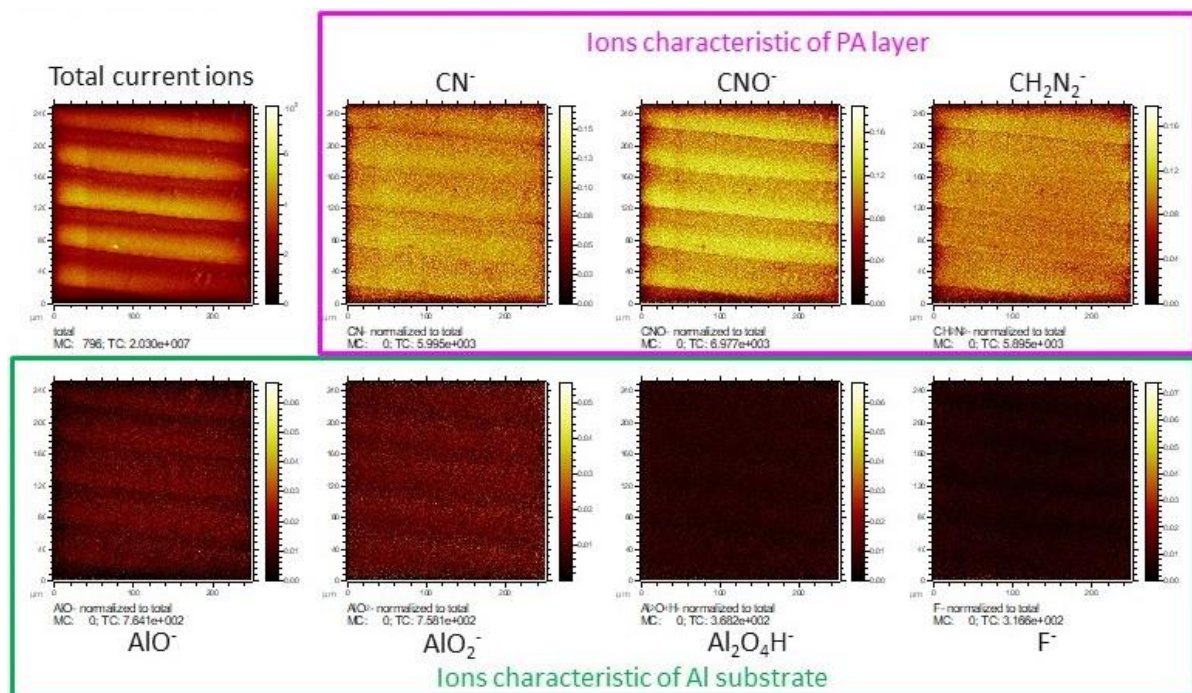
Figure 5.46. ToF-SIMS imaging in negative mode and normalized for the fracture surface of laser-polished Al after trifluoroethanol treatment.

The ion characteristics of both Al and PA are visible meaning that the treatment by trifluoroethanol solution dissolved the excessive PA on the laser-polished Al to reach the interface. It can be concluded that there is a strong chemical interaction between PA and Al at the interface. Otherwise, the PA should have been dissolved completely by 2,2,2-trifluoroethanol.
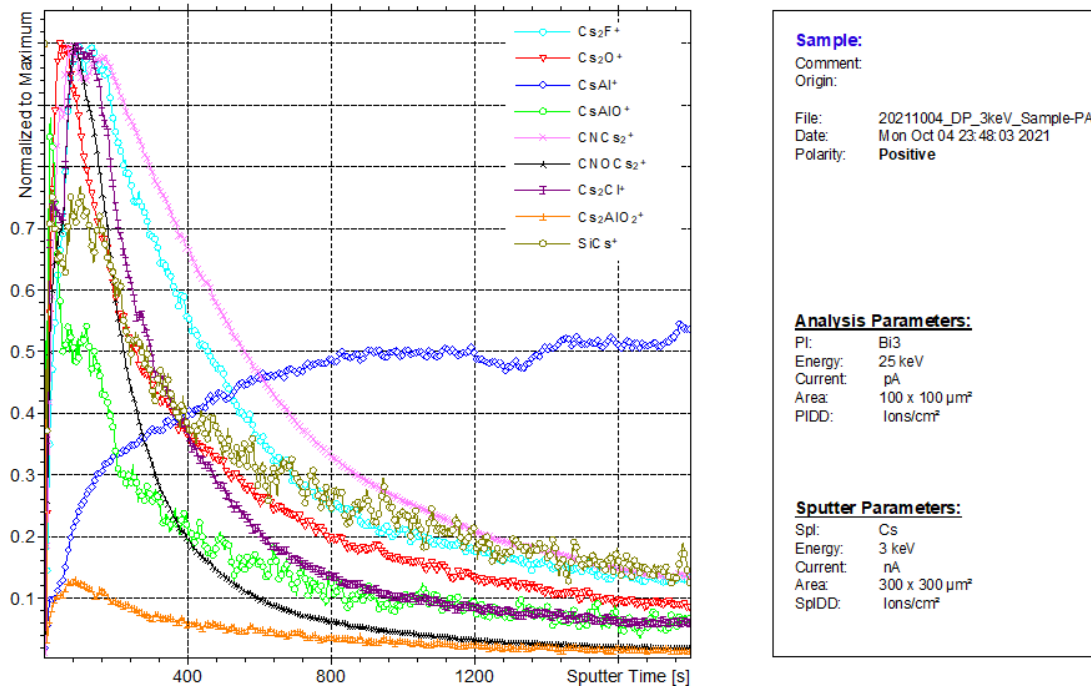
Figure 5.47. ToF-SIMS depth profiling of the as-received Al fracture surface.
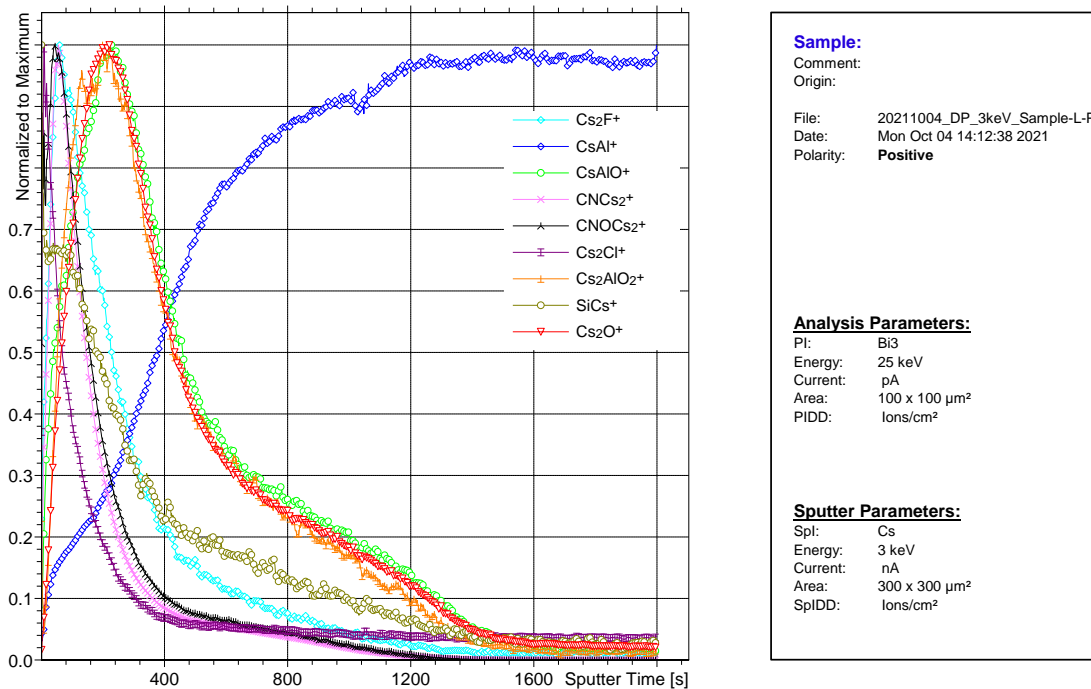
Figure 5.48. ToF-SIMS depth profiling of the laser-polished Al fracture surface.

Figure 5.47 shows the ToF-SIMS depth profiling of the as-received Al fracture surface and figure 5.48 shows that of laser-polished Al by Cs^+ gun. Therefore the ions are detected in the form of XCs^+ or XCs_2^+. Regarding the as-received Al fracture surface and sputtering from PA residue toward the as-received Al, two separated layers are identified; the first is the mixture of PA and aluminum oxide and the second is the Al substrate. However, for laser polished Al fracture surface, three layers are present; PA, aluminum oxide, and Al substrate.

Identifying the exact bonding between Al and PA at the interface needs further evaluation and studies. However, as reported by Hirchenhann [88], there are three different possible reactive sites in the PA: carbon, nitrogen, and oxygen sites. No reaction involving carbon sites is reported (also not observed in the present study with XPS) and the C-N-Al bond is not supported. The conclusion is on the C-O-Al bonds at the interface of Al/PA which is presented in figure 5.49.
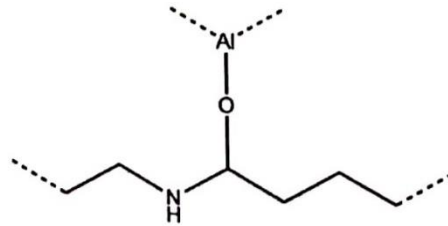
Figure 5.49. Scheme of the chemical bonding theory between Al and PA [88].

6. Validation and future work

6.1.　　The results of the salt-spray test

According to the standard of the automotive industry, the salt spray test was implemented on the laser-joined specimens for 500 hours. The following observations are worth noticing:

- The Laser-polishing process of Al and laser treatment of PA do not reduce the corrosion resistance of the materials.

- Laser-joined specimens with as-received Al and PA do not represent durability during the salt spray test and the joints break less than one week in the salt spray chamber.

- In a laser-joined specimen, the joint area must cover the whole overlap between the materials otherwise, due to the notch effect and promoting the capillary, corrosive media starts stacking up in the overhanging area and eventually weakens the joints during the salt spray test over time.

- Laser joining of Al to PA in optimum condition provides long time durability for the joint.

Figure 6.1. presents the shear load of the laser-joined samples after different times of the salt spray test.
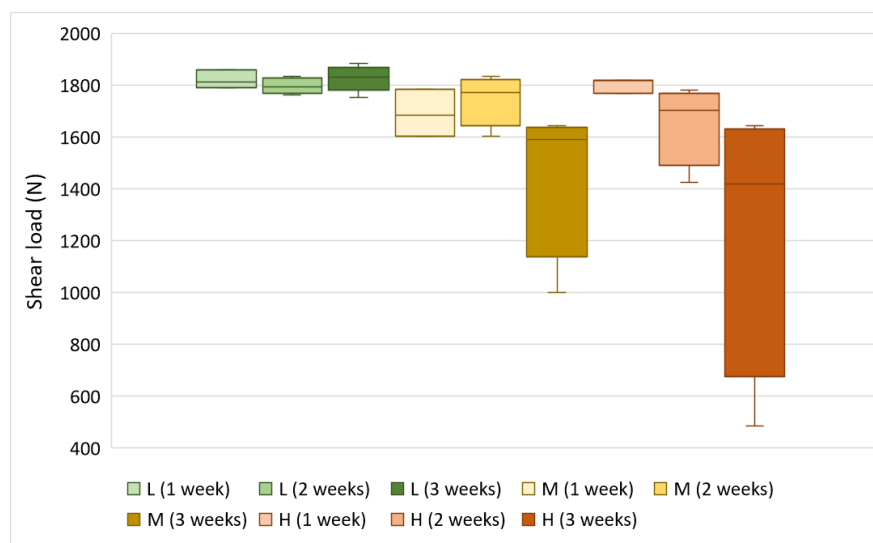
Figure 6.1. The shear load of the laser-joined samples after one, two, and three weeks of the salt spray test. (L: laser-joined samples with 5 mm/s, M: 60 mm/s, and H: 120 mm/s feed rate).

6.4.　　Metal-metal laser micro-welding

To maximize the mechanical properties of the joint it was tried to weld wire to the terminal with an innovative spatial modulation. As the dissimilar metals to be welded are only some parts of a component, which have other heat-sensitive parts in contact with them, minimizing

the heat input and consequently HAZ is essential. Therefore, to better control the heat input, power modulation was implemented.

To achieve the highest mechanical properties three different beam trajectories (linear, zigzag, and circular) were used to manipulate the weld seam [42].

6.5.   Metal-plastic laser joining

And finally, with the know-how developed in this study, the metallic cap (from stainless steel 304) is joined to GFRP (PA6.6 reinforced with 30% glass fibers). The performance of such an assembly is going to be validated in the future. Figure 6.2 depicts the design of the sensor with metal/metal laser micro-welding and metal/GFRP laser joining and figure 6.3 represents the prototype.
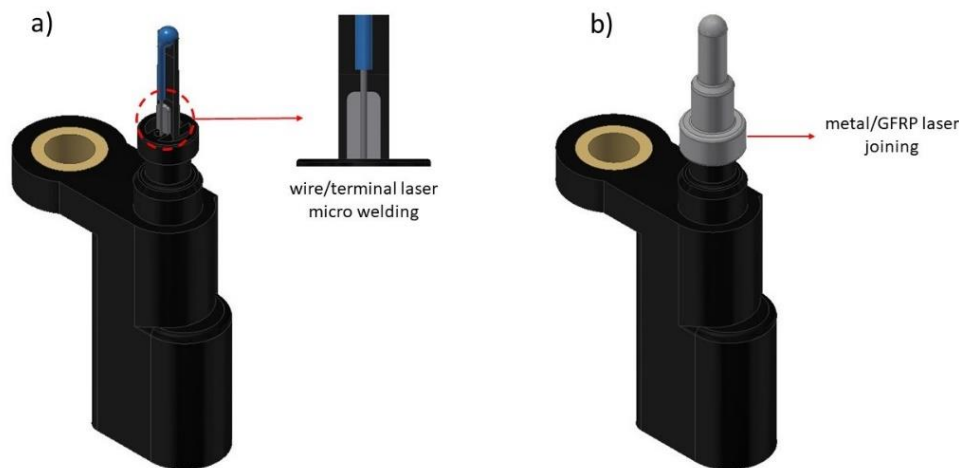
Figure 6.2. a) wire/terminal laser micro-welding and b) metal/GFRP laser joining for the sensor assembly.

Figure 6.3. The prototype of the final assembly.

7. Conclusion

Based on the present study for the laser joining of metals to polymers, three scientific gaps are discussed:

I) PA thermal degradation and its effect on the joint's quality
II) adhesion between Al and PA
III) the structural modification of PA during the laser joining process and the corresponding effect on the joint's mechanical performance.

The first gap is addressed by in-situ heating of PA inside ESEM and the temperature measurement during the laser-joining process.

- It is concluded that PA thermal degradation can be avoided by laser joining process parameters. The PA degradation is detrimental to joint performance more specifically for thinner Al partners.
- For 1 mm thick Al samples, the formation of the bubbles due to degradation is in the melted zone of PA while, in the case of 0.5 mm Al, they move to the Al which compromises the sealing of the joint and mechanical properties of Al partner.

The second gap is evaluated by the implementation of several pretreatments on the Al surface. They are mainly categorized into abrasive-based or laser-based treatments to modify the surface roughness in the presence of natural oxide or an artificial nanostructured oxide layer.

- Due to its morphology, the natural Al oxide layer on top of untreated Al does not provide good adhesion and wetting for molten PA during the joining process. Consequently, the failure of the corresponding assembly is mixed adhesive/cohesive with mediocre mechanical properties.
- Increasing the Al surface roughness with the absence of a nanostructured oxide layer (abrasive-blasted samples) does not increase the joint performance. However, it is detrimental to the heat transfer from Al to the PA surface due to an increase in thermal contact resistance. Consequently, the shear load of the joint significantly drops.
- The wetting characteristics and adhesion of PA to the artificial nanostructured Al oxide layer are superior. Thanks to the formation of the artificial oxide layer during the laser polishing process under ambient conditions, the shear load of the joints is 58% improved compared to the untreated samples. Consequently, cohesive failure is achieved with a relatively thick layer of PA on top of the Al fracture surface. for laser-ablated samples, the bubbles (due to local degradation of PA) govern the failure and for laser-polished Al, the structural modification of PA during the joining process brings the failure at HAZ.

The third gap is studied by the improvement of the joint's mechanical performance via three different processes. As the perfect adhesion between the materials is already achieved with the artificial nanostructured oxide layer, the PA structure in the HAZ was addressed to further improve the shear load of the joints.

- Laser pre-treatment of PA is responsible to increase the crystallinity degree of the PA near the surface with negligible chemical modification. Consequently, this modification of crystallinity prevents or delays the failure within PA and triggers the failure of Al in a ductile-shear manner.

- The heat treatment of the assemblies with laser-polished Al improves the joint mechanical performance while reaching the limits of the base materials. While the heat treatment of the as-received Al joined to PA presents a negative effect on the shear load due to the absence of an anchoring effect between the materials.

- Laser joining with different feed rates (and consequently different laser powers to avoid PA thermal degradation) provides different structures of PA in the melted area from amorphous (high feed rate of 120 mm/s) to semi-crystalline (slow feed rates of 2 and 5 mm/s). The shear strength of approximately 45 MPa is achieved in this study for a laser-polished Al sample laser-joined to PA with a slow feed rate.

And finally, based on different characterization techniques and more specifically Tof-SIMS on the interface of Al/PA, there are some pieces of evidence for a strong chemical interaction between Al and PA. Based on other literature, the C-O-Al bonds at the interface of Al/PA are proposed. Further evaluations are needed to prove the hypothesis.

8. References

[1] A. Heckert and M. F. Zaeh, "Laser surface pre-treatment of aluminium for hybrid joints with glass fibre reinforced thermoplastics", Phys. Procedia, vol. 56, pp. 1171–1181, 2014.

[2] A. Fortunato, G. Cuccolini, A. Ascari, L. Orazi, G. Campana, and G. Tani, "Hybrid metal-plastic joining by means of laser", Int. J. Mater. Form., vol. 3, pp. 1131–1134, 2010.

[3] C. Magnus, "Feasibility study of metal to polymer hybrid joining", M.Sc. thesis, Lappeenranta University of Technology, Finland, 2012.

[4] K. W. Jung, Y. Kawahito, M. Takahashi, and S. Katayama, "Laser direct joining of carbon fiber reinforced plastic to zinc-coated steel", Mater. Des., vol. 47, pp. 179–188, 2013.

[5] "Surface treatment of materials for adhesion bonding", S. Ebnesajjad and C. F. Ebnesajjad, Willian Andrew Publishing, USA, 2006.

[6] "Polymer surfaces from physics to technology", F. Garbassi, M. Morra, and E. Occhiello, John Wiley and Sons, UK, 1994.

[7] "Handbook of adhesive and sealants", E. M. Petrie, McGraw Hill Professional, USA, 1999.

[8] B. Escaig, "Binding metals to polymers. A short review of basic physical mechanisms", J. Phys., vol. 3, pp. 753–761, 1993.

[9] J. W. Bartha, P. O. Hahn, F. LeGoues, and P. S. Ho, "Photoemission spectroscopy study of aluminum–polyimide interface", J. Vac. Sci. Technol. A: Vacuum, Surfaces, and Films, vol. 3, pp. 1390–1393, 1985.

[10] S. Katayama and Y. Kawahito, "Direct joining of metal and plastic with laser", Scr. Mater., vol. 59, pp. 1247–1250, 2008.

[11] M. Gao, W. Liao, and C. Chen, "Improving the interfacial bonding strength of dissimilar PA66 plastic and 304 stainless steel by oscillating laser beam", Opt. Laser Technol., vol. 138 (106869), 2021.

[12] D. J. Jung, J. Cheon, and S. J. Na, "Effect of surface pre-oxidation on laser assisted joining of acrylonitrile butadiene styrene (ABS) and zinc-coated steel", Mater. Des., vol. 99, pp. 1–9, 2016.

[13] P. S. Ho, R. Haight, R. C. White, B. D. Silverman, "Chemistry and microstructure at metal-polymer interfaces", J. Phys., pp. 49-59, 1988.

[14] C. W. Chan and G. C. Smith, "Fibre laser joining of highly dissimilar materials: Commercially pure Ti and PET hybrid joint for medical device applications", Mater. Des., vol. 103, pp. 278–292, 2016.

[15] T. Sultana, G. L. Georgiev, G. Auner, G. Newaz, H. J. Herfurth, and R. Patwa, "XPS analysis of laser transmission micro-joint between poly (vinylidene fluoride) and titanium", Appl. Surf. Sci., vol. 255, pp. 2569–2573, 2008.

[16] G. L. Georgiev et al., "XPS study of laser fabricated titanium/KaptonFN interfaces", Appl. Surf. Sci., vol. 254, pp. 7173–7177, 2008.

[17] D. G. Georgiev, R. J. Baird, G. Newaz, G. Auner, R. Witte, and H. Herfurth, "An XPS study of laser-fabricated polyimide/titanium interfaces", Appl. Surf. Sci., vol. 236, pp. 71–76, 2004.

[18] J. P. Bergmann and M. Stambke, "Potential of laser-manufactured polymer-metal hybrid Joints", Phys. Procedia, vol. 39, pp. 84–91, 2012.

[19] "Joining of polymer-metal hybrid structures", S. T. Amancio-Filho and L. A. Blaga, Part III, M. Grujicic, "Joining processes based on direct-assembly methods", Wiley, USA, 2018.

[20] R. Y. Yeh and R. Q. Hsu, "Application of porous oxide layer in plastic/metal direct adhesion by injection molding", J. Adhes. Sci. Technol., vol. 29, pp. 1617–1627, 2015.

[21]   T. Kleffel and D. Drummer, "Investigating the suitability of roughness parameters to assess the bond strength of polymer-metal hybrid structures with mechanical adhesion", Compos. Part B Eng., vol. 117, pp. 20–25, 2017.

[22]   B. Huang, L. Sun, L. Li, L. Zhang, Y. Lin, and J. Che, "Experimental investigation of the strength of polymer-steel direct adhesion (PSDA) joints with micro-structures ablated by laser", J. Mater. Process. Technol., vol. 249, pp. 407–414, 2017.

[23]   M. Grujicic, V. Sellappan, M. A. Omar, N. Seyr, A. Obieglo, M. Erdmann, J. Holzeitner, "An overview of the polymer-to-metal direct-adhesion hybrid technologies for load-bearing automotive components", J. Mater. Process. Technol., vol. 197, pp. 363–373, 2008.

[24]   P. Kah, R. Suoranta, J. Martikainen, and C. Magnus, "Techniques for joining dissimilar materials: Metals and polymers", Rev. Adv. Mater. Sci., vol. 36, pp. 152–164, 2014.

[25]   "Handbook of adhesive technology", A. Pizzi, K. L. Mittal, Marcel Dekker, USA, 2003.

[26]   Y. Farazila, M. Fadzil, and M. Hamdi, "A Brief Review: Laser Joining of Polymer-Metal Structures", ASEAN Eng. J. vol. 2, pp. 5–12, 2012.

[27]   M. S. Ali, "A support system for evaluating a suitable joining method in the production of sheet metal goods", M.Sc. thesis, Lappeenranta University of Technology, Finland, 2005.

[28]   A. F. Grandt, Jr, "Materials degradation and fatigue in aerospace structures", Final report for air force office of scientific research, Purdue University, USA, 1997.

[29]   S. T. Amancio-Filho and J. F. dos Santos, "Joining of polymers and polymer-metal hybrid structures: recent developments and trends", Polym. Eng. Sci., vol. 49, pp. 1461-1476, 2009.

[30]   S. M. Goushegir, J. F. dos Santos, and S. T. Amancio-Filho, "Influence of process parameters on mechanical performance and bonding area of AA2024/carbon-fiber-reinforced poly (phenylene sulfide) friction spot single lap joints", Mater. Des., vol. 83, pp. 431–442, 2015.

[31]   S. M. Goushegir, J. F. dos Santos, and S. T. Amancio-Filho, "Influence of aluminum surface pre-treatments on the bonding mechanisms and mechanical performance of metal-composite single-lap joints", Weld. World, vol. 61, pp. 1099–1115, 2017.

[32]   F. Balle, S. Huxhold, S. Emrich, G. Wagner, M. Kopnarski, and D. Eifler, "Influence of heat treatments on the mechanical properties of ultrasonic welded AA 2024/CF-PA66-joints", Adv. Eng. Mater., vol. 15, pp. 837–845, 2013.

[33]   R. Y. Yeh and R. Q. Hsu, "Development of ultrasonic direct joining of thermoplastic to laser structured metal", Int. J. Adhes. Adhes., vol. 65, pp. 28–32, 2016.

[34]   "Fundamentals and details of laser welding", S. Katayama, Springer, Germany, 2020.

[35]   "Laser Welding Fundamentals", Amada Miyachi America, 2015.

[36]   "LIA handbook of laser materials processing", J. F. Ready and D. F. Farson, Laser Institute of America, Magnolia Publishing, USA, 2001.

[37]   "Handbook of laser welding technologies", S. Katayama, Woodhead Publishing, USA, 2013.

[38]   "ASM handbook, vol. 3, Alloy phase diagrams", ASM (American Society for Metals) International, USA, 1992.

[39]   T. Solchenbach, "Laserbasiertes Schweißlöten von Artungleichen Aluminium-Kupfer-Verbindungen", Ph.D. thesis, University of Luxembourg, 2014.

[40]   M. Naeem, A. Montello, and C. Rasmussen, "Experimental studies of fiber laser welding of a range of dissimilar material combinations", Lasers in Manufacturing (LiM) conference proceeding, Germany, 2015.

[41]   D. Harwani and K. Banker, "Welding of dissimilar metal alloys by laser beam welding & friction stir welding techniques", Int. J. Eng. Res. App., vol. 4, no. 12, pp. 64–70, 2014.

[42]   M. Amne Elahi and P. Plapper, "Dissimilar laser micro-welding of nickel wire to CuSn6 bronze terminal", Trans. Indian Inst. Met., vol. 72, pp. 27–34, 2019.

[43]   E. Haberstroh and M. Sickert, "Thermal direct joining of hybrid plastic metal components", KMUTNB Int. J. Appl. Sci. Technol., vol. 7, pp. 29–34, 2014.

[44]   A. Roesner, A. Olowinsky, and A. Gillner, "Long term stability of laser joined plastic metal parts", Phys. Procedia, vol. 41, pp. 169–171, 2013.

[45]   A. Roesner, S. Scheik, A. Olowinsky, A. Gillner, U. Reisgen, and M. Schleser, "Laser assisted joining of plastic metal hybrids", Phys. Procedia, vol. 12, pp. 373–380, 2011.

[46]   E. Rodríguez-Vidal, J. Lambarri, C. Soriano, C. Sanz, and G. Verhaeghe, "A combined experimental and numerical approach to the laser joining of hybrid polymer - Metal parts", Phys. Procedia, vol. 56, pp. 835–844, 2014.

[47]   J. Rauschenberger, A. Cenigaonaindia, J. Keseberg, D. Vogler, U. Gubler, and F. Liébana, "Laser hybrid joining of plastic and metal components for lightweight components", Lasers in Manufacturing (LiM) conference proceeding, Germany, 2015.

[48]   S. Arai, Y. Kawahito, and S. Katayama, "Effect of surface modification on laser direct joining of cyclic olefin polymer and stainless steel", Mater. Des., vol. 59, pp. 448–453, 2014.

[49]   E. Rodríguez-Vidal, C. Sanz, J. Lambarri, and I. Quintana, "Experimental investigation into metal micro-patterning by laser on polymer-metal hybrid joining", Opt. Laser Technol., vol. 104, pp. 73–82, 2018.

[50]   P. Amend, S. Pfindel, and M. Schmidt, "Thermal joining of thermoplastic metal hybrids by means of mono- and polychromatic radiation", Phys. Procedia, vol. 41, pp. 98–105, 2013.

[51]   E. Rodríguez-Vidal, C. Sanz, C. Soriano, J. Leunda, and G. Verhaeghe, "Effect of metal micro-structuring on the mechanical behavior of polymer-metal laser T-joints", J. Mater. Process. Technol., vol. 229, pp. 668–677, 2016.

[52]   K. Schricker, M. Stambke, J. P. Bergmann, K. Bräutigam, and P. Henckell, "Macroscopic surface structures for polymer-metal hybrid joints manufactured by laser based thermal joining", Phys. Procedia, vol. 56, pp. 782–790, 2014.

[53]   A. Cenigaonaindia, F. Liébana, A. Lamikiz, and Z. Echegoyen, "Novel strategies for laser joining of polyamide and AISI 304", Phys. Procedia, vol. 39, pp. 92–99, 2012.

[54]   Y. Kajihara, Y. Tamura, F. Kimura, G. Suzuki, N. Nakura, and E. Yamaguchi, "Joining strength dependence on molding conditions and surface textures in blast-assisted metal-polymer direct joining", CIRP Ann., vol. 67, pp. 591–594, 2018.

[55]   Y. Kawahito, Y. Niwa, T. Terajima, and S. Katayama, "Laser direct joining of glassy metal Zr55Al10Ni5Cu30 to engineering plastic polyethylene terephthalate", Mater. Trans., vol. 51, no. 8, pp. 1433–1436, 2010.

[56]   C. Lamberti, T. Solchenbach, P. Plapper, and W. Possart, "Laser assisted joining of hybrid polyamide-aluminum structures", Phys. Procedia, vol. 56, pp. 845–853, 2014.

[57]   F. Yusof, M. Yukio, M. Yoshiharu, and M. H. Abdul Shukor, "Effect of anodizing on pulsed Nd:YAG laser joining of polyethylene terephthalate (PET) and aluminium alloy (A5052) ", Mater. Des., vol. 37, pp. 410–415, 2012.

[58]   Z. Zhang, J. Shan, X. Tan, and J. Zhang, "Effect of anodizing pretreatment on laser joining CFRP to aluminum alloy A6061", Int. J. Adhes. Adhes., vol. 70, pp. 142–151, 2016.

[59] A. Gisario, M. Mehrpouya, and E. Pizzi, "Dissimilar joining of transparent poly (ethylene terephthalate) to aluminum 7075 sheets using a diode laser", J. Laser Appl., vol. 29, 2017.

[60] C. Hopmann, S. Kreimeier, J. Keseberg, and C. Wenzlau, "Joining of metal-plastics-hybrid structures using laser radiation by considering the surface structure of the metal", J. Polym., vol. 2016, 2016.

[61] E. Ukar, F. Liébana, M. Andrés, I. Marcos, and A. Lamikiz, "Laser texturing and dissimilar material joining", Procedia Manuf., vol. 13, pp. 671–678, 2017.

[62] A. Bauernhuber and T. Markovits, "Investigating thermal interactions in the case of laser assisted joining of PMMA plastic and steel," Phys. Procedia, vol. 56, pp. 811–817, 2014.

[63] M. Andrés, M. Ferros, and F. Liébana, "Influence of temperature and clamping force on the strength of the joint over different composite-metal combinations joined by laser", Procedia CIRP, vol. 74, pp. 506–510, 2018.

[64] "Aluminium Automotive Manual" – Joining dissimilar materials, European Aluminium Association, 2015.

[65] F. Lambiase and S. Genna, "Laser-assisted direct joining of AISI304 stainless steel with polycarbonate sheets: Thermal analysis, mechanical characterization, and bonds morphology", Opt. Laser Technol., vol. 88, pp. 205–214, 2017.

[66] S. Katayama, "Laser joining of metal and plastic", Industrial Laser Solutions. 2010. https://www.industrial-lasers.com/welding/article/16485092/laser-joining-of-metal-and-plastic

[67] Z. Zhang, J. Shan, X. Tan, and J. Zhang, "Improvement of the laser joining of CFRP and aluminum via laser pre-treatment", Int. J. Adv. Manuf. Technol., 2016.

[68] S. P. Dwivedi, S. Sharma, and V. Singh, "Optimization of laser transmission joining process parameters on joint width of PET and 316 L stainless steel joint using RSM", J. Opt., vol. 45, pp. 106–113, 2016.

[69] X. Wang et al., "Modeling and optimization of laser transmission joining process between PET and 316L stainless steel using response surface methodology", Opt. Laser Technol., vol. 44, pp. 656–663, 2012.

[70] C. Lamberti, I. Peral Alonso, and P. Plapper, "Influence of material moisture during Laser Joining of Polyamide 6.6 to Aluminum", ATINER'S Conference, 2017.

[71] K. Schricker and J. Pierre Bergmann, "Determination of sensitivity and thermal efficiency in laser assisted metal-plastic joining by numerical simulation", Procedia CIRP, vol. 74, pp. 511–517, 2018.

[72] K. Schricker, M. Stambke, J. P. Bergmann, and K. Bräutigam, "Laser-based joining of thermoplastics to metals: influence of varied ambient conditions on joint performance and microstructure", Int. J. Polym. Sci., vol. 2016, 2016.

[73] M. Wahba, Y. Kawahito, and S. Katayama, "Laser direct joining of AZ91D thixomolded Mg alloy and amorphous polyethylene terephthalate", J. Mater. Process. Technol., vol. 211, pp. 1166–1174, 2011.

[74] Y. Kawahito, Y. Niwa, and S. Katayama, "Laser direct joining between stainless steel and polyethylene terephthalate plastic and reliability evaluation of joints", Weld. Int., vol. 28, pp. 107–113, 2014.

[75] K. Schricker and J. P. Bergmann, "Temperature- and time-dependent penetration of surface structures in thermal joining of plastics to metals", Key Eng. Mater., vol. 809, pp. 378–385, 2019.

[76]   Y. J. Chen, T. M. Yue, and Z. N. Guo, "A new laser joining technology for direct-bonding of metals and plastics", Mater. Des., vol. 110, pp. 775–781, 2016.

[77]   H. Wang, Y. Chen, Z. Guo, and Y. Guan, "Porosity elimination in modified direct laser joining of Ti6Al4V and thermoplastics composites", Appl. Sci., vol. 9, 2019.

[78]   J. Jiao, Z. Xu, Q. Wang, L. Sheng, and W. Zhang, "CFRTP and stainless steel laser joining: Thermal defects analysis and joining parameters optimization", Opt. Laser Technol., vol. 103, pp. 170–176, 2018.

[79]   K. Ramani and B. Moriarty, "Thermoplastic bonding to metals via injection molding for macro-composite manufacture", Polym. Eng. Sci., vol. 38, pp. 870–877, 1998.

[80]   A. N. Fuchs, F. X. Wirth, P. Rinck, and M. F. Zaeh, "Laser-generated macroscopic and microscopic surface structures for the joining of aluminum and thermoplastics using friction press joining", Phys. Procedia, vol. 56, pp. 801–810, 2014.

[81]   A. Heckert, C. Singer, and M. F. Zaeh, "Pulsed laser surface pre-treatment of aluminium to join aluminium- thermoplastic hybrid parts," Lasers in Manufacturing (LiM) conference, Germany, 2015.

[82]   K. Schricker, M. Stambke, and J. P. Bergmann, "Experimental investigations and modeling of the melting layer in polymer-metal hybrid structures", Weld. World, vol. 59, pp. 407–412, 2015.

[83]   K. Schricker, J. P. Bergmann, M. Hopfeld, and L. Spieß, "Effect of thermoplastic morphology on mechanical properties in laser-assisted joining of polyamide 6 with aluminum", Weld. World, vol. 65, no. 4, pp. 699–711, 2021.

[84]   P. Amend, C. Mohr, and S. Roth, "Experimental investigations of thermal joining of polyamide aluminum hybrids using a combination of mono- and polychromatic radiation", Phys. Procedia, vol. 56, pp. 824–834, 2014.

[85]   B. Burzic, M. Hofele, S. Murdter, "Laser polishing of ground aluminum surfaces with high energy continuous wave laser", J. Laser Appl., vol. 29 (011701), 2017.

[86]   C. Arnaud, A. Almirall, C. Loumena, "Potential of structuring and polishing with fiber laser on homogeneous metals", J. Laser Appl., vol. 29 (022501), 2017.

[87]   L. Penel Pierron, "Deformation-induced phase transitions in hydrogen-bonding polymers: ethylene vinyl alcohol copolymers and polyamide 6", Ph.D. thesis, Lille 1 University, France, 1998.

[88]   P. Hirchenhahn, "Fundamental study of the adhesion phenomena in polymer-metal hybrid materials obtained by laser welding", Ph.D. thesis, University of Namur, Belgium, 2020.

[89]   M. Kocun, A. Labuda, W. Meinhold, I. Revenko, R. Proksch, "Fast, high resolution, and wide modulus range nanomechanical mapping with bimodal tapping mode", ACS nano 11, 2017.

[90]   C. Engelmann, J. Eckstaedt, A. Olowinsky, M. Aden, and V. Mamuschkin, "Experimental and simulative investigations of laser assisted plastic-metal-joints considering different load directions", Phys. Procedia, vol. 83, pp. 1118–1129, 2016.

[91]   X. Tan, J. Zhang, J. Shan, S. Yang, and J. Ren, "Characteristics and formation mechanism of porosities in CFRP during laser joining of CFRP and steel", Compos. Part B Eng., vol. 70, pp. 35–43, 2015.

[92]   L. Lin, A. S. Argon, "Deformation resistance in oriented nylon 6", Macromolecules, vol. 25, pp. 4011-4024, 1992.

[93]   M. Mortazavi and M. Nosonovsky, "A model for diffusion-driven hydrophobic recovery in plasma treated polymers", Appl. Surf. Sci., vol. 258, no. 18, pp. 6876–6883, 2012.

[94]   https://www.engineeringtoolbox.com/linear-expansion-coefficients-d_95.html, date of access: 10/03/2020.

[95]   "Technical datasheet of PA 6.6", Dutec, 2018.

[96]   C. Lamberti, "Optimierung und Charakterisierung einer Mittels Laserstrahl Gefügten Verbindung Zwischen Aluminium und Polyamid 6.6", Ph.D. thesis, University of Luxembourg, 2018.

[97]   https://en.wikipedia.org/wiki/Lotus_effect, date of access: 18/19/2021.

8.1.   Structure of the references (LAMP joining or study the interface of metal/polymer)

References	Surface treatment	Polymer degradation(+) polymer structure (++)	Study the interface	Mechanical properties	Mechanism of joining/bonding	Process	Material combination
Amend et al. 2013	+	+		+		Laser joining	PC-PA6-PA6.6GF30/Al 5182
Amend et al. 2014	+			+		Laser joining	PA6/Al
Arai et al. 2014	+	+	+	+	+	Laser joining	COP/SST 304
Bartha et al. 1985			+			Deposition	PI/Al
Bauernhuber and Markovits 2012		+		+		Laser joining	PMMA/St
Bergmann and Stambke 2012	+	+		+		Laser joining	PA6.6-PA6GF45/DC01 St
Cenigaonaindia et al. 2012	+			+		Laser joining	PA 6/SST 304
Chan and Smith 2016	+		+	+	+	Laser joining	PET/Ti
Chen et al. 2016		+	+	+	+	Laser joining	PET/Ti
Cheon and Na		++			+	Laser joining	HDPE/AISI304
Dwivedi et al. 2016				+		Laser joining	PET/316 SST
Engelmann et al. 2016	+		+			Laser joining + Modeling	PC/SST 1.4301
Escaig 1993					+	Deposition	-
Fortunato et al. 2010				+		Laser joining	PA6.6-GFRP-CFRP/304 SST
Fuchs et al. 2014	+			+		Friction press joining	PA6GF15-PA6GF30/Al 6082
Gao et al. 2021		++	+	+	+	Laser joining	PA6.6/304 SST
Georgiev et al. 2004			+		+	Laser joining	PI/Ti
Georgiev et al. 2008			+		+	Laser joining	KeptonFN/Ti
Gisario et al. 2017				+		Laser joining	PET/7075 Al
Haberstroh and Sickert 2006	+			+		Thermal Direct Joining	PA6-PA6GF30/St-Al
Heckert and Zaeh 2014	+			+		Laser joining	PA6-PA6.6-PBT-GFRP/Al 6082
Heckert et al. 2015	+			+	+	Laser joining	PA6GF66/Al6082
Ho et al. 1988			+		+	Deposition	PI/Cu-Cr
Holktamp et al. 2010	+			+		Laser joining	PC-POM-PA/Ti-SST
Hopmann et al. 2016	+				+	Laser joining	MABS-PA6.6GF35-PP-PC/St-Al
Huang et al. 2017	+			+		Laser joining	PAGF35/St

Reference						Method	Material
Hussein et al. 2013		+		+		Laser joining	PMMA/304 SST
Jiao et al. 2018			+	+		Laser joining	CFRP/304 SST
Jung et al. 2013 (Dec. 2012)		+	+	+	+	Laser joining	CFRP/St
Jung et al. 2013 (JWRI)		+		+	+	Laser joining	PA6CF20/St
Jung et al. 2013 May		+	+	+	+	Laser joining	CFRP/5052 Al
Jung et al. 2016	+	+	+	+	+	Laser joining	ABS/St
Kajihara et al. 2018	+			+		Injection molding	PBT/Al
Katayama and Kawahito 2008		+	+	+	+	Laser joining	PET/304 SST
Kawahito et al. 2010		+		+	+	Laser joining	PET/Zr55Al10Ni5Cu30
Kawahito et al. 2012		+	+	+	+	Laser joining	PET/304 SST
Lamberti et al. 2014	+			+	+	Laser joining	PA6.6/Al
Lamberti et al. 2017		+				Laser joining	PA6.6/Al
Lambiase and Genna 2017		+		+		Laser joining	PC/ 304 SST
Mian et al. 2005			+	+	+	Laser joining	PI/Ti
Pagano et al. 2017				+		Laser joining	PLA/Al
Ramani and Moriarty	+			+		Injection molding	PC/1018 St
Ramani and Tagle 1996		+		+		Injection molding	PEKEKK/Ti6Al4V
Ramani and Zhao		++		+		Injection molding	PEEK-PEI/St
Rauschenberger et al. 2015	+			+		Laser joining	MABS-PA6.6GF35/Stl-SST
Rodríguez-Vidal et al. 2014	+			+		Laser joining + Modeling	PA6GF30/St DP 1000
Rodríguez-Vidal et al. 2016	+			+		Laser joining	PA6GF30/HC420LA Steel
Rodríguez-Vidal et al. 2018	+			+		Laser joining	PA6-GF30/HC420St
Roesner et al. 2011	+			+		Laser joining	PC-PA-GFRP/Steel
Roesner et al. 2013	+			+		Laser joining	PC/?
Sanz and Soriano 2014	+			+		Laser joining	PAGF30/St
Schricker and Bergmann 2018	+	+				Laser joining + Modeling	PA6-PA6.6-PP/Al6082-SST 304
Schricker and Bergmann 2019	+			+		Laser joining	PP/Al 6082
Schricker et al. 2014	+			+		Laser joining	PA6.6/Al 6082
Schricker et al. 2015	+	+				Laser joining	PA6.6/Al6082
Schricker et al. 2016	+	+		+		Laser joining	PA6.6/Al 6082
Schricker et al. 2018	+	++				Laser joining	PA6-PA6.6-PP/Al6082

Schricker et al. 2021	+	++		+		Laser joining	PA6/Al6082
Sultana et al. 2008			+	cebi	+	Laser joining	PVDF/Ti
Tan et al. 2015		+				Laser joining	PA6CF30/St
Ukar et al. 2017	+					Laser joining + Modeling	Tepex102/304 SST
Wahba et al. 2011	+	+		+	+	Laser joining	PET/AZ91D
Wang et al. 2010			+	+	+	Laser joining	PET/Ti
Wang et al. 2012				+		Laser joining	PET/316 SST
Wang et al. 2019	+					Laser joining	PA6.6GF30/Ti6Al4V
Yusof et al. 2012	+		+	+		Laser joining	PET/Al 5052
Zhang et al. 2016	+	+	+	+	+	Laser joining	PA6-22%CFRP/Al 6061
Zhang et al. 2016	+			+		Laser joining	PA6CF22/Al 7050

8.2. List of publications

- Mahdi Amne Elahi, Max Hennico, Peter Plapper, "The effect of temperature and joining speed on the joining quality for conduction laser joining of metals to polymers", Lasers in Manufacturing (LiM) Proceeding, 2021.

- Mahdi Amne Elahi, Marcus Koch, Julien Bardon, Frédéric Addiego, Peter Plapper, "Failure mechanism analysis based on laser-based surface treatments for aluminum-polyamide laser joining", Journal of Materials Processing Technology, Vol. 298, 2021. https://doi.org/10.1016/j.jmatprotec.2021.117318

- Mahdi Amne Elahi, Marcus Koch, Peter Plapper, "Evaluation of the Joint Based on Different Surface Conditions for Aluminum-Polyamide Laser Welding", Journal of Laser Applications, Vol. 33, 2021. https://doi.org/10.2351/7.0000326

- Mahdi Amne Elahi, Marcus Koch, Mike Heck, Peter Plapper, "Pre and post-treatments to improve weldability and mechanical properties of aluminum-polyamide laser welded specimens", Procedia CIRP, Vol. 94, 2020, pp. 537-541. https://doi.org/10.1016/j.procir.2020.09.178

- Mahdi Amne Elahi, Marcus Koch, Peter Plapper, "Laser polishing of Aluminum and Polyamide for dissimilar laser welded assemblies", Lasers in Manufacturing (LiM) proceeding, Munich, Germany, June 2019. https://www.wlt.de/lim/Proceedings2019/data/9.html

- Mahdi Amne Elahi, Peter Plapper, "Dissimilar Laser Micro-Welding of Nickel Wire to CuSn6 Bronze Terminal", Transactions of the Indian Institute of Metals, Vol. 72, 2019, pp. 27-34. https://doi.org/10.1007/s12666-018-1457-y

8.3.   List of conference presentations

➢ The effect of temperature and joining speed on the joining quality for conduction laser joining of metals to polymers, Lasers in Manufacturing (LiM) Conference, Munich, Germany, June 2021.

➢ Evaluation of the Joint Based on Different Surface Conditions for Aluminum-Polyamide Laser Welding", International Congress on Applications of Lasers and Electro-Optics (ICALEO), Chicago, USA, Oct. 2020.

➢ Pre and post-treatments to improve weldability and mechanical properties of aluminum-polyamide laser welded specimens, 11th CIRP Conference on Photonic Technologies (LANE), Erlangen, Germany, September 2020.

➢ Laser polishing of Aluminum and Polyamide for dissimilar laser welded assemblies, Lasers in Manufacturing (LiM) Conference, Munich, Germany, June 2019.

➢ Laser micro-welding of wire to flat geometry for dissimilar materials in an electromechanical application, 11th International Conference on Photo-Excited Processes and Applications (ICPEPA 11), Vilnius, Lithuania, September 2018.

8.4.   List of supervised projects

➢ Ricardo Santos Teixeira, "The effect of laser-based surface treatments on the mechanical properties of Al-GFRP laser joined specimens", Bachelor thesis, summer semester 2020-2021, University of Luxembourg.

➢ Max Hennico, "Temperature measurement for heat conduction laser joining of metals to polymers", Bachelor thesis, winter semester 2020-2021, University of Luxembourg.

➢ Mike Heck, "The effect of Al surface roughness at Al/PA interface on the joint quality of laser welded assemblies", Bachelor thesis, winter semester 2019-2020, University of Luxembourg.

➢ Hasan Nadeem, "Laser Polishing of DC-01 steel using micro and macro polishing techniques", Master case study, winter semester 2019-2020, University of Luxembourg.

➢ Gowtham Ravi, "Study the heat generation during macro laser polishing of aluminum", Master case study, winter semester 2019-2020, University of Luxembourg.

➢ Kevin De Oliveira, "Study the simulation and experiments of micro-welding for an electromechanical application", Bachelor thesis, winter semester 2018-2019, University of Luxembourg.